Technical University of Crete
School of Electrical and Computer Engineering

Experimental modelling of stator poles for traction motors and influence of manufacturing defects

---

Author:
Nikitas Ravanis

Thesis committee:
Assoc. Prof. Konstantinos Gyftakis (Supervisor)
Prof. Eftychis Koutroulis
Dr. Eleftheria Sergaki
Chania,2024

Abstract

From its first concepts and commercial steps in the late 19th century, the internal combustion engine has been a driving force for human and cargo transportation around the world. However, today we are witnesses to a global shift when it comes to the automotive world as electric vehicles are getting more and more common. That is due to the several advantages of modern electric vehicles compared to their internal combustion brethren such as higher torque, efficiency, robustness, and most importantly enabling emission-free driving through the utilization of renewable energy. The Permanent Magnet Synchronous Motor(PMSM) is a special type of Synchronous Machine that utilises permanent magnets on its rotor instead of copper winding or bars. That results in a motor with excellent capabilities that offers significant advantages over traditional Synchronous Motors in terms of efficiency, size, reliability, and performance, making them increasingly popular in various industrial and commercial applications. However, due to their wide use range, permanent magnet motors can potentially be exposed to various stresses determined by their application. These stresses can gradually deteriorate motor insulation components over time, potentially leading to failure. Stator faults pose a significant risk in electric motors, as they can rapidly escalate into catastrophic breakdowns, and are directly connected with insulation system quality. This thesis aims to have PMSM poles undergo a variety of stresses and to use the produced degradation data to investigate the suitability of Frequency Response Analysis (FRA) as a quality assessment tool for PMSM pole insulation systems. To accomplish that, first a comprehensive equivalent circuit model for PMSM stator poles and their mounted armature coils, in their respective healthy state, will be showcased. The parameters of the aforementioned model are extracted from experimental results from various tests carried out on healthy poles. Analysis of the model will give us insight on the behaviour of the Frequency Response Analysis graphs when model parameters change in value. Finally, we will test the reliability of Frequency Response Analysis as a quality assessment tool by selecting poles that show weakness in the insulation system originating from their healthy state data and poles that exhibit a strong insulation system, and comparing their insulation degradation process during the accelerated ageing cycles with the ultimate goal of evaluating the reliability of FRA as a quality assessment technique to discern defective poles from the final motor assembly.

Περίληψη

Από τις πρώτες του εκδοχές και εμπορικά βήματα στα τέλη του 19ου αιώνα, ο κινητήρας εσωτερικής καύσης υπήρξε κινητήρια δύναμη για τη μεταφορά ανθρώπων και φορτίου σε όλο τον κόσμο. Ωστόσο, σήμερα είμαστε μάρτυρες μιας παγκόσμιας αλλαγής όσον αφορά τον κόσμο της αυτοκινητοβιομηχανίας, καθώς τα ηλεκτρικά οχήματα γίνονται όλο και πιο κοινά. Αυτό οφείλεται στα πολλά πλεονεκτήματα των σύγχρονων ηλεκτρικών οχημάτων σε σύγκριση με τα παραδοσιακά εσωτερικής καύσης, όπως η υψηλότερη ροπή, η απόδοση, η στιβαρότητα και το σημαντικότερο η δυνατότητα οδήγησης χωρίς εκπομπές μέσω της χρήσης ανανεώσιμων πηγών ενέργειας. Ο Σύγχρονος Κινητήρας Μόνιμου Μαγνήτη (PMSM) είναι ένας ειδικός τύπος Σύγχρονης Μηχανής που χρησιμοποιεί μόνιμους μαγνήτες στον ρότορά του αντί για χάλκινη περιέλιξη ή ράβδους. Αυτό έχει ως αποτέλεσμα έναν κινητήρα με εξαιρετικές δυνατότητες που προσφέρει σημαντικά πλεονεκτήματα σε σχέση με τους παραδοσιακούς Σύγχρονους Κινητήρες όσον αφορά την απόδοση, το μέγεθος, την αξιοπιστία και την απόδοση, καθιστώντας τους όλο και πιο δημοφιλείς σε διάφορες βιομηχανικές και εμπορικές εφαρμογές. Ωστόσο, λόγω του ευρέος φάσματος χρήσης τους, οι κινητήρες μόνιμου μαγνήτη μπορούν ενδεχομένως να εκτεθούν σε διάφορες καταπονήσεις ανάλογα την εφαρμογή τους. Αυτές οι καταπονήσεις μπορούν να επιδεινώσουν σταδιακά τα εξαρτήματα της μόνωσης του κινητήρα με την πάροδο του χρόνου, οδηγώντας τον ενδεχομένως σε αστοχία. Σφάλματα στον στάτη αποτελούν σημαντικό κίνδυνο στους ηλεκτροκινητήρες, καθώς έχουν γρήγορη πρόοδο, μπορούν εύκολα να οδηγήσουν σε καταστροφή του κινητήρα και συνδέονται άμεσα με την ποιότητα του συστήματος μόνωσης. Αυτή η διπλωματική εργασία στοχεύει στην επιταχυνόμενη γήρανση πόλων PMSM με ποικιλία κατανοήσεων και να χρησιμοποιήσει τα παραγόμενα δεδομένα υποβάθμισης της μόνωσης τους για να διερευνήσει την καταλληλότητα του Frequency Response Analysis (FRA) ως εργαλείο αξιολόγησης ποιότητας για συστήματα μόνωσης πόλων PMSM. Για να επιτευχθεί αυτό, θα παρουσιαστεί πρώτα ένα ολοκληρωμένο μοντέλο ισοδύναμου κυκλώματος για πόλους στάτορα PMSM συμπεριλαμβανομένων των τοποθετημένων πηνίων οπλισμού τους, στην αντίστοιχη υγιή τους κατάσταση. Οι παράμετροι του προαναφερθέντος μοντέλου εξάγονται από πειραματικά αποτελέσματα από διάφορες δοκιμές που πραγματοποιήθηκαν σε υγιείς πόλους. Η ανάλυση του μοντέλου θα μας δώσει μια

εικόνα για τη συμπεριφορά των γραφημάτων του FRA όταν λαμβάνει χώρα αλλαγή στην τιμή των παραμέτρων του μοντέλου. Τέλος, θα ελέγξουμε την αξιοπιστία του FRA ως εργαλείου αξιολόγησης ποιότητας επιλέγοντας πόλους που παρουσιάζουν αδυναμία στο σύστημα μόνωσης τους λόγω κατασκευαστικών ατελειών καθώς και πόλους που παρουσιάζουν ισχυρό σύστημα μόνωσης, συγκρίνοντας τη διαδικασία υποβάθμισης της μόνωση κατά τη διάρκεια της επιταχυνόμενης γήρανσης με απώτερο στόχο την αξιολόγηση της αξιοπιστίας του FRA ως τεχνικής αξιολόγησης ποιότητας για τη διάκριση ελαττωματικών πόλων από την τελική συναρμολόγηση του κινητήρα.

Keywords

Traction Motors, Yokeless and Segmented Armature Motor, Condition Monitoring, Fault Modelling, Equivalent Circuit Modelling, Frequency Response Analysis, Nyquist Diagrams, Manufacturing Defects and Tolerances, Accelerated Multifactor Ageing, Quality Assessment.

Acknowledgements

This thesis is the based on the results of a group research project. With this statement, I would like to express my gratitude towards the members of TEAMstress and fellow students at the Technical University of Crete, Antonios Douvaras Dimitrios Chronopoulos and Dimitrios Glykos, for their dedication, exceptional collaboration and work ethic during the project's duration. Special thanks are also extended towards Athanasios Malisovas for his technical assistance.

Towards my instructor, mentor, and supervisor of this research project, Associate Professor Konstantinos N. Gyftakis, I would like to say a big heartfelt thank you for all the time and effort he invested towards this project and to me personally throughout the years of our collaboration and communication in our faculty. His mentorship, insightful expertise, and collaboration played a pivotal role towards the completion of this work and my personal development.

Towards the other members of the thesis committee, Professor Eftyxios Koutroulis and Doctor Segraki Eleftheria, I extend my appreciation and gratitude for their feedback, which refined the quality of my research.

Last but not least, I extend my deepest gratitude to my family and friends, whose unwavering support, encouragement, and love have been my anchor throughout this journey and for believing in my potential even during moments when I doubted myself.

Table Of Contents

List of Figures

List of Tables

1 Chapter 1: Introduction

1.1 Benefits of Electric Vehicles

Fossil fuels such as coal, oil, and natural gas have multiple good properties ranging from high energy density and versatility to low extraction costs. As such, they have made themselves a cornerstone of the modern world. However, it's important to acknowledge that while fossil fuels offer these benefits, their usage also comes with significant environmental and societal challenges [11], such as greenhouse gas emissions, air and water pollution, and contribution to climate change. Thus, there's a growing urgency on transitioning to cleaner and more sustainable energy sources.

As of the last two decades, renewable energy sources have made great progress towards the goals of reducing carbon footprint and creating a sustainable energy landscape. Many countries have realized that relying on fossil fuels for their energy supply has significant drawbacks towards energy stability and climate change. Renewable energy is becoming more important for communities, regions, and countries to grow economically and socially. Politicians and governments have taken notice of the growing economic advantages tied to the renewable energy sector, leading to the implementation of supportive policies for renewables, as well as adjustments in regulations and deregulation within specific areas of the power market [12].

Given what has been said, encouragement and endorsement of electric vehicle (EVs) as a prevalent means of large scale emission-free individual mobility can have positive impact on a global scale, on society, the economy as well as the environment.First and foremost, EVs use electric energy to power their motors. Electric energy is a clean form of energy due to its potential to be generated from renewable sources with minimal environmental impact. Therefore, it is safe to say that EVs will play a pivotal role to pave the way to full renewable energy integration [13]. Naturally, with electric production being strongly dependent on non-renewable sources, electric motors cannot yet be considered emission-free. Despite that, electric motors can be considered more efficient than conventional combustion engines. Firstly, the electric machine's duality as a motor and generator can efficiently recover, the otherwise wasted in a conventional combustion engine powered vehicle, kinetic energy during braking. Secondly, as shown in Fig. 1.1, traditional combustion motors operate on a really low efficiency percentage since they have to operate in different conditions (torque and speed) often far away from the optimal operating point. As such, the environmental advantages of EVs cannot be understated as the world tries to shift towards a more sustainable future. On the other hand, the transition to electric vehicles creates economic opportunities, including job creation in manufacturing, maintenance and the development of charging infrastructure. Furthermore, the widespread adoption of EVs drives innovation in traction motors,

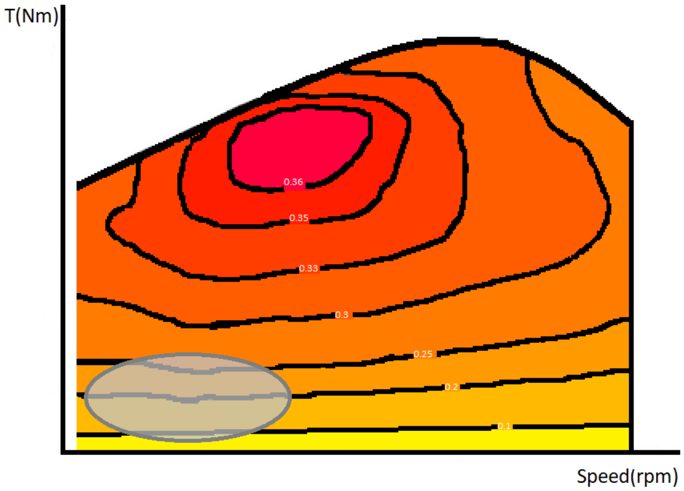

Figure 1.1: Typical efficiency chart of an internal combustion engine in function of torque M and speed.The grey spot indicates the region that is used mostly during normal vehicle driving.

batteries, energy management systems and autonomous features [14], leading to advancements not only in transportation but also in other sectors, such as energy storage and grid management. The following chapter expresses some basic technical capability requirements that an electric motor fitted in a Full Sized Vehicle should exhibit (Section 1.2), as well as a review of electric motor topologies best fitted for the task (Section 1.3). After this chapter, the thesis will focus exclusively on the Permanent Magnet Synchronous Machine.

1.2 Technical Capability Requirements of Traction Motors for Full Sized Vehicles

As of today, a lot of innovation-driven research and experimentation has taken place around the subject of traction motors in the automotive industry. As a result, a wide range of electric motors are used to propel various types of electric vehicles. However, an electric vehicle must be able to meet basic utility functions common to any type of vehicle. So we reasonably conclude that there is a set of properties that should be present in every motor intended for traction drive use. The aforementioned properties are presented below.

- Good efficiency, especially during low power operation points.
- Compact design
- High power density
- Wide speed range without the presence of a gearbox
- High torque at low speeds
- High power at high speeds
- Sufficient mechanical robustness
- Long lifecycle and high reliability
- Low to no acoustic noise generation
- Excellent power factor in most operation points.

1.3 Showcase of Potent Motor Topologies

As electric vehicles have been a hot topic recently, there has been a lot of research around what kind of electric motor is optimal for EV use. With a huge array of different motor designs available to choose from, as shown in Fig. 1.2, there is no clear answer to this question as it heavily comes down to application dependence. In this section, motor topologies with potential to be used in electric vehicles are briefly examined.

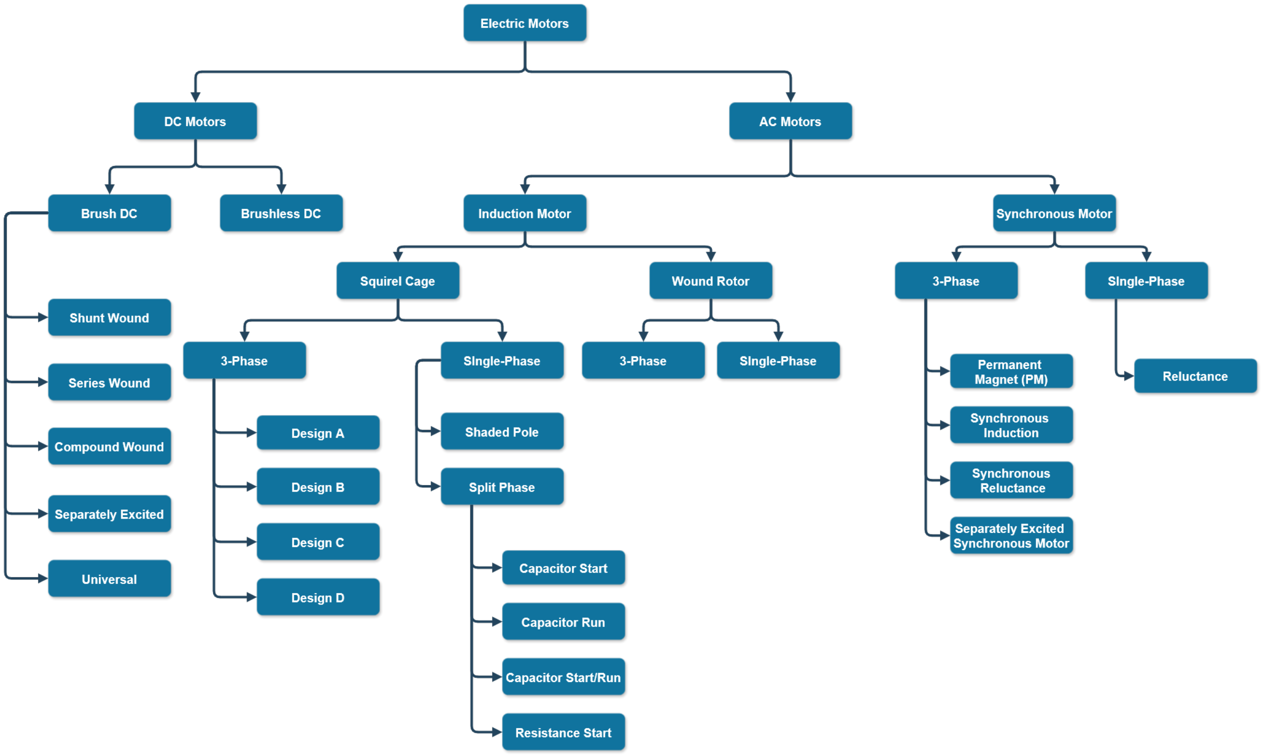

Figure 1.2: Diagram of different types of electric motors

1.3.1 Brushed DC Motor

The Brushed DC motor utilizes a commutator and brushes, which transform DC current within an armature coil into AC current. Its construction is relatively simple compared to other types of motors, while providing high torque at low speeds. Furthermore, Brushed DC motors can be controlled using simple electronic circuits as they operate with DC power, so they are very attractive for low-cost applications as an inverter is not essential [15]. Finally, advancements in motor design have made DC brushed motors more compact and lightweight compared to some other motor types [16].

Despite having high torque at low speeds, this topology is usually no longer used for automotive purposes. The presence of commutating brushes which need to transfer the whole power in the rotor is enough to make this topology unattractive. Friction between brushes and commutators make frequent maintenance necessary, generates electromagnetic interference and makes high speeds unattainable [17] [18].

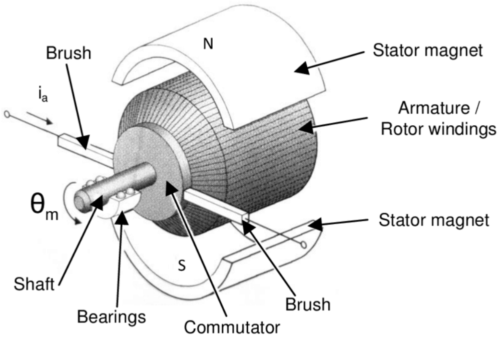

Figure 1.3: Model of a Brush DC Motor [1]

1.3.2 Asynchronous Motor

The asynchronous motor, or known as well as the induction motor Fig 1.4, is one of the most used motors globally. Firstly, its manufacturing cost is reasonably low, partially due to the absence of rear earth permanent magnets. Also, it has a simple and robust design with most topologies having no mechanical moving parts, which means high reliability and low maintenance requirements [19]. Employing an inverter-fed induction machine enables the attainment of both high starting torque and low starting current. Thus, compared to conventional induction machines designed for constant supply frequency operation, certain limitations are eliminated [2].

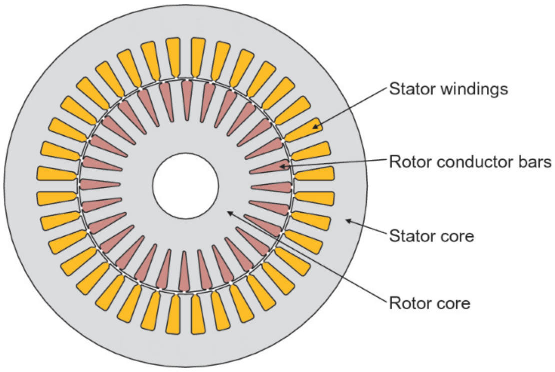

Figure 1.4: Cross section of the Induction Motor

Unfortunately, the induction machine presents a set of undesirable traits for vehicular use. Firstly, its power factor is lacking, especially at the reduced power region, and worsens with rotor flux loss present [2]. Consequently, the necessary inverter needs to be oversized to supply active power. Also, excessive heating in the rotor from rotor copper losses has the potential to lead to unacceptably high temperature of the rotor core, shaft and bearings, even if using liquid cooling for the rotor [20]. Finally, in conventional induction motors, the range of constant power usually spans from 2 to 3 times the base speed. Despite this range being expandable to 4 to 5 times the base speed in traction versions by flux weakening [19], this still is a limitation of the induction machine compared to other topologies that can have a constant peak power on a wider speed range. As such, its employment for high speed applications, like travelling at cruising speeds, is recommended with a variable transmission gearbox. The gearbox's weight and volume further decreases its subpar power density, caused by its bulky design.

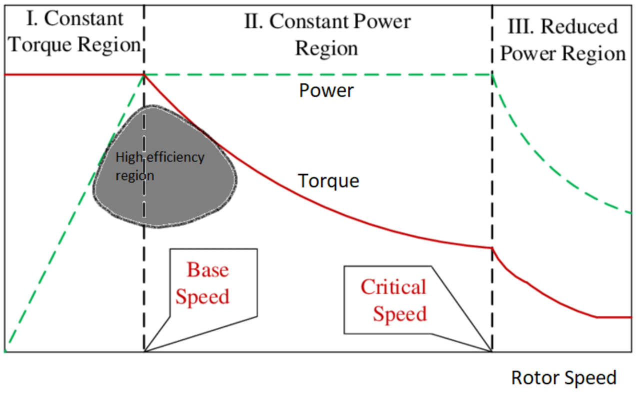

Figure 1.5: Standard Torque-power/speed graph of inverter fed Induction Machine. The gray area represents the high effieciency area as high torque and high power are present [2].

1.3.3 Separately Excited Synchronous Motor

The Separately Excited Synchronous Motor (SSM), or also known as Wound Rotor Synchronous Motor (WRSM), is a wound-rotor synchronous AC motor that uses a DC excitation winding in the rotor. It is a traction motor without rare earth magnets, with great control freedom given by the possibility of controlling the rotor current [21] and with torque at low speeds as well. With the introduction of inductive energy transfer systems replacing the obsolete use of brushes, the SSM is a rather promising topology as a traction drive. As such, leading electric vehicle manufacturers prefer this topology, including Renault and BMW [20] [22], as magnet-free alternatives to permanent magnet options.

However, the SSM has drawbacks that hinder its overall appeal. First of all, heat

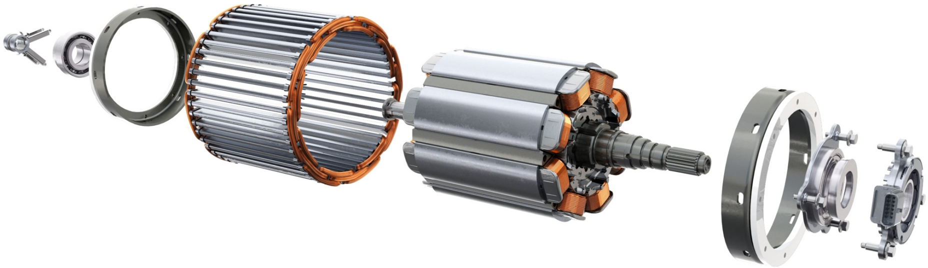

Figure 1.6: Renault SSM motor [3].

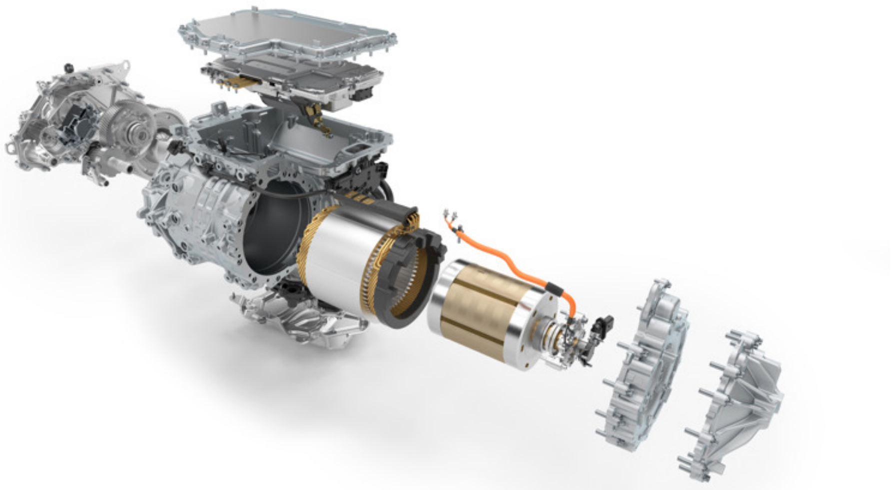

Figure 1.7: BMW 5th generation eDRive powered by an SSM [3].

generated in the rotor due to copper losses negatively affects the continuos power of the machine, thus limiting its performance capabilities. Secondly, the inductive energy transfer system which tackles the commutating brush issue come with its own challenges. This approach comes with the disadvantage of escalating system complexity, posing challenges in rotor current control, especially in swiftly eliminating it to ensure rapid rotor demagnetization in case of an emergency.

1.3.4 Switched Reluctance Motor

Switched Reluctance Motors(SRM), Fig 1.8, emerge as a compelling candidate for significant advancements within the realm of motor technology. Offering a spectrum of advantages, this motor topology presents a fertile ground for innovation and enhancement. One of its prominent strengths lies in the combination of its capacity to deliver constant toque and constant power for a wide speed range [2], making it adept for high speed applications. Unlike other motor types, SRMs do not rely on permanent magnets, rendering them remarkably cost-efficient both in terms of manufacturing and maintenance. Another notable advantage stems from the absence of rotor coils, eliminating associated losses at the rotor copper and contributing to overall efficiency. Furthermore, reluctance motors exhibit fault tolerance capabilities, a crucial trait for electric vehicular utilization. Consequently, the SRM presents a fertile ground for ongoing research and development efforts aimed at unlocking their full potential and further refining their performance characteristics [19].

Despite its strengths, the SRM also harbors several drawbacks that warrant consideration. One notable limitation is the tendency for these motors to generate high levels of acoustic noise during operation across all speed ranges. Additionally, the motor produces torque ripples that stem from its salient pole design. Another drawback is that the motor needs some compromise between constant power and constant torque capabilities which is directly tied to its rotor pole design, thus resulting in a motor with stiff performance characteristics after its construction. Finally, the control mechanisms governing reluctance motors can be intricate, requiring sophisticated systems to optimize performance effectively.

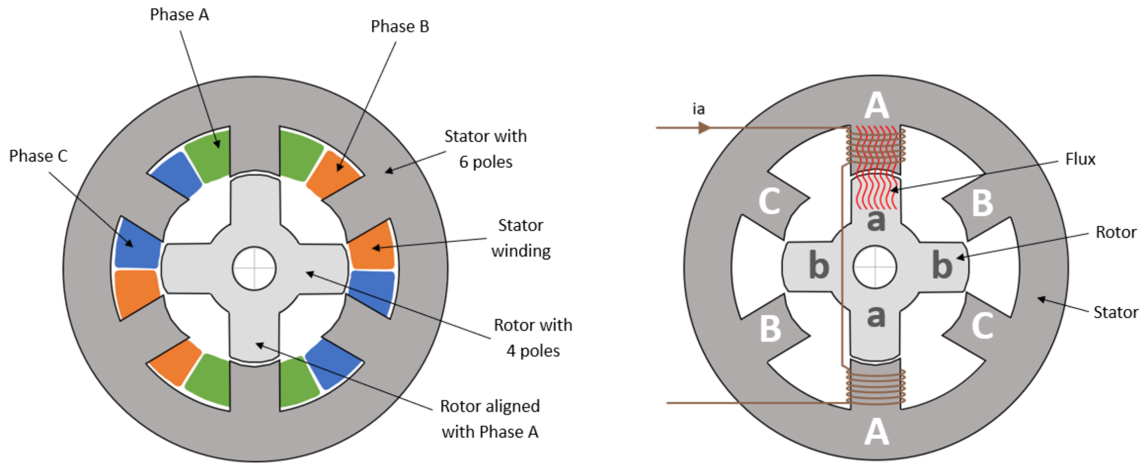

Figure 1.8: Showcase of an 6/4 Switched Reluctance Motor [4].

1.3.5 Synchronous Reluctance Motor

The Synchronous Reluctance Motor does not need any permanent magnet and its manufacturing costs are extremely low. This in combination with its wide constant power range makes it one of the cheapest solutions for applications that high rotational speeds while maintaining smooth operation is vital. Furthermore, it is very safe since the absence of permanent magnets means that in case of an inverter failure it does not produce any braking torque. Finally, the synchronous reluctance motor has exceptional high overload capability as there is no fear of demagnetization of its permanent magnets [23], something that is coveted for a traction motor.

This topology suffers from a notable disadvantage in torque density, rendering it less appealing for mid-range electric vehicles. Moreover, the power factor typically remains low due to a substantial portion of the stator current being allocated to rotor magnetization without contributing to torque generation. A favourable power factor stands as a crucial attribute for achieving optimal electric motor efficiency. Consequently, designing a reluctance motor with comparable efficiency to other topologies while ensuring a significantly improved power factor presents a challenge [6].

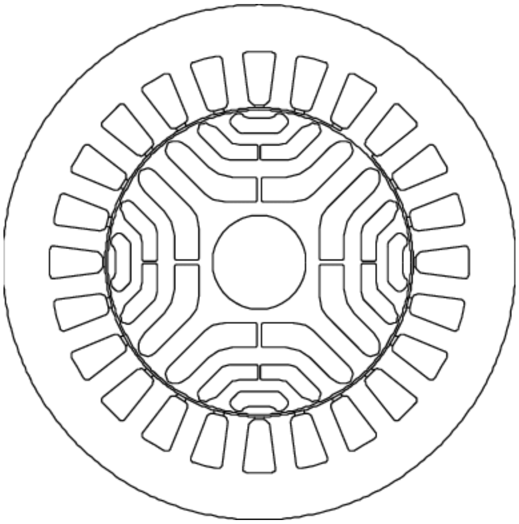

Figure 1.9: Cross section of a Synchronous Reluctance Motor [5].

1.3.6 Permanent Magnet Synchronous Motor Topologies

This family of motors have emerged as the most prominent candidates for electric vehicular use and have been widely used as EV (or hybrid EV) traction drives across the automotive world [24]. All the motors included in this group utilize rare-earth permanent magnets instead of copper windings. Absence of heat generated in the rotor by copper losses means Permanent Magnet Synchronous Motor are machines whose peak power is less limited by thermal issues, but mostly by their magnetic properties. The examined topologies in this section are shown in Fig. 1.10.

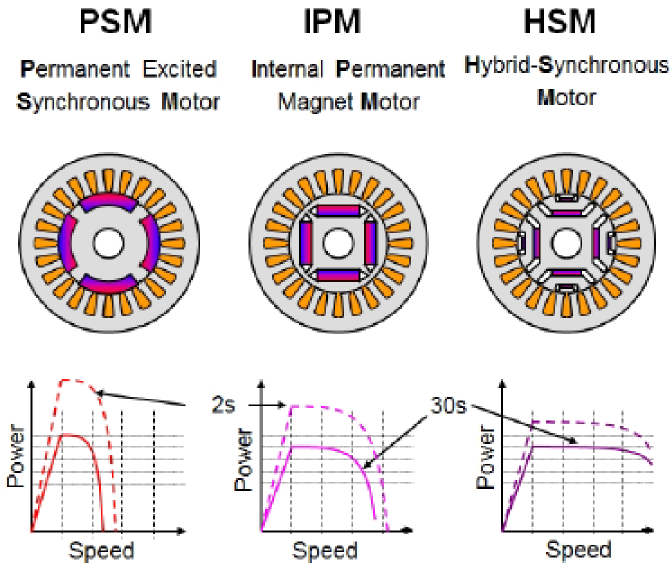

Figure 1.10: Showcase of different permanent magnet synchronous machines each with its respective power - speed chart. [6].

Surface Mounted Permanent Magnet Motors

The Surface Mounted Permanent Magnet Motors, or also known as the Permanent Excited Synchronous Motor Fig 1.10 left side, provide high torque at low speed, remarkable efficiency, high power factor as well as excellent power density attributed to its combination of small size and high power. All the above traits makes it one of the best suited electric motors for high performance applications like motorsports. Furthermore, its simple design in combination with its small size makes it a strong option to explore in-wheel vehicular propulsion systems.

Its drawbacks are that the peak speed is often limited, since the large amount of permanent magnets induce very high voltages in the stator at high speeds [2]. Simultaneously, flux weakening operation to address the above issue is expensive regarding stator current while also endangering with demagnetization the exposed rotor magnets. To conclude, most configurations of this topology utilize a large quantity of permanent magnets containing expensive rare earth materials such as neodymium and dysprosium [24].

Internal Permanent Magnet Motors

The Internal Permanent Magnet Motor(IPMM), Fig 1.10 center, shares most of its attributes with the SMPMM. Instead of relying on solely its permanent magnets, it incorporates reluctance to some extent, sacrificing a bit of torque at low speeds to extend its constant power range while also lowering its manufacturing costs. Additionally, by embedding the magnets within the rotor iron, they are effectively shielded from the demagnetizing armature reaction field, making flux weakening operation safer. Finally, in case of a fault in the inverter it produces less short circuit torque, making its operation safer.

Downgrades compared to the SMPMM consist of, higher leakage flux by a significant margin, resulting in lower torque at low speeds. Furthermore, the integration of reluctance results in a design that is notably more elaborate and intricate.

Hybrid-Synchronous Motor

This topology, Fig 1.10 right side, tries to improve the capabilities of the SRM. To that end, permanent magnets are inserted in the flux barriers to improve torque density and rectifying the subpar power factor of the SRM [23]. Furthermore, while the Hybrid-Synchronous Motor produces more short circuit torque compared to its non-permanent magnet assisted counterpart, the risk involved is less compared to pure permanent magnet motors [6]. Moreover, as it relies less upon permanent magnets for its operation we can opt to using non rare-earth less powerful magnets, reducing its cost.

However, despite the HSM relying less on strong permanent magnets the risk of demagnetization is never zero, making its overloading less of an option [23]. Also, the PM-tied performance related traits of high torque and power density are downgraded.

Permanent Magnet Brushless DC Motor

The Permanent Magnet Brushless DC motor(PM-BLDC), Fig 1.11, can be regarded as the DC counterpart of the Surface Mounted Permanent Magnet Motor. Both topologies have their permanent magnets mounted on the rotor surface, resulting in their inductances along the d and q axes being closely aligned, resulting in negligible reluctance torque [25]. Like the Surface Mounted Permanent Magnet Motor, it can achieve high torque at low speed, noteworthy efficiency at high speeds, high power factor as well as excellent power density.

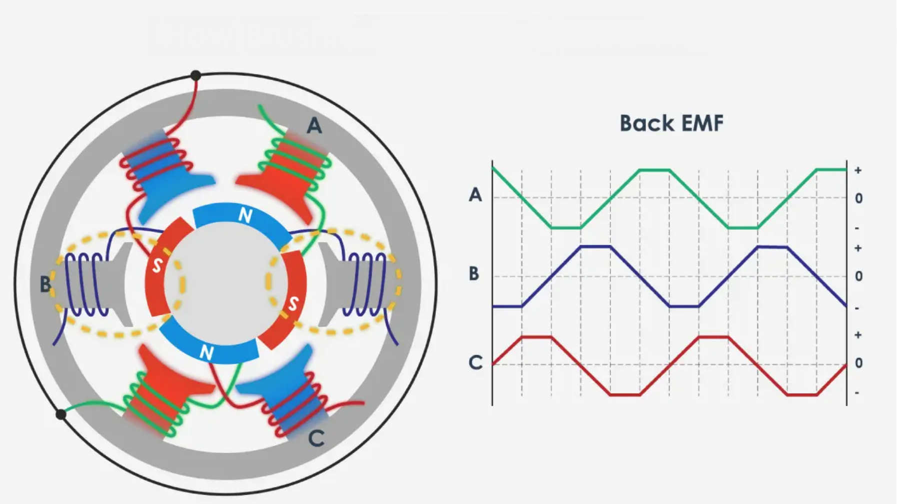

Figure 1.11: The BLDC motor cross-section with its back EMF characteristic [7].

One of the main differences of the BLDC motor and its AC counterparts is in the shape of their back EMF. While the back EMF of standard AC permanent motors is sinusoidal, the BLDC's back EMF has a trapezoidal shape. Worth highlighting is that the interplay between trapezoidal current and magnetic field in the motor can generate a higher torque output compared to sinusoidal counterparts, giving BLDC motors an

advantage in terms of torque density [26]. Nonetheless, this enhanced performance introduces its own challenges. Trapezoidal shaped back EMF results in torque ripples and means that constant-power operation for the BLDC is more challenging. As the back EMF waveform no longer resembles a sine, torque ripples are common and standard flux-weakening control methods are no longer convenient. Nevertheless, constant-power operation can be achieved through advanced conduction angle control [27].

1.3.7 Axial flux Permanent Magnet Machine

The Axial Flux Permanent Magnet (AFPM) machine presents an appealing substitute for cylindrical Radial Flux Permanent Magnet (RFPM) machines because of its flat shape, condensed build, and remarkable power density [28]. Furthermore, it is commonly acknowledged in the literature that AFPM machines typically exhibit superior torque densities and efficiencies compared to their radial flux counterparts [29]. This is partially attributed to the inherent advantages of the AFPM design concerning motor cooling.

Additionally, AFPM machines are adept at functioning as generators for small to medium power needs. Their ability to accommodate numerous poles makes them perfect for low-speed tasks such as electromechanical traction drives, rendering them highly compatible with electric vehicles [30]. From the vast variation of this type of electric machine, this thesis will focus on the toroidally wound internal stator (TORUS) machine and its close relative, the Yokeless And Segmented Armature (YASA) machine.

Toroidally Wound Internal Stator machine

The Toroidally Wound Internal Stator machine is a single stator dual rotor axial flux permanent magnet motor configuration and is one of the best performing. This topology has two versions, the NN Torus-S and the NS Torus-S, and both will be thoroughly examined.

Firstly, the NS Torus-S, Fig 1.12 right, is named after the fact that in this machine, each rotor's magnets that are facing across one another have opposite polarity. According to [31], the iron yoke of this topology is allowed to be narrow as the magnetic flux doesn't path through it, so it is in no risk of magnetically saturating. The short yoke cuts losses while reducing the volume of the motor elevates power density. Nonetheless, a lap round copper cable winding is necessary to generate torque [28]. Consequently, the machine encounters challenges such as a low fill factor and extended end-windings, leading to an enlarged outer diameter, reduced power density, and heightened losses.

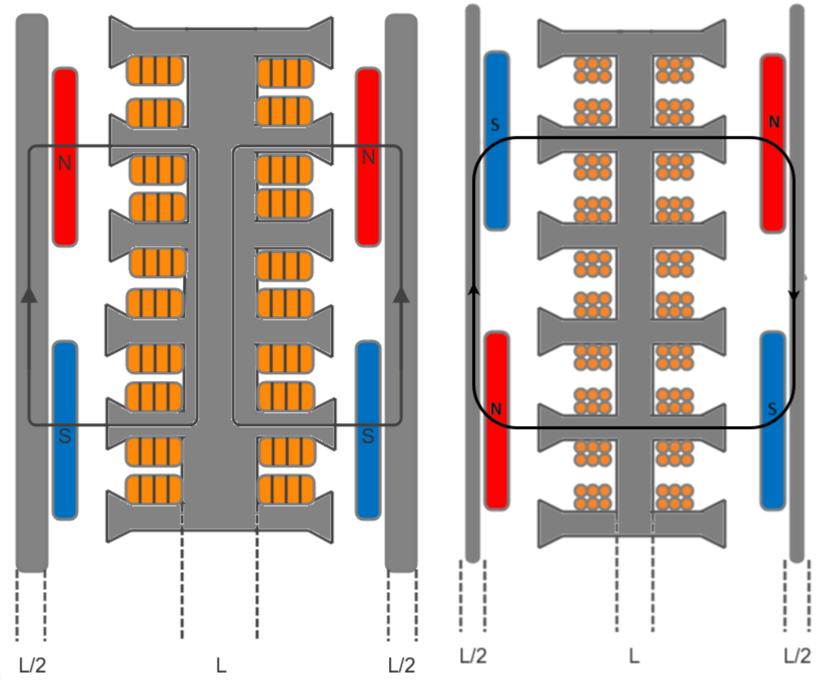

Figure 1.12: NN Torus-S (left) and NS Torus-S (right) axial flux motors with their respective magnetic flux paths. In the NN configuration the stator yoke needs to be larger than the one in the NS as all of the magnetic flux of the motor transverses through it and we want to avoid magnetic saturation of the iron core.

On the contrary, in the NN Torus-S, Fig 1.12 left, magnets across each other possess the same polarity. This means that all the magnetic flux from the motor paths through the stator iron. In order to avoid magnetic saturation losses in the iron core, the stator yoke needs to be larger than the one in the NS Torus-S. The larger stator increases the motor volume, which in turn reduces power density. However, a back-to-back square copper cable winding with high fill factor can be employed. This significantly minimizes the extension of the end windings, thereby enhancing the power density and efficiency of the NN Torus-S type machine [28]. In summary, both machines demonstrate comparable performance levels, although the NS Torus-S has better peak attributes [31].

1.3.8 Yokeless and Segmented Armature Motor

The Yokeless And Segmented Armature (YASA) Motor, Fig 1.13, is a single stator double rotor axial flux machine that is regarded as an advancement upon the aforementioned TORUS topologies [32]. The YASA fundamental qualities lie on the NS Torus S design while taking a step further, discarding the iron stator yoke. This is possible due to the yoke not being necessary for reasons other than mechanical support. The Yokeless design has no iron core related losses, bolstering motor efficiency while getting rid of unnecessary weight. Additionally, attaching a basic coil with shortened end windings to each tooth, and employing square wire, enables achieving a high fill factor. Hence, it is safe to say that the YASA topology combines the main strong points of the two aforementioned TORUS topologies [31]. This leads to a notable increase in power density and torque density.

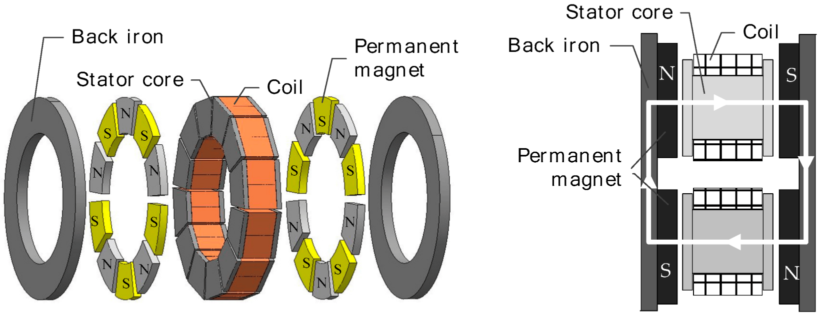

(a)

(b)

Figure 1.13: (a) Yokeless And Segmented Armature topology (b) Magnetic flux path [8].

However, the exceptional performance capabilities of the YASA motor are also tied to inherent drawbacks. Firstly, the magnets being mounted on the surface of the two rotors makes vector control difficult and endangers them with demagnetization [8], especially during flux weakening operation. This in combination with high eddy current losses at high frequencies [31] may restrict the achievable field-weakening range, limiting the motor's ability to operate efficiently at high speeds. Furthermore, this motor topology has numerous design parameters, making its design process complex.

1.4 Scope and Motivation

Research on experimental modelling of complex components for prognosis-based purposes remains limited, particularly in capturing real-life effects and manufacturing characteristics. However, this level of detail in modelling is essential for reliably interpreting results from experimental testing. In this thesis, a detailed experimental model of stator poles, complete with the windings of Permanent Magnet Synchronous Motors (PMSMs), is developed as a tool to connect the data generated from accelerated ageing tests with the degradation of the insulation system properties. The ultimate goal is to evaluate the reliability of FRA as a quality assessment technique to discern defective poles from the final motor assembly.

1.5 Outline

The thesis is organised as follows:

- Chapter 2: The roots and the manifestation of common faults that take place in PMSMs as well as potential underlying causes will be discussed. Also, a brief literature review on fault modelling is done for each type of fault.
- Chapter 3: In this chapter, all the decisions made during the development of the pole equivalent circuit model proposed in this work are revealed.
- Chapter 4: Here the behaviour of the impedance FRA graph when change in a single model parameter takes place is analysed and a brief parameter analysis concerning the equivalent circuit model is made.
- Chapter 5: The accelerated ageing procedures, cycle strategy and results are discussed here. The validity of Frequency Response Analysis as a quality assessment tool is also be tested in the chapter.
- Chapter 6: General remarks about the results showcased in the thesis and potential future work are stated here.

2 Chapter 2: Condition Monitoring and Fault Modelling in Permanent Magnet Synchronous Motors

As it was discussed above, Permanent Magnet Synchronous Motors are really popular in the electric vehicle industry. That is because their performance profile best satisfies the requirement for the propulsion of a full sized vehicle. As the essential part of a traction drive, any fault or failure in the PMSM can result in severe repercussions, particularly during vehicle operation, namely prolonged downtime, property damage, and potentially human casualties [33]. Though the PMSM are generally robust, being mounted on a moving platform, that is the electric vehicle, usually means exposure to non-ideal operating conditions. The potential added stress originating from these conditions in combination with inherent asymmetries and manufacturing defect of the motor as well as prolonged operation induce magnetic, mechanical and electrical faults on the machine [34] [35]. This chapter will name stator and rotor faults that commonly occur in the PMSM, exploring the underlying conditions responsible for them, while also suggesting prognostic and diagnostic methods to accurately pinpoint them and prevent catastrophic consequences.

Prior to that, the term Condition Monitoring regarding electrical motor faults will be defined. It is widely accepted that the Condition Monitoring term can be divided into two sub-areas which will be discussed below: fault diagnosis and fault prognosis.

Fault Diagnosis on the other hand takes place after the fault has occurred. Its main goals are detecting when a fault is present in the machine, identifying what kind of fault that is and pinpointing the location where the fault has taken place, and all of that as soon as possible. This means that a good diagnostics method needs to recognise the fault at an early stage during normal motor operation. In this way, necessary action can take place to prevent catastrophic repercussions from occurring.

Fault Prognosis is the art of prediction of motor faults before they come to fruition. Its main goal is the estimation of the time for which the machine in question will continue to function properly with only using available observations and past related historic archives, so that maintenance can be scheduled in a convenient and timely manner. Therefore, fault prognosis is tightly related to material science as well as motor stress and ageing mechanisms.

Unfortunately, today there is no integrable systematic prognostic method available that can be applied in intelligent maintenance systems, making expert human involvement mandatory. On that topic, several prognostic methods have been submitted in technical literature, despite most of them still facing some kind of problem. These methods can be divided into one of two approaches: the data-driven approach and the model-based approach.

The data-driven approaches are constructed based on system operation data like spectrometric data and calibration data, as well as input and output real-time measurements to model the system degradation behaviour. The main strength of a data-driven method is its signal processing ability to draw information relevant to prognostic decisions from high-dimensional and potential noisy data and the vast system operation data that is available today. However, this means that the method cannot take into account random events into consideration, as it relies on the consistency of the statistical characteristics of the data.

The model-based approaches are built on the outcomes of consistency checks between the output of an elaborate mathematical model and the one of a real system. This is a time-consuming procedure as time must be spent developing the model as well calibrating it to match the behaviour of the real system during different scenarios. The primary limitation of the model-based approach is its lack of practicality, as the fault type is often unique, varies between components, and is difficult to identify without disrupting machine operation.

A fundamental aspect of any effective condition monitoring technique is comprehending the electrical, magnetic and mechanical behaviour of the machine both in its healthy state and under faulty conditions. Designing and validating these techniques usually requires elaborate and detailed mathematical models or highly accurate equivalent circuits that enable extensive computer simulation for performance prediction and fault identification purposes concerning the motor. This makes motor fault modelling an invaluable tool for studying the operational characteristics of motors under both normal and faulty conditions without the need for destructive testing [36].

2.1 Magnetic Defect Faults and Fault Modelling

Magnetic faults are exclusive to the permanent magnet motor and are related to the dysfunction of the permanent magnet system. Magnetic defect faults occur instantly, have a negative effect towards motor performance and efficiency, their prognosis is extremely difficult and pose a threat capable of incapacitating the machine [37] [38]. Thus, fault mitigation methodologies are essential during the motor design stage to prevent magnetic faults from taking place.

2.1.1 Permanent Demagnetization Fault

The Permanent Demagnetization Fault is a common and instant fault that affects the PMs of the rotor in a PMSM. Its roots can be found from the hysteresis loop, Fig 2.1, of the ferromagnetic material used for the production of the magnet. The hysteresis loop depicts how the magnetization of the ferromagnetic material changes when placed inside an alternating magnetic field that can drive it to magnetic saturation. As we can see for Fig 2.1, after the material has been driven to magnetic saturation from an outside magnetic field, when that magnetic field is no longer present a portion of its magnetic properties still remain, thus turning it to a permanent magnet. This residual magnetic induction of the newly born permanent magnet is called remanence.

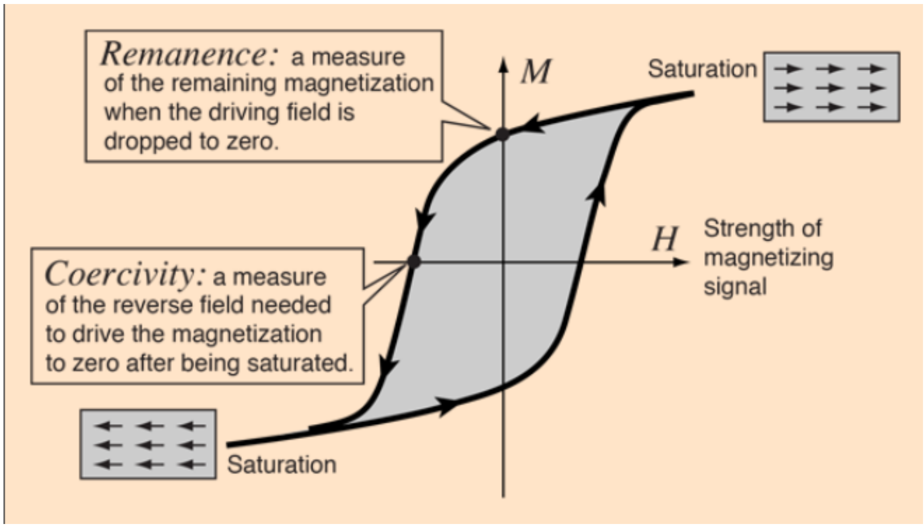

Figure 2.1: Hysteresis loop and the point of coercivity [9].

Afterwards, as we can deduce from Fig 2.1, if a reverse magnetic field is applied to the permanent magnet some of its magnetic properties are slowly lost without them being able to return to their maximum remanence status. However, once the external magnetic field exceeds a certain threshold, the magnetic polarization drops rapidly. That threshold is generally known as the knee point of the demagnetization curve, and the corresponding magnetic field strength as the knee coercivity. This is relevant because during operation if a knee coercivity able magnetic field is produced by the stator, one or more PMs of the machine are partially and irreversibly demagnetized. To make matters worse, as it can be seen in Fig 2.2, increasing the temperature of the PM slightly lowers its magnetic properties and shifts the knee coercivity point to the right, meaning that a weaker magnetic field can lead the PM to partial. To conclude, oxidation and corrosion of the machines materials are factors that can make a PMSM prone to demagnetization.

The dysfunctionality of the partially demagnetized PMs poses a great threat towards the operation of the faulty machine. Firstly, the weakened magnets diminish the motor's performance, leading to a lower torque produced [39]. If the operation of the motor doesn't cease and continues to operate under rated load, higher input stator current will be invested, increasing copper losses, elevating temperatures and thus accelerating the degradation of the insulation system [40]. Additionally, partial demagnetization increases the magnitude of

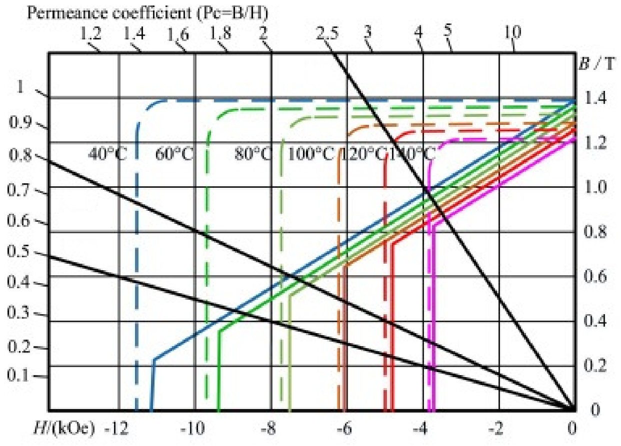

Figure 2.2: Here we can see the normal curve, solid line, and the intrinsic curve, doted line, of Nd-Fe-B permanent magnets with regard to temperature. The operation point of the magnet is located where the load line, solid black line, cuts the normal curve. If the load line cuts the intrinsic line after its knee coercivity point, the permanent magnet is subsequently partially demagnetized [10].

higher force harmonics in the components, resulting in vibrations and acoustic noise emitted from the machine while also affecting the rotor-stator attraction, altering the machine's shaft trajectory and producing cogging torque [41].

The above points combined with the wide use of the PMSM in electric vehicles make the precise modelling of the demagnetization effect a popular topic in academic literature. In [42] the authors introduced a flexible and accurate magnetic-equivalent-circuit-based model with consideration to dynamic response of the motor as well as the saturation effect. In [43] the Lumped Magnetic Circuit Model(LMCM) which is based on 2D Poisson's and Laplace's equations is proposed. Lastly, in references [44] [45] the finite element analysis was used for the analysis and modelling of the demagnetization phenomenon.

2.1.2 Broken Magnet Fault

The broken magnet fault occurs when one or more magnets of a PMSM break into two or more pieces due to some underlying cause or a defect during the magnet's manufacturing procedure. This phenomenon has a direct negative effect on the performance and the future health of the motor. When the PMSM operates with a broken magnet of a certain degree, the winding current must increase to achieve the same torque output. In these conditions, the temperature of the winding increases due to Joule losses, making highly likely the manifestation of other fault in the motor, like the inter turn fault. Moreover, these conditions make the iron nonlinearity significant and as such it cannot be ignored, making previous the calculation accuracy of a previously developed analytical model unreliable.

There are a lot of potential underlying causes for the broken magnet fault. Firstly, mechanical causes like continuous vibrations, excess magnetic forces within the machine, improper handling during transportation and/or maintenance and general wear of the motor influence greatly the mechanical integrity of the magnet. Furthermore, thermal causes like excessive heat production and thermal cycling can degrade the permanent magnets, making them brittle and more susceptible to cracks and breaking. Finally, ambient factors like exposure to harsh environmental conditions, such as moisture or corrosive chemicals, can degrade the magnets, making them more susceptible to breakage.

Errors during manufacturing of the magnet and assembly of the machine also have impact towards the occurrence of a magnet breaking during motor operation. Inherent material defects in the magnets, such as unwanted doping of the magnet material, voids, or other imperfections, can lead to structural weakness and eventual breakage. Also, poor adhesive bonding of the magnets to the rotor and poor choices during the design phase of the motor can result in detachment and breakage during operation.

Various methods are proposed in the academic literature about modelling and analysis of the broken magnet fault and its fault signatures. In [46] the severity of the broken magnet fault was modelled using a linear motor model as well as finite element analysis. A non-linear analytical model was introduced in [47] to examine the relationship between the magnet defect fault and the behaviour of a surface-mounted permanent magnet motor, with finite element analysis to verify the results.

2.2 Mechanical Faults

Mechanical faults in PMSMs are malfunctions connected with moving parts of the machine, generally speaking the rotor and the bearings. When a mechanical fault is in its early stages, generally it has neither severe nor instantaneous repercussion upon the electrical machine. However, if the fault is not detected and treated, it will progress silently and slowly as the machine operates with destructive end results.

Eccentricity is the primary indication of an underlying mechanical fault. Eccentricity is present in an electrical machine when the air gap length is not constant between the rotor and the stator. Eccentricity can be divided into two types with regard to the type of displacement that has taken place: static eccentricity and dynamic eccentricity. Static eccentricity occurs when the centre of rotation has been displaced with regard to the geometrical centre of the stator but remains stable during the rotation of the rotor. Dynamic eccentricity occurs when the centre of rotation of the rotor itself moves radial around the geometrical centre of the stator during its rotation. Mixed eccentricity is named the scenario where both static and dynamic eccentricity are present. Eccentricity in general plagues every motor ever produced, as the constructing procedure cannot by any means be perfect and defects are common. However, a well-designed and well-constructed electrical machine will have a negligible inherent eccentricity degree which poses no threat. The tricky part about eccentricity is that signature indexes can take the appearance of a different type of fault altogether, making its diagnosis difficult as false positive, false negative and/or misdiagnosis are all possible scenarios. This makes methods for diagnosing and discernment of eccentricity from other types of faults essential, making it a hot topic of scientific literature.

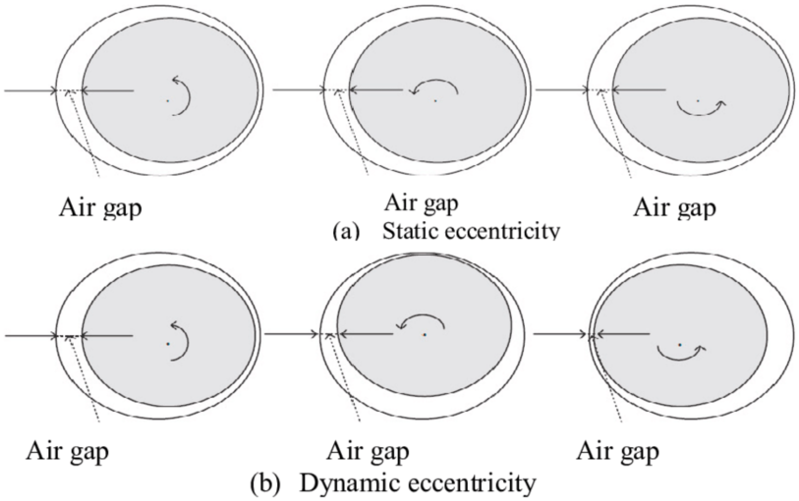

Figure 2.3: Showcase of (a) Static eccentricity and (b) Dynamic eccentricity

2.2.1 Bearing Fault

The bearing fault is the most common and probable fault that can occur to an electrical machine, with studies reporting that 40% of all motor failures are bearing related. Fault in the bearing system is responsible mostly for the dynamic eccentricity present in machines. A generic deep groove ball bearing is composed of the outer ring, inner ring and balls situated between them, as show in the figure 2.3, with lubricant applied to the moving parts of the bearing.

A lot of factors that can lead the bearing system of a machine to failure. Firstly, the deterioration of the properties of the lubricant is one of the main said factors. This is especially true for inverter fed PMSMs as the high switching frequencies in conjunction with parasitic capacitances leads to common-mode voltage and a small current circulating

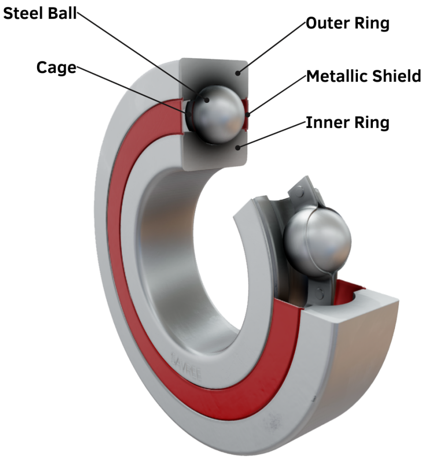

Figure 2.4: Deep groove ball bearing

through the shaft and bearings [48]. The joule losses of the circulating current increases the temperature of the bearing, thermally stressing the lubricant. At high current densities in particular, there is high risk of fluting and pitting on the surface of the bearing, resulting in vibration and acoustic noise. Moreover, as almost all the PMSMs used in electrical vehicles are inverter fed, countering the bearing fault is of great significance. Secondly, overloading of the bearings can lead to the collapse of their moving parts, leading to heavy dynamic eccentricity that has the potential to bring about the catastrophic breakdown of the machine. Finally, other mechanisms that accelerate the wear of bearings in electrical machines consist of ambient stress due to the presence of dirt, dust, moisture and/or corrosive substances in the environment that the machine operates as well as the presence of other faults such as misalignment and/or excess vibration produced by other sources.

The development of precise bearing dynamic models is essential for conducting dynamic analysis of the bearing system in electrical machines for both diagnosis and prognosis purposes. In early dynamic modelling [49] [50] [51] the authors modelled the vibration sequence of rolling bearings with single point and multiple defects, respectively, and examined how the load period and transfer path influence the vibration characteristics of the rolling bearing. In [52], the author developed a dynamical model solving it using time domain as well as frequency domain analysis, and got the non-linear response of ball bearings with a single and multiple defects.In [53] a two-degree-of-freedom ball bearing dynamic model was used for in-depth analysis and the effects of rotational speed, load, defect location and defect size on the bearing vibration response characteristics were obtained.

2.2.2 Rotor Shaft Misalignment

The rotor shaft misalignment fault is a commonly observed phenomenon in electric machines. It occurs when the rotor shaft is either bent or not aligned with the correct axis of rotation. It can be divided into two categories: angular misalignment and parallel misalignment. Angular misalignment occurs when the rotor shaft is not in parallel with the correct axis of rotation and therefore the air gap along the rotor is not fixed, leading to an unbalanced electrical machine. Parallel misalignment on the other hand of the rotor shaft and has the same effects as static eccentricity, while being its primary cause.

Misalignment may be present due to various factors such as improper assembly of machines, thermal distortion of machines and asymmetry in applied loads. Furthermore, even after the utilisation of sophisticated alignment techniques like laser alignment, the rotor system is bound to have some residual misalignment present even during perfect operation conditions and will develop silently over the lifespan of the machine making prognosis based maintenance checks essential. Despite all that, misalignment can be kept within reasonable levels with good design choices and proper operation of the machine.

Accurate prediction of vibration response of the misaligned rotor strongly depends on the realistic modelling of the misalignment vibration. In [54] the authors explored the relationship between misalignment and load oscillation using the motor current signal analysis (MCSA) method together with an equivalent circuit based on experimental results. A detailed three-dimensional magnetic equivalent circuit model while taking into account the axial direction of the rotor with varying severity of static eccentricity based on the axial position of the rotor shaft was introduced in [55].

2.3 Electrical Faults

Electrical faults in PMSMs are only found in the stator, as that is the only part of the machine that is electrified. They are related to failures of the stator pole insulation system leading to excess heat production, rotor permanent magnet demagnetization and if left unchecked catastrophic breakdown of the motor.

2.3.1 Turn-to-Turn fault

The Turn-to-Turn fault, also known as the inter-turn fault, is a fast progressing fault that takes place when a number of turns in a phase of the stator winding are internally shorted. Most of the time after post-fault analysis, this fault is attributed to a weak turn-to-turn insulation [56]. Because of the rotating magnetic field of the machine, voltage is induced in the shorted turns producing a circulating short current. According to [57], even during a fault of low severity, the short circuit current is greater than the rated stator current. This increases the temperature of the shorted turns greatly, endangering the overall health of the machine and necessitating the fault's early detection.

Inter-turn faults are a problem especially for the PMSM due to the presence of the magnets. Firstly, in a fault-tolerant methodology, even if the turn-to-turn fault is detected in a timely manner, the magnetic decoupling between the stator poles and the rotor magnets is difficult by external means [33]. This in combination with the fault's rapid evolution gravely endangers the machine. Furthermore, the ability of the inter-turn fault to produce high circulating current in the shorted turns means that a high intensity magnetic field is produced by the faulty poles. This in combination with the elevated temperatures, which narrows the hysteresis loop, can bring the magnetic field intensity inside the machine higher than the coercivity of the magnets, thereby demagnetizing them irreversibly and damaging the machine.

It is worth noting that a lot of factors can take the role of underlying cause for the turn-to-turn fault. As specified by [58], there is a wide variety of degradation mechanisms that will eventually lead to stator winding turn puncture. Firstly, extreme temperatures inside the motor caused by long time operation at higher than rated load or some kind of malfunction will stress the turn insulation, making it susceptible to puncture. Secondly, wear due to friction between the turn insulation of different stator pole coils induced by forces originating from the motor magnetic fields will erode the said spots of the insulation, facilitating the progression of the turn-to-turn fault, resulting in insulation failure.

Furthermore, thermomechanical insulation deterioration caused by rapid load changes resulting in insulation delamination as well as partial discharges due to aforementioned delamination, inadequate thickness of the insulation and/or manufacturing defects will degrade the insulation quality. Finally, contamination of the turn insulation due to humidity, oil, or chemicals will downgrade the insulation and lead to electrical tracking, which can lead to dielectric failure of the insulation system of the machine.

A wide range of analytical models regarding the turn-to-turn fault have been proposed in the academic literature in recent years. In [59] a general analytical model for the turn-to-turn fault in multiphase fault-tolerant permanent magnet machines was introduced and a novel T-type equivalent circuit was favoured. An elaborate fault model for motor coils connected in series or in parallel has been proposed by the authors in [60], while taking into consideration the potential flux coupling between the faulted coil and the other healthy coils in the same phase. In [61] a dynamic model of a PMSM in MATLAB/Simulink environment was presented with which the identification of the turn-to-turn short circuit fault at an early stage was demonstrated. Another analytical model was proposed in [62] this time based on winding functions and the physical geometry of the motor in question.Finally, in [63] a dynamic mathematical model for the turn-to-turn fault in surface mounted PMSM based on the motor's theoretical flux, current, and voltages combined with utilising the measurements of their positive and negative sequence components was submitted.

3 Chapter 3: Equivalent Circuit Modelling of Stator Poles

As discussed in previous sections of this thesis, permanent magnet machines have become exceedingly popular in modern applications due to their high power density and high efficiency. Throughout its lifespan, a permanent magnet machine receives a wide range of stresses such as thermal, electrical, ambient and mechanical, commonly known as TEAM. These stresses will gradually make the machine vulnerable to faults. These faults if not detected in time can evoke the breakdown of the machine. This makes reliable fault diagnosis methods and long term prognosis methods a topic of tremendous interest for both the academia and the electric motor industry.

Among the faults that afflict the PM machines, the turn-to-turn short circuit fault is one of the most prominent. The high current density required in the stator pole coils for that performance profile means that the looming danger of the fast progressing inter-turn fault is ever greater. This makes the continuous improvement of the insulation system in electrical machines a task of outmost significance, as its integrity and resilience throughout its lifespan is essential to the health and normal operation of the machine.

More specifically, in terms of prognosis, undetected manufacturing defects and tolerances in parts of electrical machines have long been an action point of stress mechanisms that will lead to an earlier than expected failure of the machine. To that end, a quality assessment procedure taking place, prior to the assembling process, is bound to significantly reduce the number of defective parts that end up in machines. So in other words, a finely tuned quality assessment procedure will lead to higher reliability and longevity of produced machines, meaning less maintenance procedures and costly repair downtimes.

The scope of our project was studying the behaviour of segmented stator poles and their mounted coil, Fig. 3.1, under multifactor ageing using offline tests such as impedance spectroscopy and Nyquist diagrams. At the early planning stages of the project, developing an equivalent circuit model of segmented poles with their mounted armature coils was deemed essential for the approximation of the healthy and aged states of the poles. The model with correct calibration based on experimental data would be able to configure the

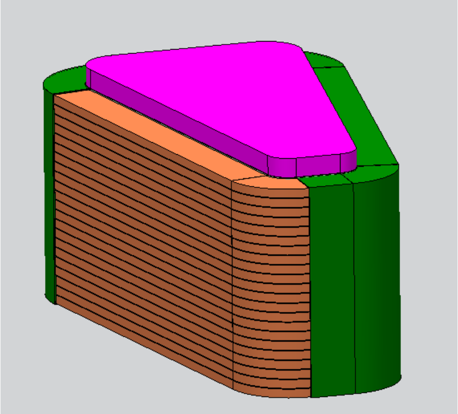

Figure 3.1: Segmented stator poles with mounted armature coil and its thin film insulation. With orange colour is depicted the copper wire, with green colour the PAI thin film insulation and with the pink colour the coil's core.

healthy state of the pole, providing us with its parameter values. The literature contains numerous models that attempt to describe coil behaviour across different frequencies [64] [65] [66] [67], but less effort has been dedicated to experimentally modelling the actual components with high complexity, a feature that is of outmost significance for making accurate predictions and accounting for real-world phenomena and manufacturing characteristics. Furthermore, some available past work around equivalent circuit modelling is designed for control or operation at specific frequencies only [68] [69], which does not fit with this project's scope. Equipped with the healthy pole model data, we would be able to monitor in what manner the multifactor ageing affected the pole's performance through impedance spectroscopy and Nyquist diagrams. For the impedance spectroscopy testing, the FRAX-99 Sweep Frequency Response Analyser manufactured by Megger was used and was configured to run for frequencies from 20 to 20 million Hz, Fig 3.2. For the rest of this master thesis, all figures or pictures that are presented below are results of my work and are owned by me unless explicitly mentioned.

3.1 Initial Circuit Choice and Parameter Assignment

The first step for the development of the equivalent circuit model was choosing a starting base circuit from where we would begin our task. The first design of the circuit is depicted in Fig. 3.3.

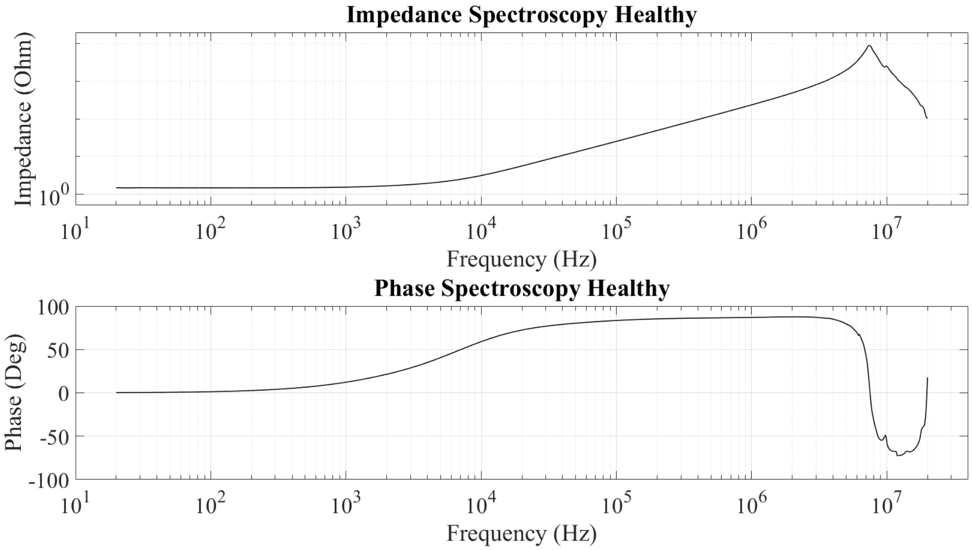

Figure 3.2: A typical spectroscopy measurement of a healthy pole test subject.

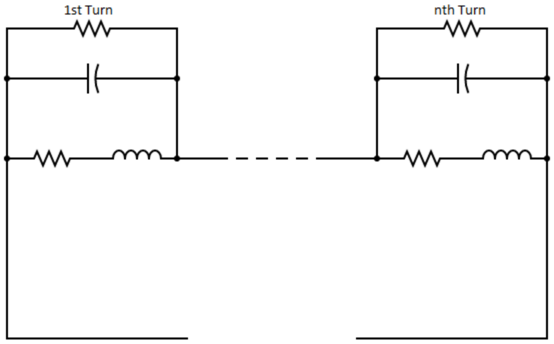

Figure 3.3: Initial Equivalent Circuit model of machine pole.

As it can be seen, this is an entirely intuitive and basic design. Each turn is composed of a series RL circuit connected in parallel with a parallel RC circuit [70]. The RC circuit describes the inductance and the resistance of a turn's copper wire, while the RL circuit describes the thin film insulation between turns. The components are connected in such a way so that when the turn resistance is theoretical punctured and a turn is shorted we can simulate the bypassed turn by reducing the resistance of the parallel RC circuit and allowing the current to flow through the insulation. The desired current flow of a shorted turn is shown in Fig. 3.4.

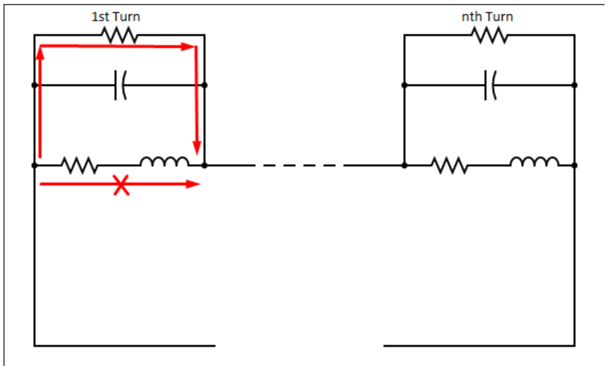

Figure 3.4: Current flow after a turn-to-turn short circuit.

3.1.1 Internal resistance of the armature coil

After designing this initial version of the model, we set out to measure the parameters of the healthy state of the pole for the calibration of its model. As it was said above, the resistance of the series RL circuit represents the resistance of the copper wire of each turn of the coil. The DC value of the resistance was measured using an ohmmeter and the value was found $R = 0.0041$ Ohm for each turn of the coil. However, the skin effect [71] is a phenomenon that has to be taken care of, as the spectroscopy frequency can reach the value of 20 million Hertz. So the resistance value needed to be calculated for every frequency step as shown in Fig. 3.5. The parameters of the formula being: l represents the length, σ the conductivity, ρ the resistivity, w the width, $t$the thickness, δ the skin effect depth being ($\delta = \frac{1}{\sqrt{\pi \cdot f \cdot \mu \cdot \sigma}}$) and the critical frequency of the skin effect being: $f_{se} = \frac{4}{\pi \cdot \mu \cdot \sigma}(\frac{w \cdot t}{w+t})^2$.

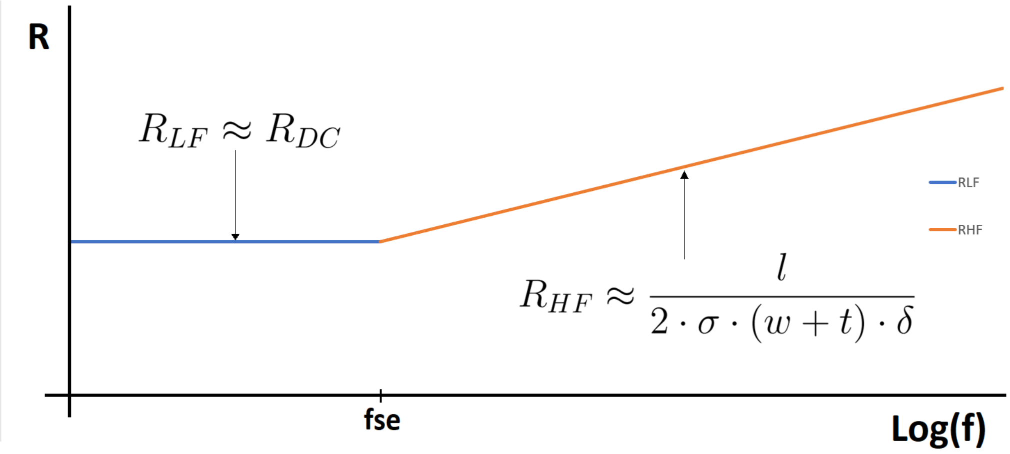

Figure 3.5: Behaviour of the internal resistance value with the skin effect present.

3.1.2 Inductance of each coil turn

The inductance of the series RL circuit models the inductance of each turn of the armature coil and it was measured through the impedance spectroscopy of the 95 healthy poles at our disposal. The inductance of each pole was drawn from the impedance value with the following method. For each of the 95 poles the frequency where the phase of the impedance was the closest to being 90°, in other words being close to fully inductive, was pinpointed and the corresponding total impedance was noted. Next, the inductance was calculated from the total impedance Z and the impedance phase θ at said frequency using the formula $L = \frac{|Z| \cdot sin\theta}{\omega}$. Finally, a mean value was drawn from the measurement population and through him the value $L = 37.9\mu H$ was calculated, which corresponds to the inductance of the whole coil. Consequently, for us to obtain the inductance of each turn we had to divide that value with the number of turns. Below, Table 3.1, the measured inductances organised in ranges are presented as well as the statistical analysis of the results, Fig. 3.6.

Limits (µH)	Number of Points
37.2-37.48	3
37.48-37.76	3
37.76-38.04	30
38.04-38.32	31
38.32-38.6	18
38.6-38.88	4
38.88-39.16	1
39.16-39.44	3
39.44-39.72	1
39.72-40	1

Table 3.1: Statistical Analysis of L measurements.

3.1.3 Turn-to-turn insulation resistance

The resistance of the parallel RC circuit represents the thin film insulation resistance between each turn of the coil. The desired values were measured using 10 copper wire bars, Fig. 3.7, coated with the same thin film insulation as the turns of the coil via the Megger MIT1525 15kV Insulation Tester. The test procedure was done as follows:

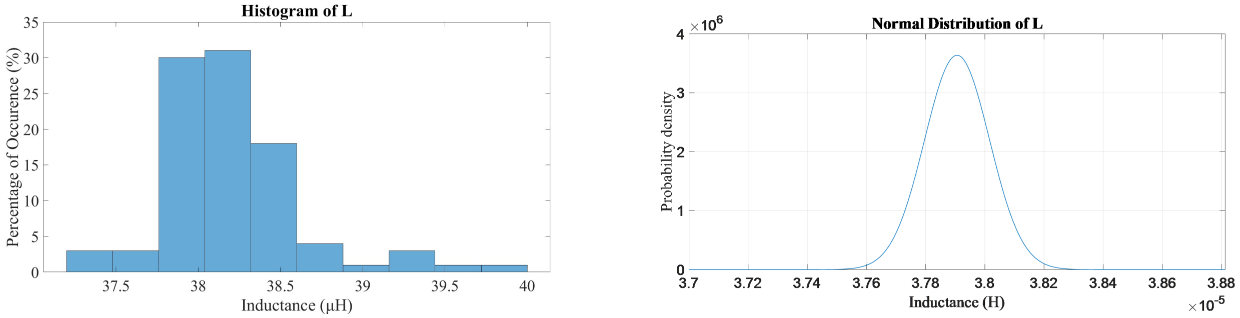

Figure 3.6: Histogram (left) and normal distribution (right) of the measured poles' inductance.

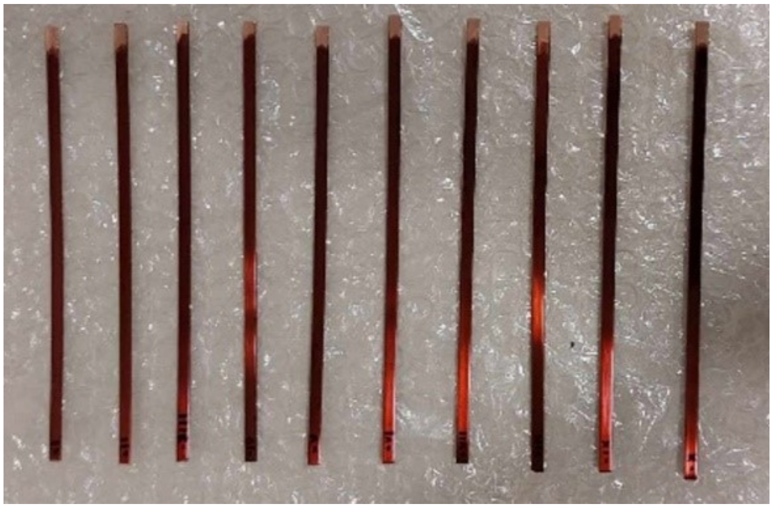

Figure 3.7: The 10 copper wire bar samples.

- The population of 10 copper wire bars were separated into 5 groups of 2.
- The ends of each bar were stripped of their insulation layer so that electrical contact between them and the megohmmeter is possible.
- Each group's bars were placed inside separate ducts within a custom-built plastic casing. The copper wire bars were then connected in parallel to each other via a copper plate and similarly copper plates were situated in contact with the thin film insulation of both bars, Fig. 3.8 (Left). The copper plates would act as the connection points to the megohmmeter, Fig. 3.8 (Right).
- With the megohmmeter set at 5 kV DC and timed for 8 minutes, the test would commence with the data being recorded on a computer with each group being tested at 3 different contact points for a good statistical result.

The copper wire bars were connected in parallel due to high resistance value restrictions, meaning that we had to take into consideration that the reading would correspond to half the resistance value of the thin film insulation. Worth noting is that the insulation resistance test was the last test to be conducted, as the high voltage applied to the insulation along its extended duration would have irreversibly and unpredictably stressed the insulation, making its parameters unfit for the healthy pole model. It is also important to note that when DC voltage is applied to the thin film insulation it will also act as a dielectric. So the absorption current of the capacitor will be measured together with the leakage current that we want to measure isolated with the megohmmeter. So the test duration of 8 minutes was selected as that is enough time for the absorption current of the capacitor to be small enough so that the leakage current, as per IEEE Std 43 standard [72], and in extension the resistance reading are as reliable as possible. The mean measurement of each group is presented below, Fig. 3.9, where we can see how the resistance value stabilizes along the IR test duration. The mean resistance value of each measurement was produced from the last one and a half minutes of its duration. From those values, the mean value between them was deemed the value of the thin film insulation resistance.

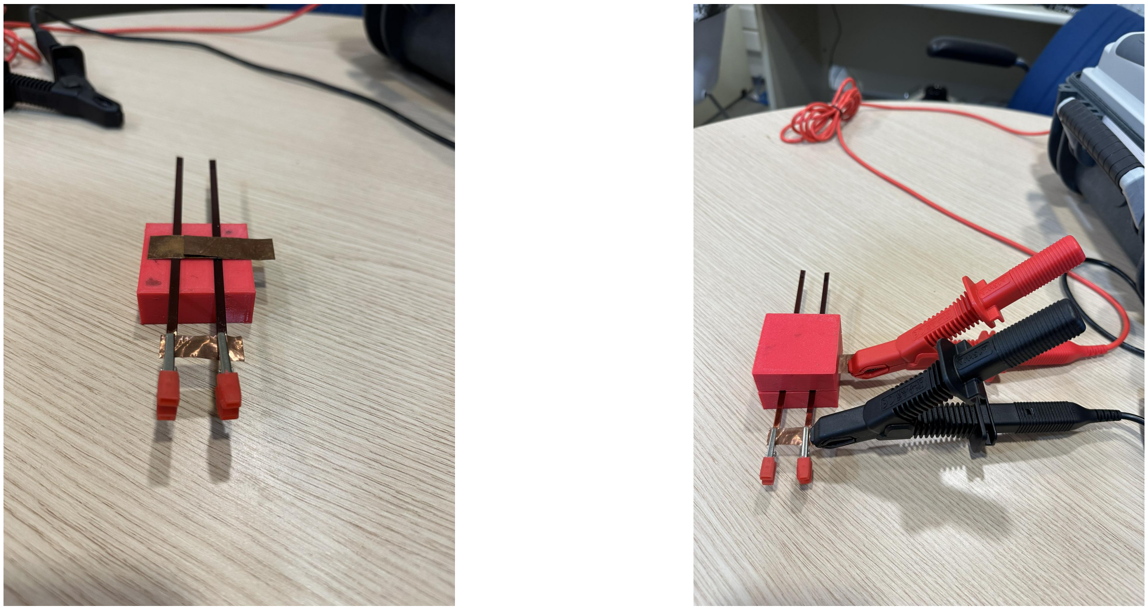

Figure 3.8: Thin film insulation resistance measurement.

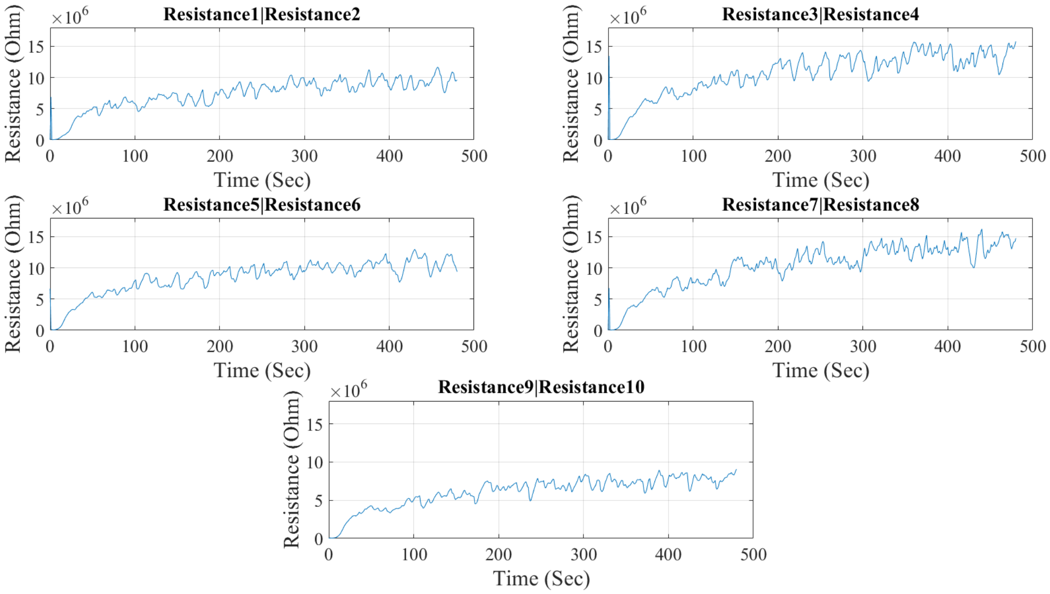

Figure 3.9: Mean measurement for each group as depicted by Megger MIT1525.

3.1.4 Turn-to-turn insulation capacitance

The capacitance of the parallel RC circuit models the thin film insulation capacitance between each turn of the coil. The measurements were carried out using 10 copper wire bars, Fig. 3.8, coated with the same PAI thin film insulation as the turns of the coil via the impedance spectroscopy test. The test was conducted as follows:

- The population of 10 copper wire bars were again separated into the same 5 groups of 2.
- The ends of each bar were stripped of their insulation layer so that electrical contact between them and the FRA tool is possible.
- Each group's bars were placed inside separate ducts within the custom-built plastic casing, with each bar positioned perpendicularly to the other creating a contact area where they meet, as seen in Fig. 3.10.
- Impedance spectroscopy was performed for each group at 16 different points of contact (80 measurements in total).

To measure the capacitance value, a similar procedure as the one used for the measurement of the inductance of each turn was conducted. A frequency where the

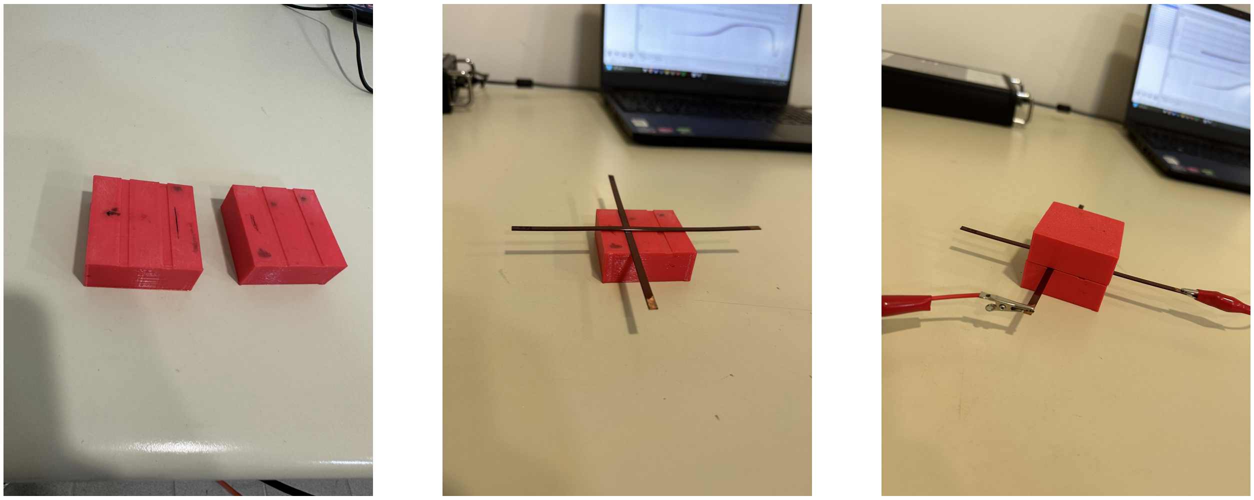

Figure 3.10: Thin film insulation capacitance measurement.

impedance phase was approximately -90°, almost fully capacitive, was needed. To that end, the 80 kHz frequency was selected and the impedance value of each measurement at said frequency measured was using the formula $C = \frac{1}{\omega \cdot |X_c|}$, giving us 80 capacitance values. Below, Table 3.2, the statistical analysis of the results as well as the measured capacitances organised in ranges and corresponding normal distribution are presented, Fig. 3.11.

Limits (pF)	Number of Points
4.1-4.29	2
4.29-4.48	3
4.48-4.67	8
4.67-4.86	9
4.86-5.05	11
5.05-5.24	11
5.24-5.43	9
5.43-5.62	7
5.62-5.81	6
35.81-6.0	9
6.0-6.19	4

Table 3.2: Statistical Analysis of C measurements.

It is important to note that the capacitance value calculated does not correspond to the thin film insulation capacitance of each turn. To find the desired value at first the measured value was normalized based on the surface of the contact point between the copper wire bars. Then the surface of each turn was calculated using the length as well as the width of a single coil turn. Finally, the normalized capacitance value multiplied with the turn surface give us

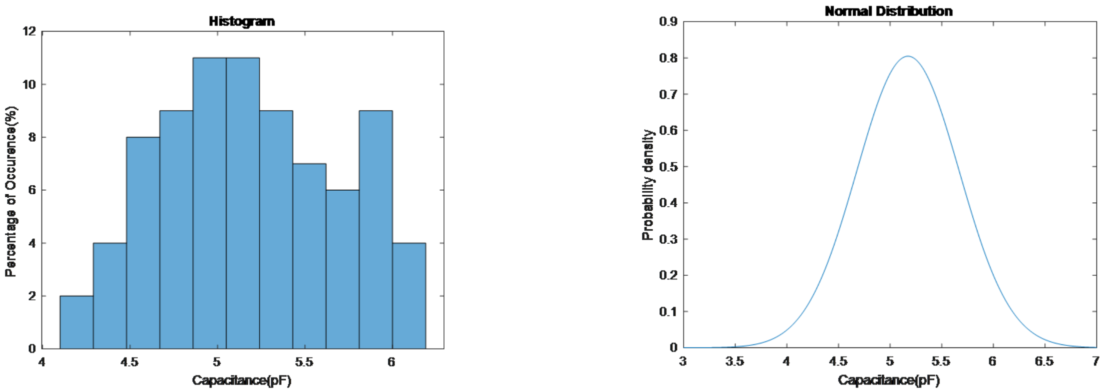

Figure 3.11: Histogram (left) and normal distribution (right) of the measured thin film insulation capacitance.

the value of the capacitance of each turn, with said value being introduced in the model.

3.1.5 Impedance and phase spectroscopy comparison to experimental results

Below, Fig. 3.12, the comparison between the impedance spectroscopy simulation results of the model and the experimental results of the impedance spectroscopy test of a healthy pole are plotted. As we can, there is some resemblance between the two graphs but this not an acceptable result. More specifically, during the low frequencies of the test the experimental graph starts at a higher value and maintains said value for a while, a phenomenon not present in the model graph. During the medium frequencies of the test, there is good resemblance between the two graphs with both increasing at an equal rate. Finally at the higher frequencies, the antiresonance points of the two graphs do not fit meaning that the inductive impedance of the copper wire becomes equal to the capacitive impedance of the thin film insulation later than intended.

As far as the phase graph comparison is concerned, Fig. 3.13, it is evident that in the experimental measurement the impedance acquiring an inductive behaviour, as the frequency increases, is a more gradual process compared to the model phase graph where 90°are reached at the 1kHz mark. That phenomenon can be explained as the impedance of the pole model acquiring an inductive behaviour much faster than the real pole. Finally, at the last frequency values of the procedure we can see the phase value acquiring positive values again while the model fails to do so.

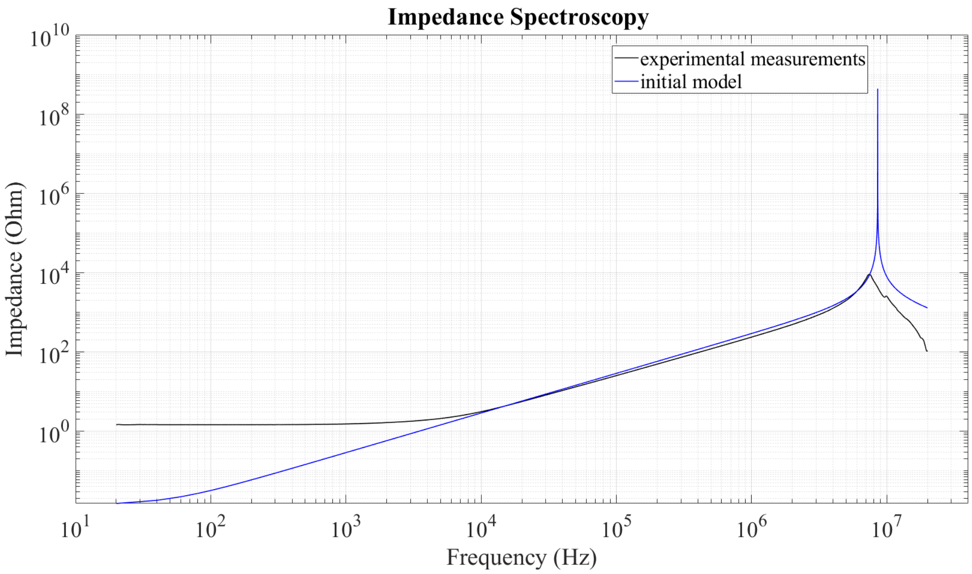

Figure 3.12: Impedance spectroscopy comparison between developed initial model FRA simulation and experimental results.

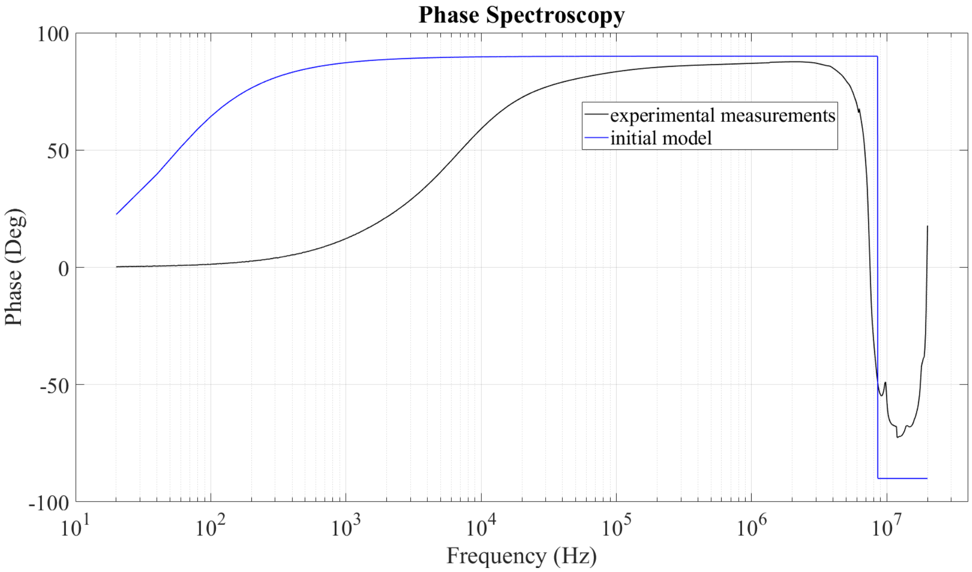

Figure 3.13: Phase spectroscopy comparison between developed initial model FRA simulation and experimental results.

To conclude, the above comparison of the impedance and phase graphs between the model simulated measurements and the experimental measurements tell us that the equivalent circuit model of the healthy pole is a subject for revision. Changes have to be made so that the remarks mentioned can be fulfilled through the equivalent circuit, so that it can more accurately simulate the experimental measurements.

3.2 Advanced model version and discussion

Firstly, for our model to better represent the coils properties we decided to introduce a new set of extra parameters. The more detailed instance of the equivalent circuit is shown below, Fig. 3.14.

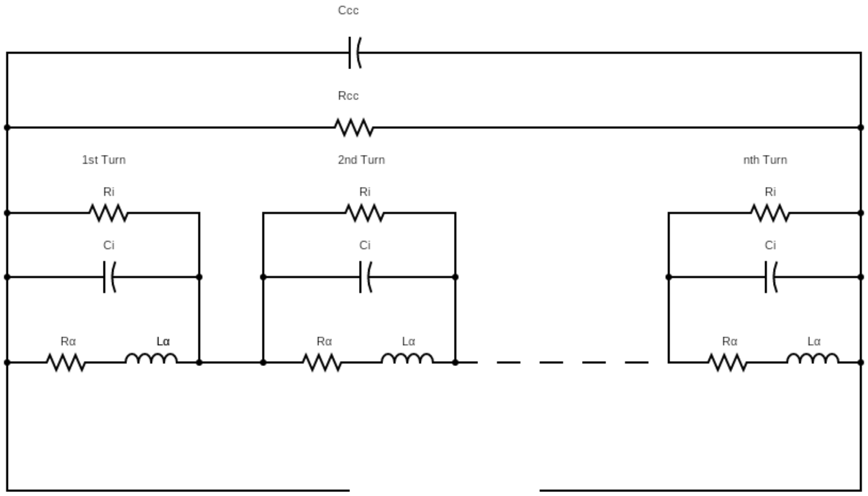

Figure 3.14: The more detailed version of the equivalent circuit model.

This new version of the equivalent circuit is designed to be able to take into account the possibility of a coil-to-core short circuit fault. To achieve that, we decided configuring the coil-to-core insulation parameters similarly to the thin film turn insulation using a parallel RC circuit that connects the two end windings of the armature coil. To measure the values of the aforementioned parameters, new procedures and equipment designs needed to be devised. Additionally, with introduction of more parameters we decided naming the model parameters with the names shown below, Table 3.3.

Name	**Description**
R_α	Internal turn resistance.
L_α	Single turn inductance
C_i	Capacitance between two turns of the coil.
R_i	Insulation resistance between two turns of the coil.
R_{cc}	Resistance between the core and coil.
C_{cc}	Capacitance between the core and coil.

Table 3.3: Equivalent circuit parameter index.

3.2.1 Resistance between the core and coil R_{cc}

Our first concern was the measurement method of the value of the R_{cc} parameter. For that reason, a custom plastic case with a pole-shaped conductive floor made out of solder was designed and built. It would accommodate the poles while providing a conductive point of contact during the measuring procedure, Fig 3.15, that was carried out as follows:

- The whole population of poles, 95 in number, would be used for a good statistical result.
- The poles would be placed inside the case so that the pole core would make direct contact with the conductive floor of the case.
- Next, one the electrodes of the megohmmeter would be connected to the pole-shaped conductive floor of the case while the other to one of the terminals of the pole, Fig. 3.16.
- With the megohmmeter set at 5 kV DC and timed for 12 minutes, the test would commence with the data being recorded on a computer.

Figure 3.15: Custom pastic casing with conductive floor. As it can be seen a metal wire is protruding from the conductive floor to make the connection with the testing equipement possible.

Figure 3.16: R_{cc} measurement procedure.

The duration of 12 minutes was chosen so that capacitor absorption current would not influence our measurement. The mean value of each measurement was produced from the last 2 minutes of its duration and the average value between those values gave us the value of $R_{cc} = 2.28$ TΩ. It is important to note that this test was conducted after the measurement of the coil-to-core capacitance as the high voltage and long duration of the measurement would have aged electrically the insulation. Below are presented the stem plot of the mean resistance values of each pole, Fig. 3.17, as well as the corresponding histogram, Fig. 3.18.

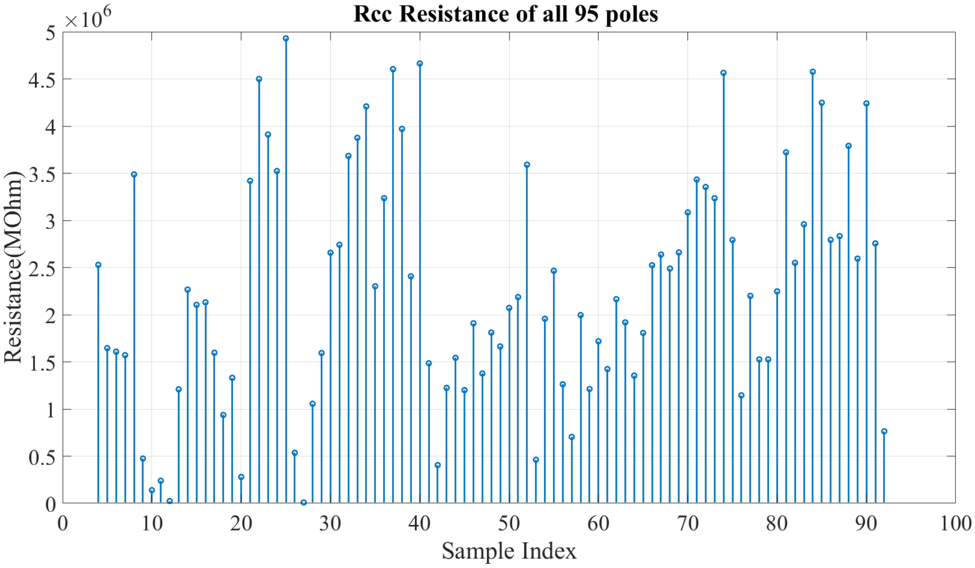

Figure 3.17: Stem plot of the mean resistance values of each pole.

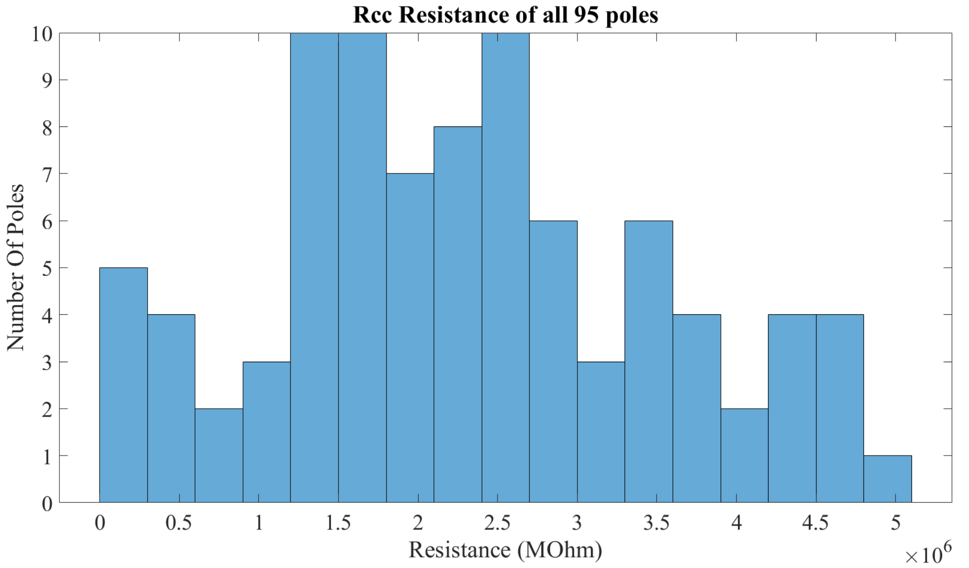

Figure 3.18: Histogram of the mean resistance values of each pole.

3.2.2 Capacitance between the core and coil C_{cc}

For the measurement of the coil-to-core capacitance the procedure devised was as follows:

- The whole population of poles, 95 in number, would be used for a good statistical result.
- The procedure started with bringing the pole core and a copper plate in the best

conducting contact possible. Good contact between them would be essential to the elimination of parasitic elements that would reduce the quality of the measurement.

- After bringing the copper plate and the core were in contact connection to the Frequency response Analyzer would be established, with one of the electrodes being connected to the pole core through the copper plate and the other electrode being connected to one of the coil's terminals.
- The impedance spectroscopy test would run and produce the corresponding graph, Fig. 3.19 and Fig. 3.20.

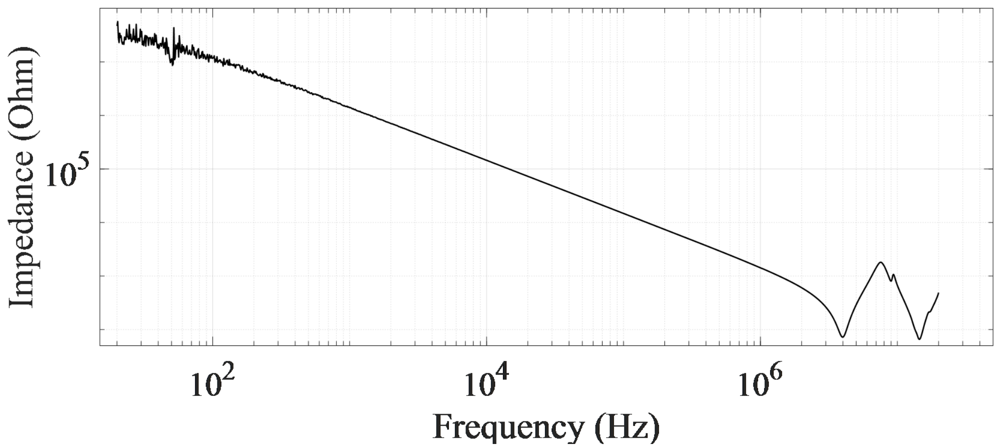

Figure 3.19: Typical impedance spectroscopy of the insulation between the coil and the core.

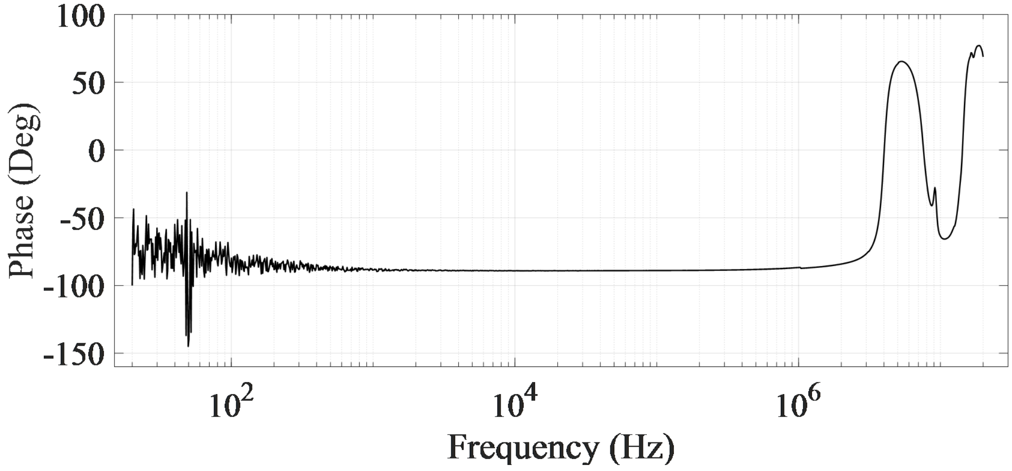

Figure 3.20: Typical impedance phase spectroscopy of the insulation between the coil and the core. The capacitive nature of the core-to-coil impedance is confirmed from the phase value staying at -90 °for most of the duration of the test, verifying our parallel RC circuit choice for the representation of the core-to-coil impedance.

To measure the capacitance value, the same procedure as the one used for the measurement of the thin film insulation capacitance was incorporated. The impedance value at a frequency where the impedance phase was approximately -90°was used to extract the core-to-coil capacitance of each pole using the formula $C_{cc} = \frac{1}{\omega \cdot |X_c|}$. Finally the mean out of the 95 capacitance values was calculated to be $C_{cc} = 103.06$ pF. It is worth noting that that is the value that represents the core-to-coil capacitance as potential difference existed between the whole coil and the whole core, so the capacitor created was one that exists even during rated operation. Below, Table 3.4, the statistical analysis of the results as well as the measured capacitances organised in ranges and corresponding normal distribution are presented, Fig. 3.20.

Limits (pF)	Number of Points
10-28	3
28-46	0
46-64	0
64-82	4
82-100	14
100-118	32
118-136	19
136-154	17
154-172	3

Table 3.4: Statistical Analysis of C_{cc} measurements.

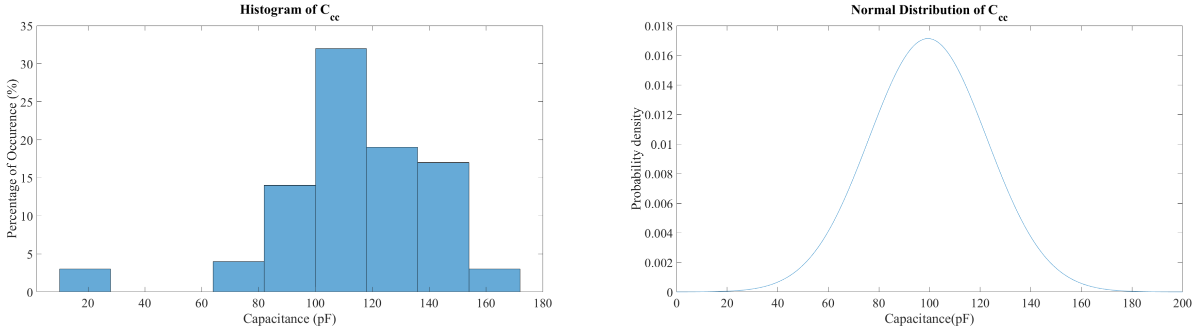

Figure 3.21: Histogram (left) and normal distribution (right) of the measured core-to-coil capacitance.

3.2.3 Impedance and phase spectroscopy comparison with previous model and experimental results.

Below, Fig 3.21, the three-way impedance spectroscopy comparison of the advanced model, the initial model and the experimental is plotted. Firstly, we can see that the advanced model reaches its antiresonance point faster than the previous initial model. This is an expected result as the additional capacitance will increase the rate at which the capacitive impedance decreases as the frequency increases, meaning that the inductive impedance would become equal to the capacitive impedance at an earlier frequency value. However, despite this being a more detailed representation of the pole's equivalent circuit we can see that the impedance spectroscopy graph as well as the impedance phase graph diverge more from the experimental results than the initial model.

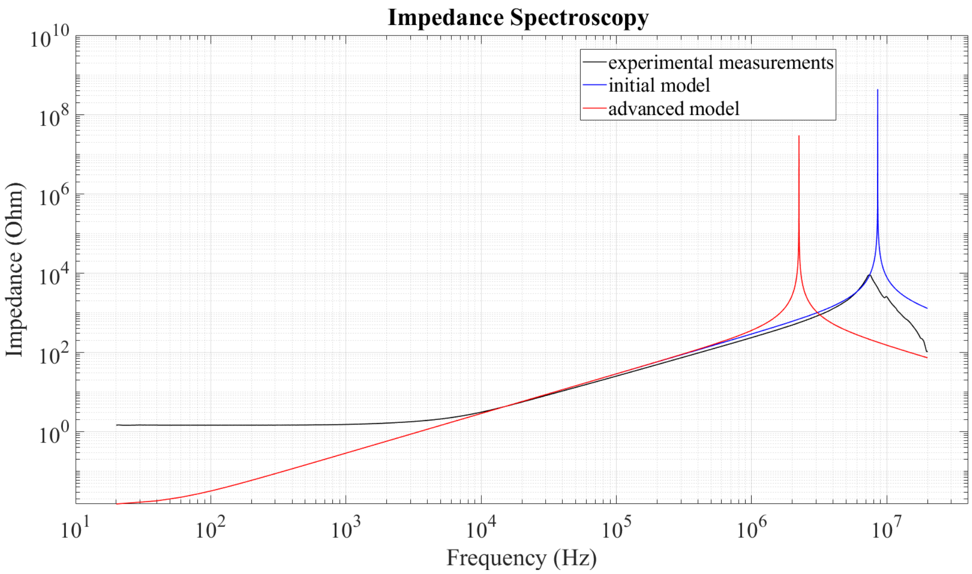

Figure 3.22: Impedance spectroscopy comparison.

To conclude, in this model version all the highlighted issues (section 3.1.5) about the initial model remain unsolved. The above observations are a strong indication that more model parameters are needed for the astute description of the pole.

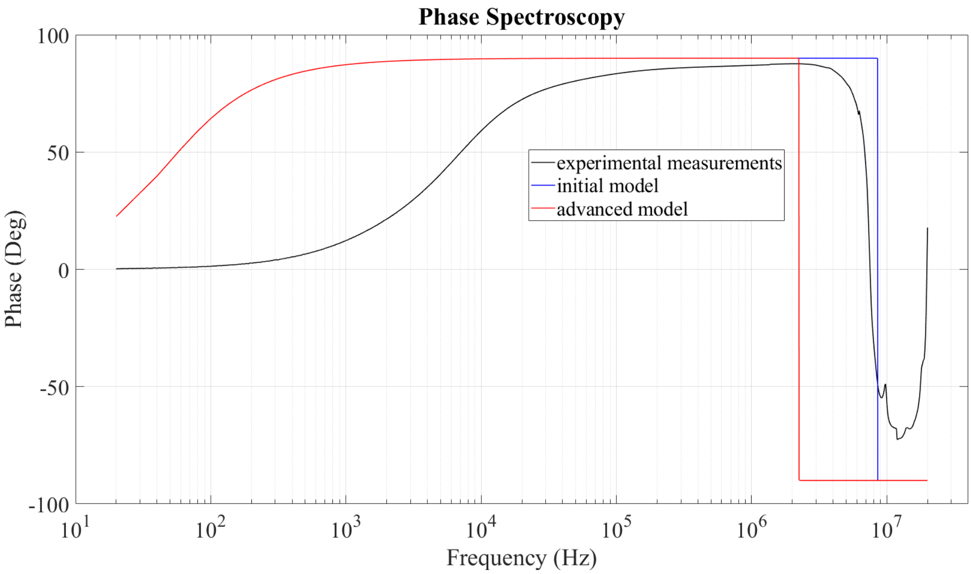

Figure 3.23: Phase spectroscopy comparison.

3.3 Equipment-tied circuit parameters and final calibration

After constructing the advanced equivalent circuit we opted to exploring factors capable of influencing the impedance spectroscopy test results but not associated with the test subject. Consequently, we set out to investigate how the wiring and the test equipment itself could be represented inside the equivalent circuit model.

3.3.1 Resistance of the wiring

The existence of a resistance connected in series to the pole's equivalent model was indicated to us by comparing the model's impedance and phase spectroscopy with the experimental results. As noted previously, in low frequencies there is a noteworthy difference in impedances between experimental measurement and model simulation, which was calculated to be 1.37 Ohm. Moreover, the impedance sustains that value for an extended period before any noticeable change occurs. For us to interpret this behaviour of the impedance, we assumed this being the effect of a resistance connected in series to the model's equivalent circuit, as that would increase the circuit's resistance at low frequencies and impede the circuit from acquiring an inductive behaviour due to the coil.

So this phenomenon was attributed to the wiring that connected the frequency response analyzer and the test subject. To find the value for said resistance, we simply connected the two ends of the wiring with each other and used an ohmmeter. As seen in Fig. 3.24, the cable resistance is found 1.2 Ohm which is quite close to 1.37 Ohm, with the 0.17 Ohm difference being attributable to the inner resistance of the FRA tool. Thus, the aforementioned assertion about the cable resistance was verified. After the convincing results, the resistance of the wiring was named R_{add1} and inserted to the equivalent circuit model as shown below, Fig. 3.25

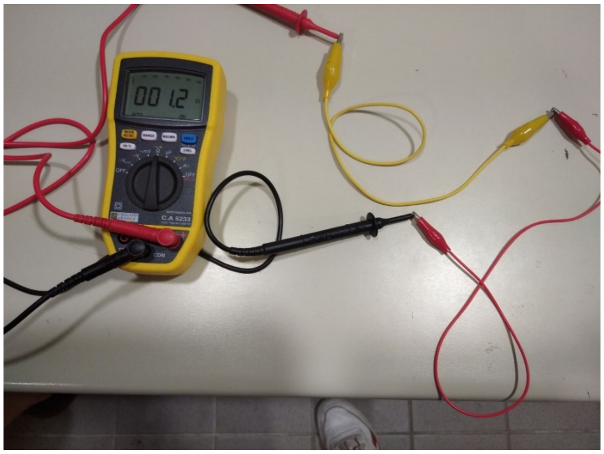

Figure 3.24: Resistance measurement of the wiring.

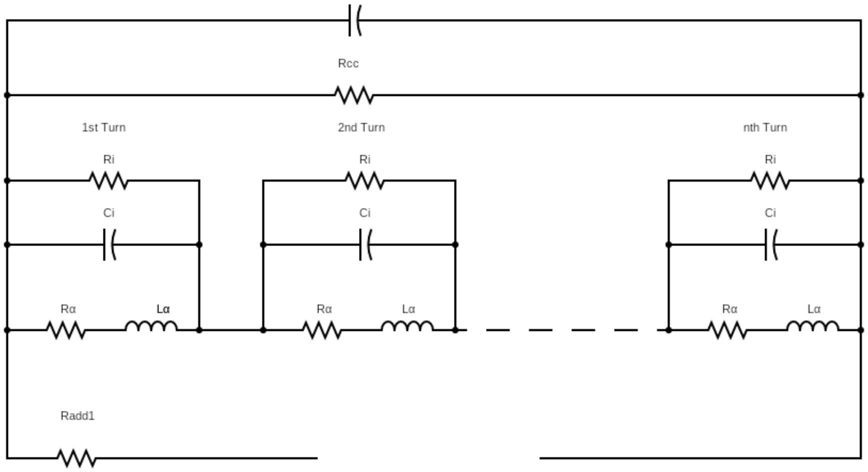

Figure 3.25: Equivalent circuit with the addition of R_{add1}.

The effect of the new parameter on the impedance spectroscopy, Fig. 3.26, and phase spectroscopy, Fig. 3.27, graphs are shown below. It is evident that the addition of R_{add1} fixes any issues as far as low frequencies are concerned, further verifying our hypothesis.

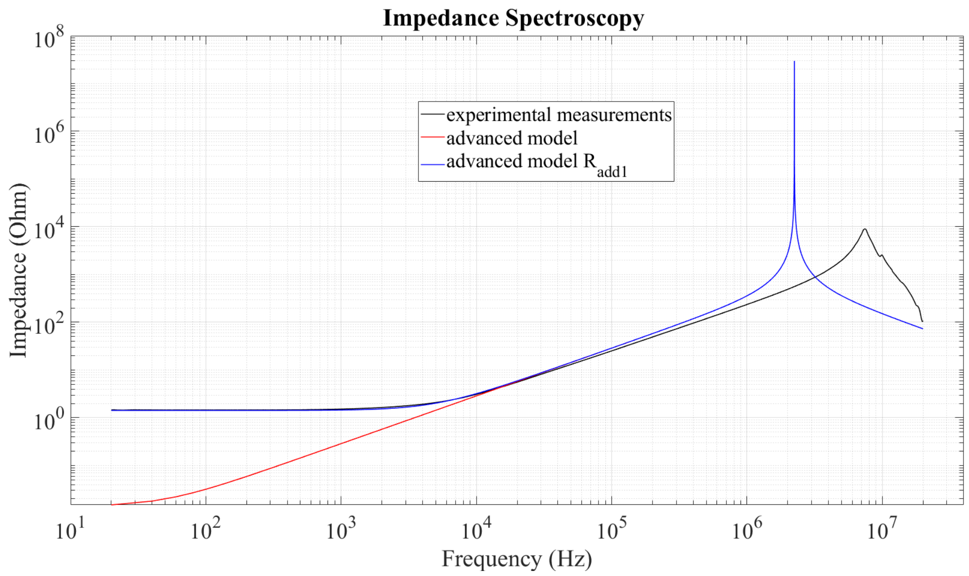

Figure 3.26: Impedance spectroscopy comparison.

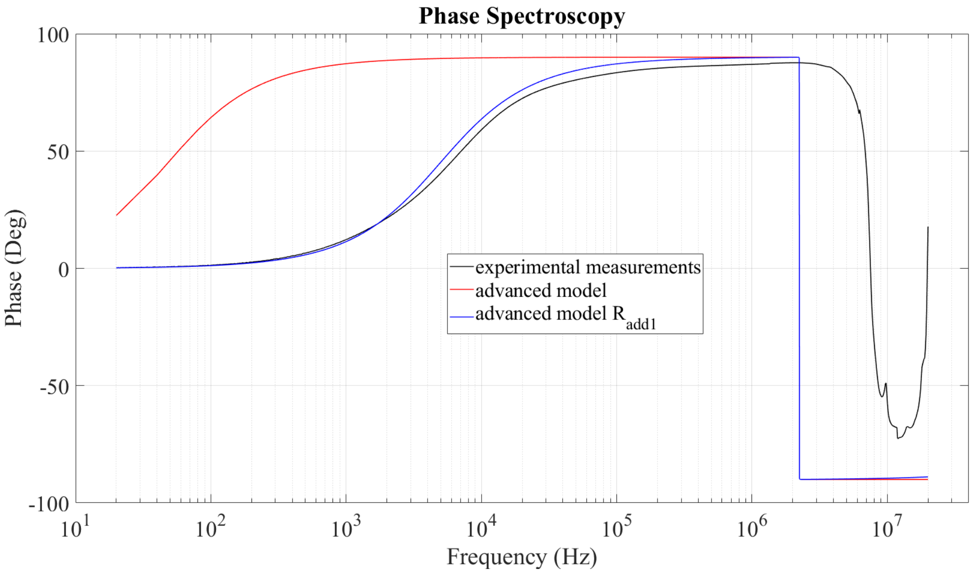

Figure 3.27: Phase spectroscopy comparison.

3.3.2 Inductance of the wiring

After introducing the R_{add1} parameter to the model, we started exploring in what other way could the wiring influence our test results. To have a better grip on what we were searching for we decided to run an impedance spectroscopy test with the two electrodes connected to each other. Below the corresponding impedance, Fig. 3.28, and phase graphs, Fig. 3.29, can be seen. Firstly, noticing the impedance having a value close to 1.37 Ohm for all the low frequencies of the test verifies further the value chosen for the resistance of the wiring . Then, from the middle point and onwards of the impedance graph of the short test we can see that the impedance increases at a logarithmic rate as the frequency increases. This phenomenon combined with the phase acquiring positive values makes it safe to assume the inductive behaviour of the impedance along those frequencies.

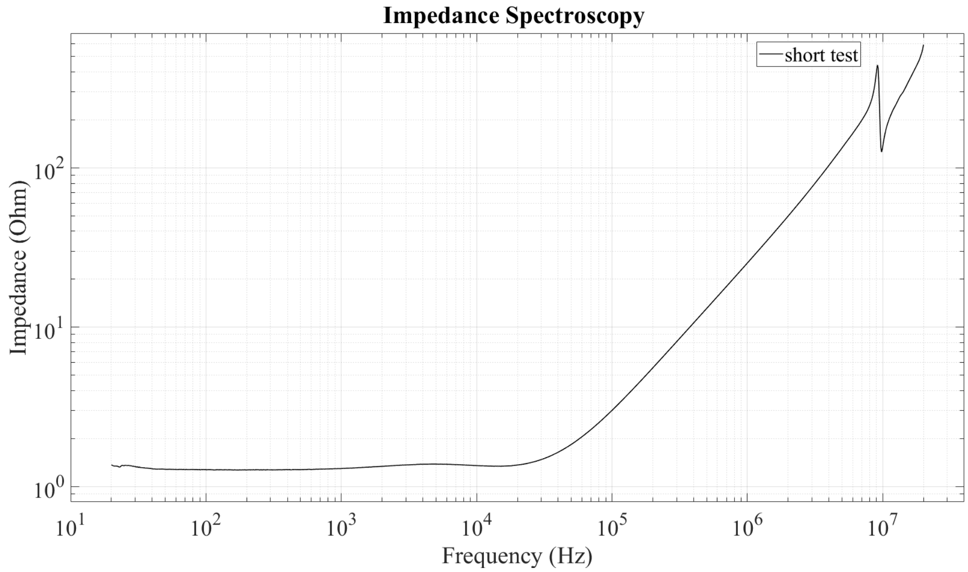

Figure 3.28: Impedance of the short test.

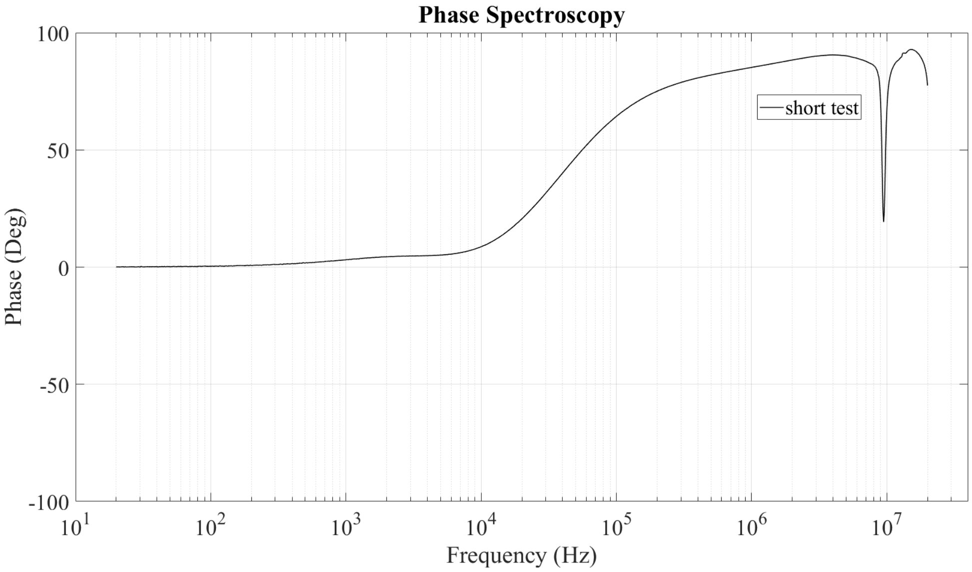

Figure 3.29: Phase of the short test.

After the above remarks, we decided that an inductance connected in series with R_{add1} is the correct way to represent this inductance. The value for said inductance would be extracted from the impedance graph at a frequency where the phase acquires a value that is closest to 90°by subtracting the real part of the AC resistance with skin effect included and calculating the inductance from the purely inductive impedance $L = \frac{X_L}{\omega}$. The frequency chosen was 3 MHz and the inductance was calculated to be $L_{series} = 4.09$ mH. Below, the new equivalent circuit model is shown, Fig. 3.30.

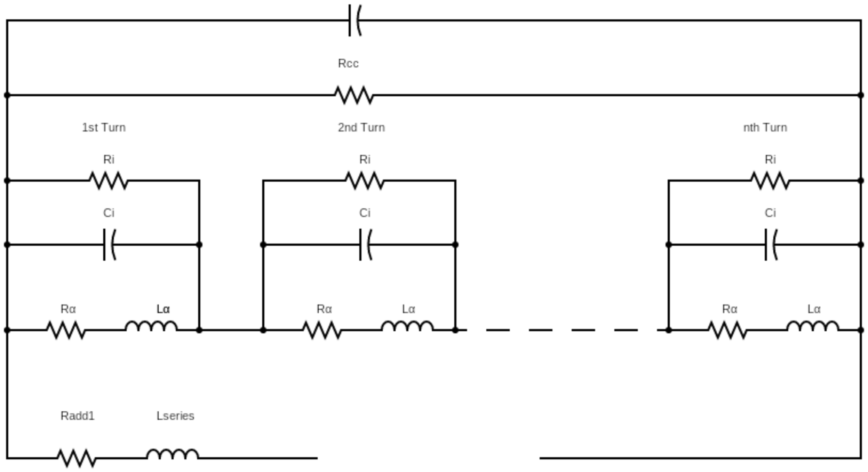

Figure 3.30: Equivalent circuit with the addidtion of L_{series}

The effect of the new parameter on the impedance spectroscopy, Fig. 3.31, and phase spectroscopy, Fig. 3.32, graphs are shown below. From the impedance spectroscopy graph, the main difference between before and after the introduction of the L_{series} parameter in our model is that there is a resonance occurring after the first one. Additionally, this resonance point signals the impedance transitioning from a capacitive behaviour to an inductive one as the impedance starts increasing logarithmically with respect to frequency. Moreover, the phase graph further verifies our deduction as the phase can be seen changing value from -90°to 90°. Modelling this phenomenon was of utmost significance as it can also be seen taking place during the experimental measurements.

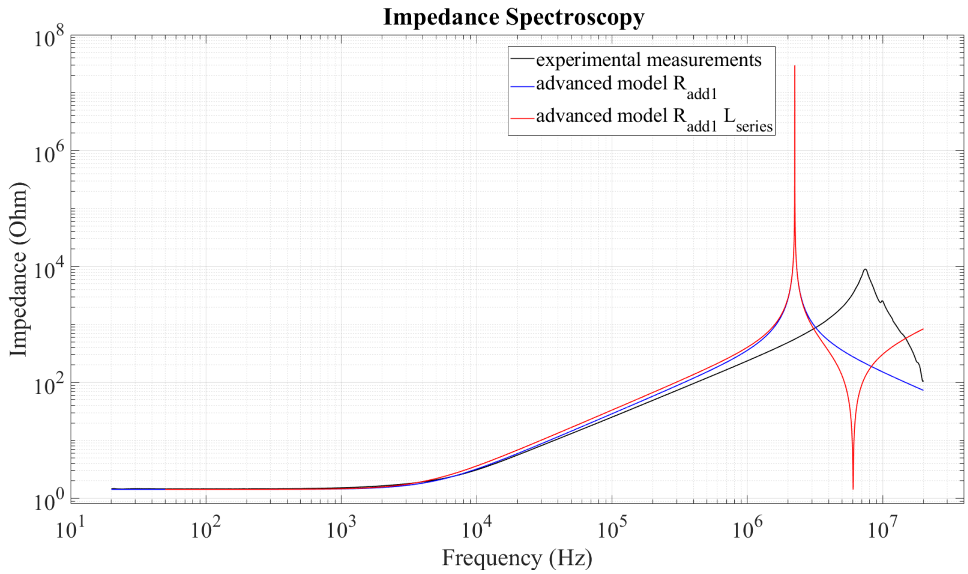

Figure 3.31: Impedance spectroscopy with the addidtion of L_{series}

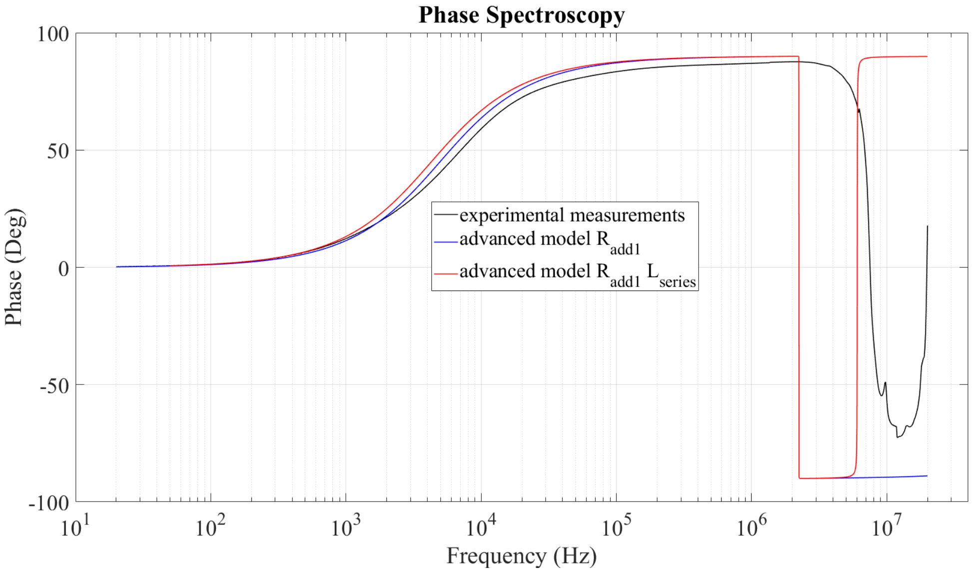

Figure 3.32: Phase spectroscopy with the addidtion of L_{series}

3.3.3 Final calibration and end effects.

In this section, the influence that the FRAX 99 has upon the impedance spectroscopy graph will be explored and how high frequencies affect the equivalent circuit modelling will be discussed. The end effects of the coil will also be discussed and how they were modelled in the equivalent circuit. Finally, the final comparison of the graphs between the final model and the experimental measurements will be showcased.

As it was showcased previously, factors not tied to the test subject can have a large influence upon the spectroscopy test results, as we have seen with the connection wiring. With that in mind, the started exploring how the test equipment could influence the spectroscopy graphs. Below, Fig. 3.33, the FRAX-99 inner measurement circuits are showcased as they are depicted in the user manual provided by Megger.

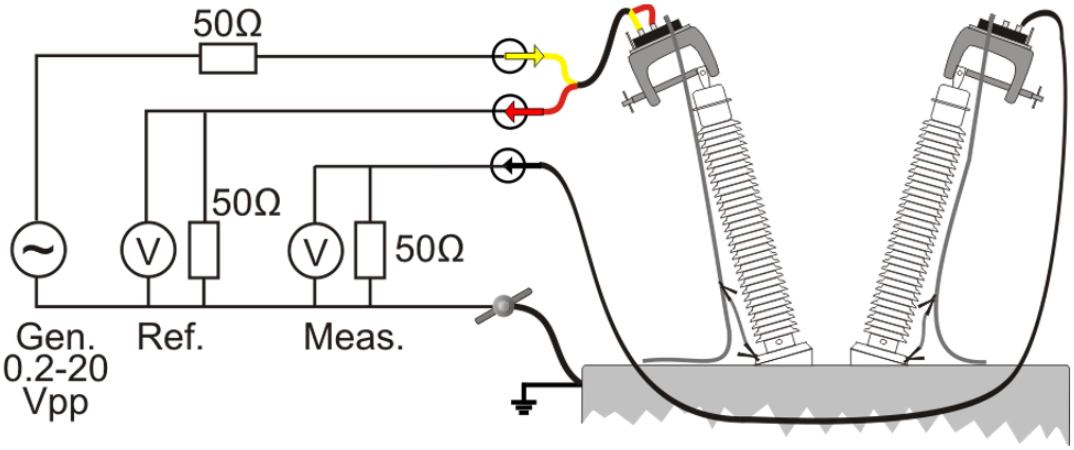

Figure 3.33: FRA-99 measurement circuitry, as depicted in the user manual provided by Megger.

As illustrated, the measurement and reference voltmeters are each connected in parallel to one 50 Ohm SMD resistor. Those two resistors are connected in series with respect to the ground cable, and their combination is connected in parallel to the coil while performing spectroscopy. However, they are affected by some level of skin effect at high frequencies, increasing their resistance values. This increase results in a reduction in the resistance R_{cc} connected in parallel to the coil turns. Additionally, during the spectroscopy test, a resistance was connected between the C-shaped test clamps, in parallel to the test circuit, for circuit protection reasons. We model the change in resistance value caused by the above effects by adding a resistor named R_{add2} in parallel to R_{cc} in the equivalent circuit. Below, we can see the spectroscopy graphs before and after the addition of R_{add2}.

It is evident that the addition of R_{add2} reduces the peak value that the impedance attains during the spectroscopy test while not changing the frequency where said peak takes place. We can also see greater resemblance between the model and the experimental measurements after the addition of the R_{add2} parameter, which signals a step towards the right direction concerning the accuracy of our model.

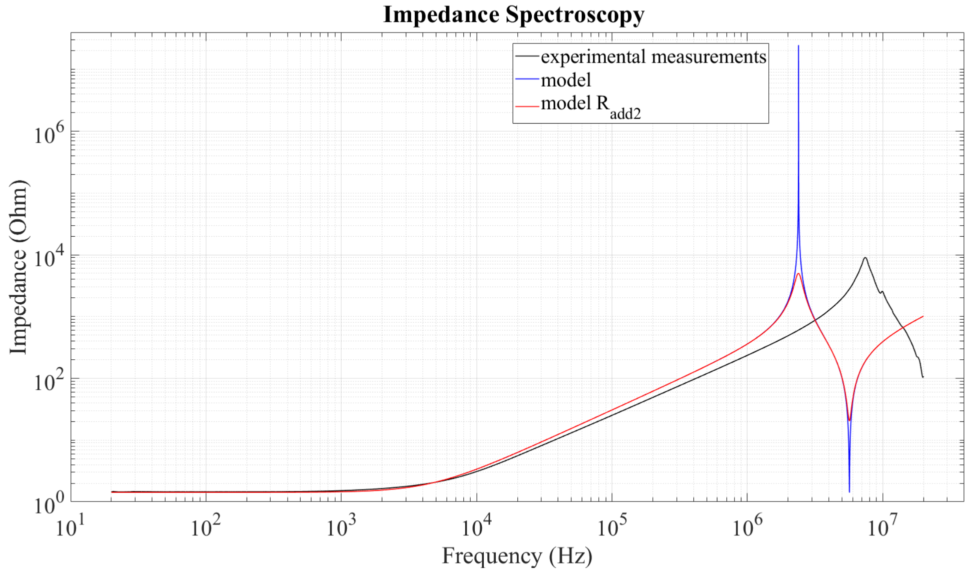

Figure 3.34: Impedance spectroscopy with the addition of R_{add2}

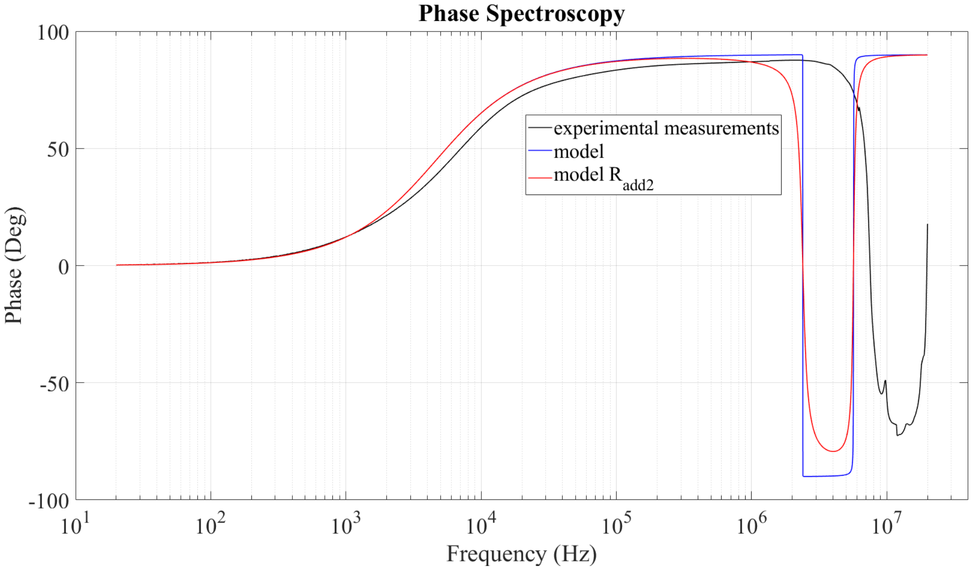

Figure 3.35: Phase spectroscopy with the addition of R_{add2}

In this paragraph, we will discuss how high frequencies dynamically affect the equivalent circuit modelling. As the frequency increases during the spectroscopy, the impedance of the coil-to-core circuit will start to reduce until the resonance happens. There, the capacitive impedance of the coil-to-core circuit becomes equal to the inductive impedance of the wiring making the imaginary part of the transfer function zero. For frequencies after the resonance, the impedance becomes an increasing function with respect to frequency. However, as it is illustrated in Fig. 3.36 and Fig 3.37, at higher frequencies we can see again the impedance acquire a capacitive behaviour once again after an antiresonance point.

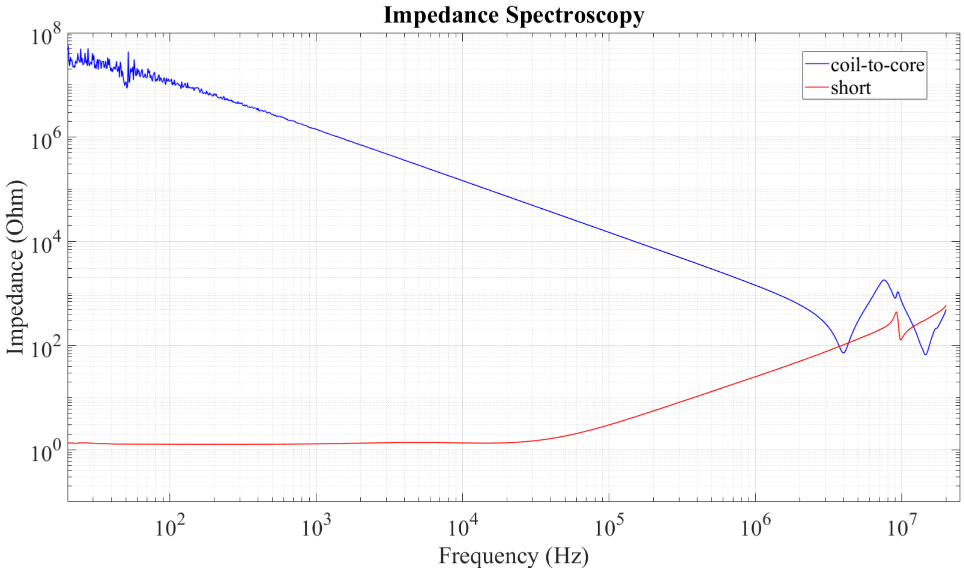

Figure 3.36: Impedance spectroscopy comparisson between the coil-to-core and short measurements

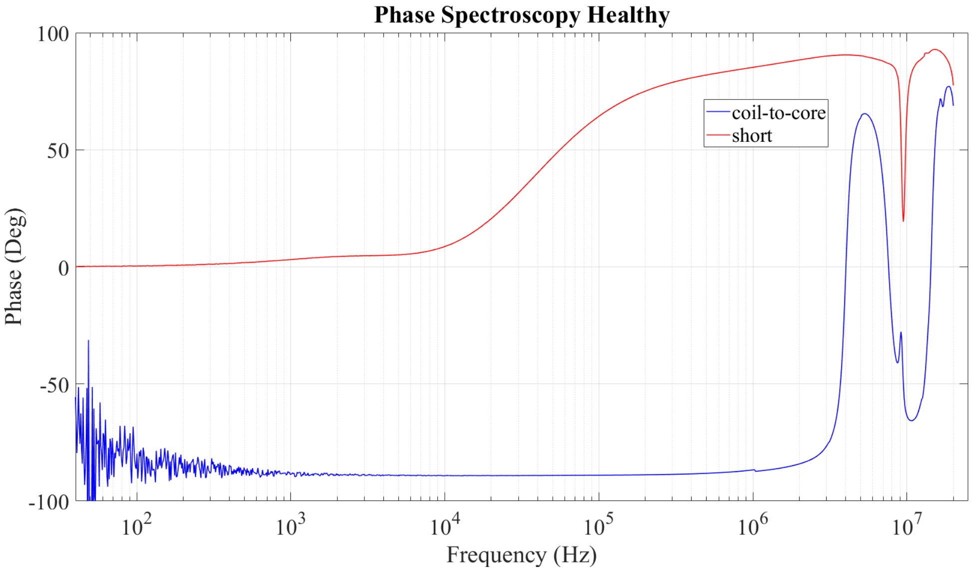

Figure 3.37: Phase spectroscopy comparisson between the coil-to-core and short measurements

This indicates the coil-to-core capacitor to have a lower capacitance value than expected at higher frequencies. This could possibly be the result of coupling between the coil and the core of the pole due to the weakening of the impedance between them and thus the coil-to-core impedance being represented only by its weakest points, reducing the capacitor surface and by extend the capacitance value. If we use the capacitance value after the coupling occurs C_{cg}, we get the following impedance and phase spectroscopies, Fig. 3.38 and Fig 3.39. The clear resemblance between the graphs of the experimental measurements and the model verify that the coil-to-core capacitance does decrease at higher frequencies.

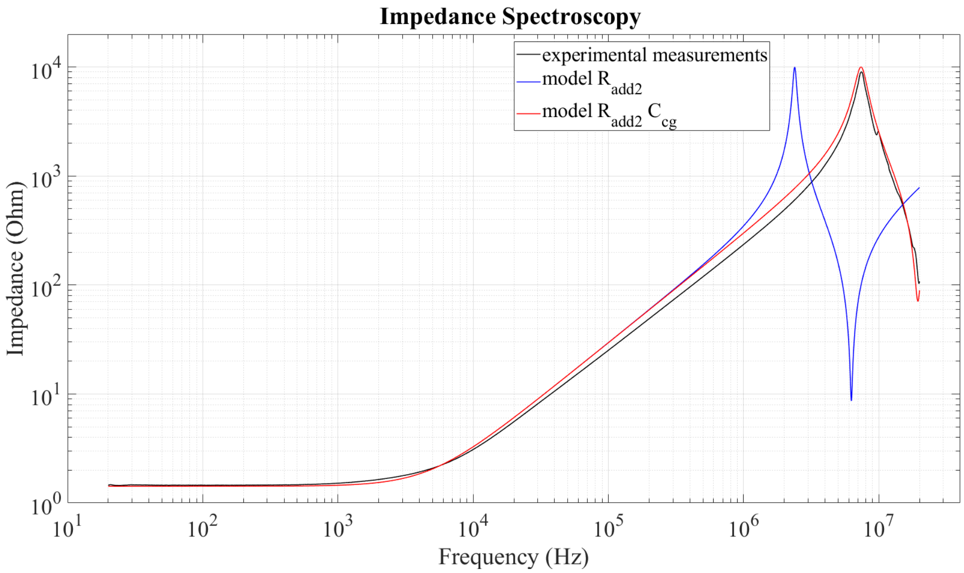

Figure 3.38: Impedance spectroscopy with the addition of C_{cg}

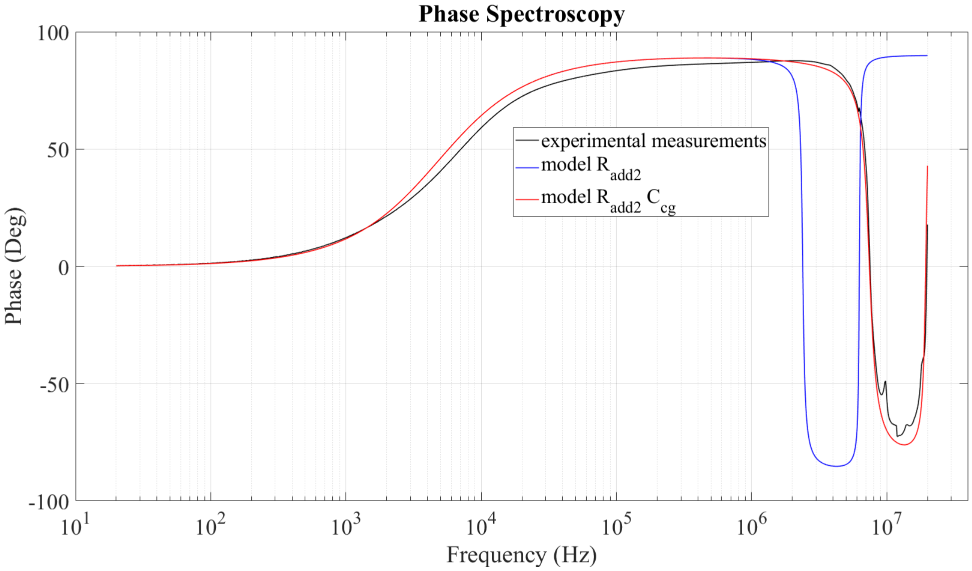

Figure 3.39: Phase spectroscopy with the addition of C_{cg}

Afterwards, we decided to deal with the more detailed matching of our model to the experimental measurements. This caused us to investigate a phenomenon that we noticed on the impedance spectroscopy graph of the experimental measurements. As we can see below, Fig. 3.37, a fluctuation can be spotted in the impedance spectroscopy graph close to the main antiresonance, something not present on our model impedance spectroscopy.

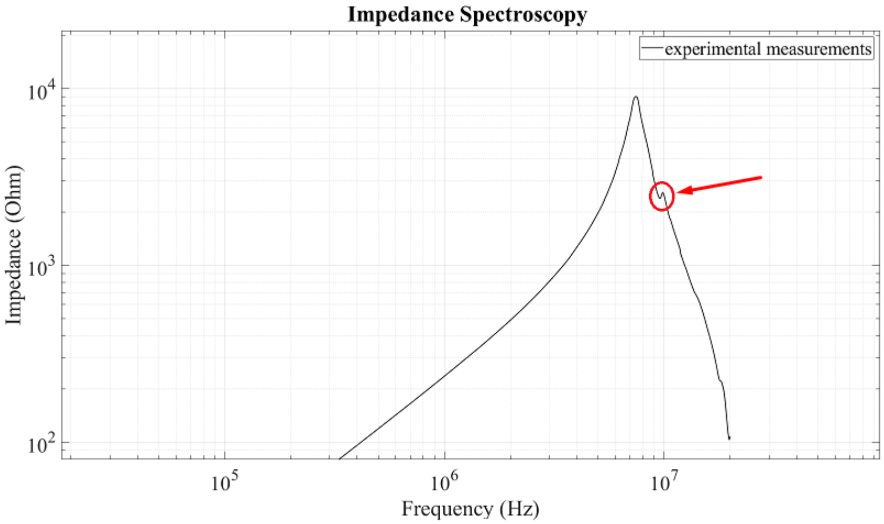

Figure 3.40: Fluctuation in the impedance spectroscopy graph.

After some experimentation with the model it was discovered that the phenomenon is due to the first and last turns of the coil having different parameter values due to the end windings. To configure the model to take into consideration the end effects, we reduced some parameter values of the first and last turns of the coil. The reasoning behind our thought process was that the end windings are not form complete turns, so their L_α and R_i must be less compared to the other coil turns. Using the magnitude of the fluctuation and the frequency where it was present we calculated the L_{end} and R_{end} values compared to the original values as:

$$\begin{aligned} L_{end} &= 0.8 \cdot L_a \\ R_{end} &= 0.9 \cdot R_i \end{aligned} \tag{1}$$

Additionally, the capacitance of the first and last turns of the coil was a topic of investigation. Due to fringing effect [73] [74] the capacitance value was increased by a fringing factor k_f. The fringing effect is noteworthy in this particular case because of the protruding end-winding present at the first and last turns of the coil that increases the effective area of the insulation capacitance. The estimation of the k_f factor was done using the following suggested formula [75] which gives capacitance considering the fringing effect:

$$C_{fr} = \frac{\varepsilon_0 \cdot \varepsilon_r \cdot w \cdot l}{g} + \frac{\pi \cdot \varepsilon_0 \cdot \varepsilon_r \cdot (l + w)}{ln\left(\frac{\pi}{2} \cdot \left(1 + \frac{g}{t}\right) + \sqrt{\frac{\pi^2}{4} \cdot \left(1 + \frac{g}{t}\right)^2 - 1}\right)} \tag{2}$$

In the above equation the w and l correspond to the width and length of the capacitor plates, respectively, g is the separation between the plates, and t indicates the thickness of the plates. By comparing the newly calculated C_{fr} with the original C_i we get the value of $k_f \approx 1.1$. So the value we set for C_{end} compared to the original values is:

$$C_{end} = 1.1 \cdot C_i \tag{3}$$

Using all the new parameters developed above the final equivalent circuit model version is showcased, Fig. 3.41, along with the complete table of its parameters, Table 3.5.

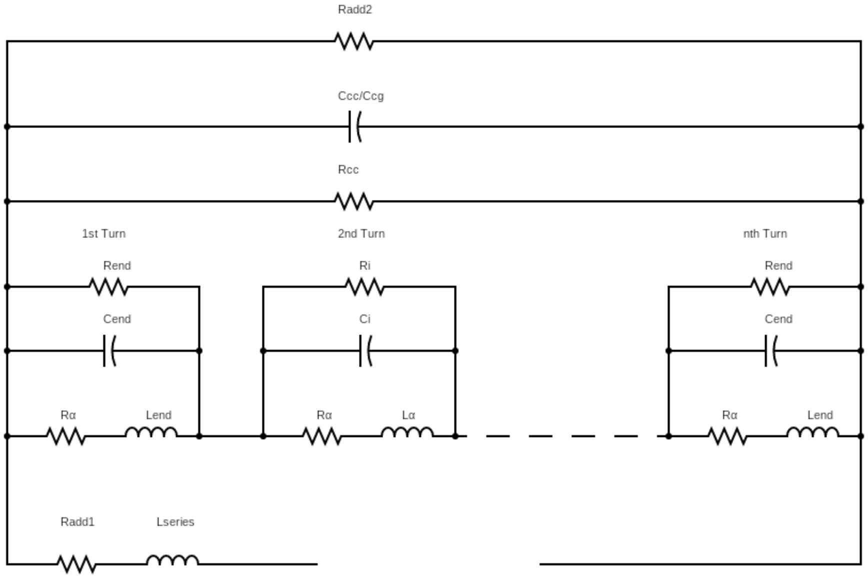

Figure 3.41: Final version the equivalent circuit model.

Name	**Description**
R_α	Internal turn resistance.
L_α	Single turn inductance
C_i	Capacitance between two turns of the coil.
R_i	Insulation resistance between two turns of the coil.
R_{cc}	Resistance between the core and coil.
C_{cc}	Capacitance between the core and coil.
R_{add1}	Resistance of the connection wiring.
L_{series}	Inductance of the connection wiring.
R_{add2}	Shunt resistance of the impedance spectroscopy equipment
C_{cg}	Coil to core capacitance at high frequencies.
R_{end}	Insulation resistance of first and last turns due to end effects.
L_{end}	Inductance of first and last turns due to end effects.
C_{end}	Insulation capacitance of first and last turns due to end effects.

Table 3.5: Final equivalent circuit parameter index.

Last but not least, the impedance and phase spectroscopies of the final version equivalent circuit model is comparison with experimental measurements are shown below, Fig. 3.42 and Fig. 3.43. The clear match between the two characteristics, especially in the zoomed area, makes this a satisfactory result.

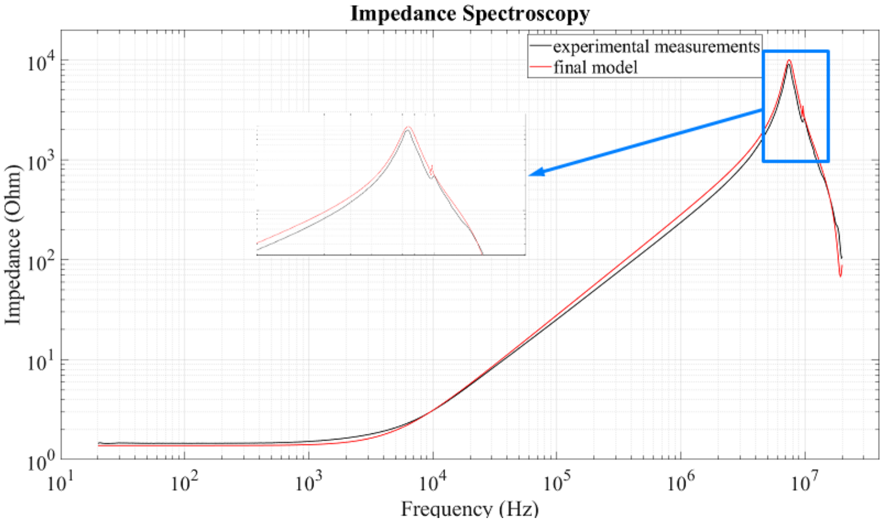

Figure 3.42: Impedance spectroscopy of the of the final version equivalent circuit model

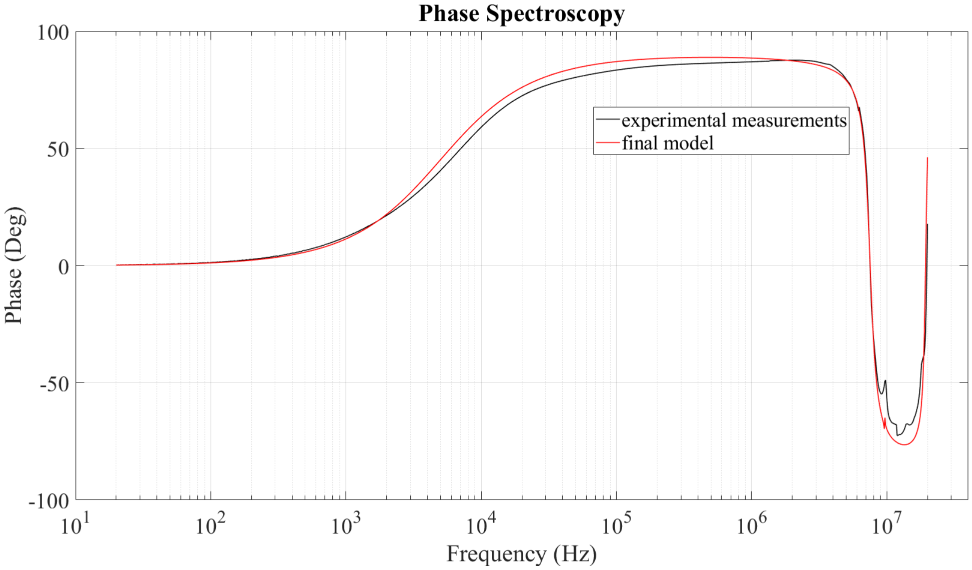

Figure 3.43: Phase spectroscopy of the final version equivalent circuit model

4 Chapter 4: Influence of potential manufacturing defects on the spectroscopy graph of the equivalent circuit model.

In this chapter, we will investigate how potential manufacturing tolerances could influence the corresponding impedance spectroscopy of said defective pole. To accomplish that, we will compare the impedance spectroscopy and Nyquist graphs produced from the healthy pole equivalent circuit model we developed in the previous chapter with the corresponding graphs after a single parameter had either an increase or decrease in value. The degree of change in the parameter value is always relative to the sensitivity of the model in FRA, in order for us to see a visible change in the respective graph. Afterwards, the differences between the graphs will be discussed, and a plain parameter analysis will be conducted. The simulations that produced the figures shown in this chapter were carried out in Matlab/Simulink environment.

4.1 Change in the value of C_i

Below we can see the impedance and phase spectroscopy graphs of the equivalent circuit model after we have increased and decreased the C_i capacitance, Fig. 4.1 and Fig. 4.2. It is evident that decreasing the C_i capacitance shifts both the impedance and phase to the right while increasing the C_i capacitance shifts both the impedance and phase to the left, while also making the second antiresonance point produced from the end winding appear later with respect to the main antiresonance point. From the Nyquist diagram, Fig. 4.3, we can spot the higher intensity of the second antiresonance point when C_i increases, as it happens earlier in the graph where the impedance has greater value, otherwise no other change can be identified between the graphs.

The value of the turn-to-turn capacitance of the coil, $C = \frac{\varepsilon \cdot A}{d}$ where A is the area of the plates of the capacitor, d is the spacing between the plates and ϵ is the permittivity of the material separating the plates, indicates how healthy the thin film insulation is.

A less than expected C_i capacitance value indicates problems with the turn-to-turn

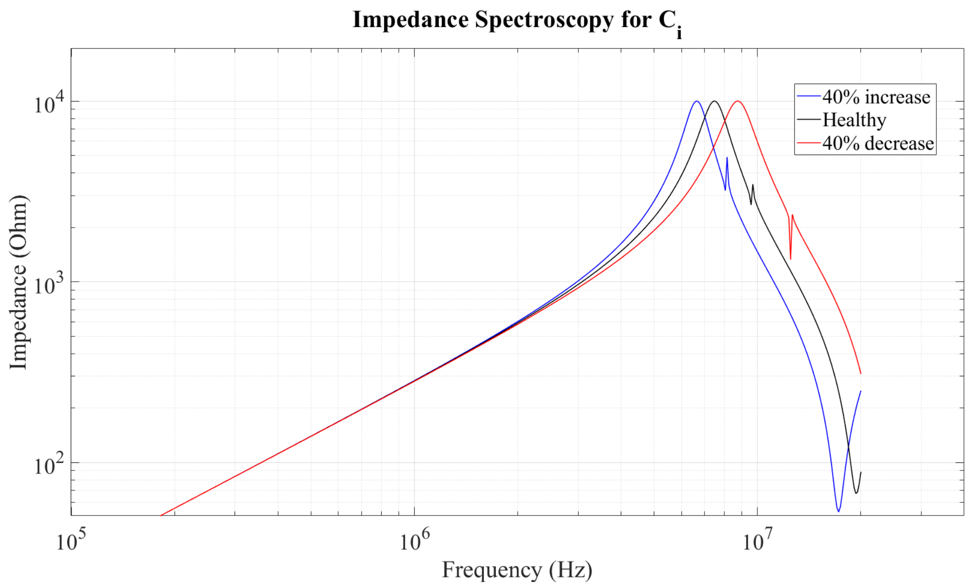

Figure 4.1: Impedance spectroscopy for different values of C_i

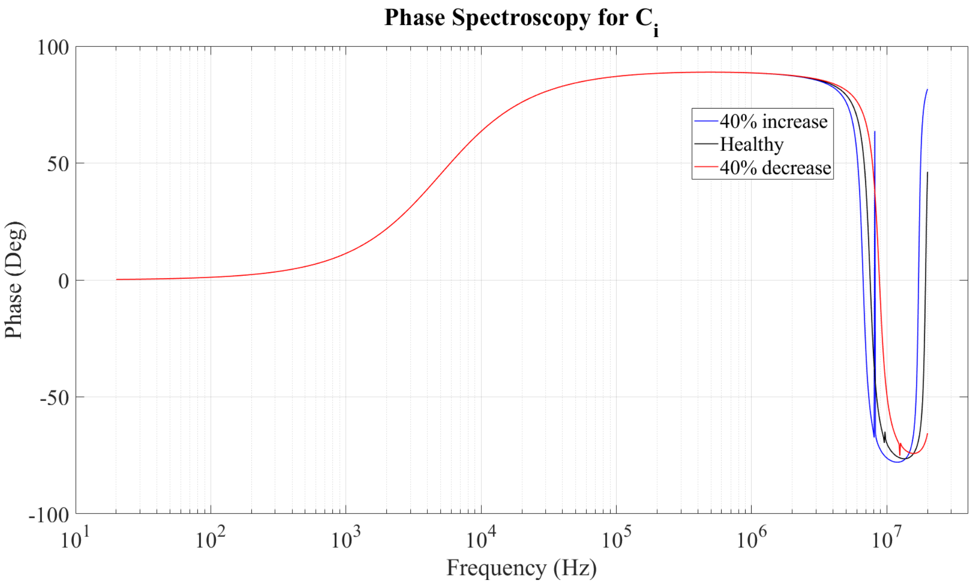

Figure 4.2: Phase spectroscopy for different values of C_i

insulation. A small permittivity ϵ, which is connected to the dielectric properties of a material, could be a sign of the bad condition of the insulation material during the manufacturing process. Another factor that could reduce the C_i capacitance is water of the insulation, which again reduces the permittivity ϵ of the insulation material. Water contamination however is not something irreversible, as the elimination of humidity could reveal a healthy pole suitable for use. Another cause could be trapped air bubbles between the insulation and the copper wire that were created during the manufacturing process,

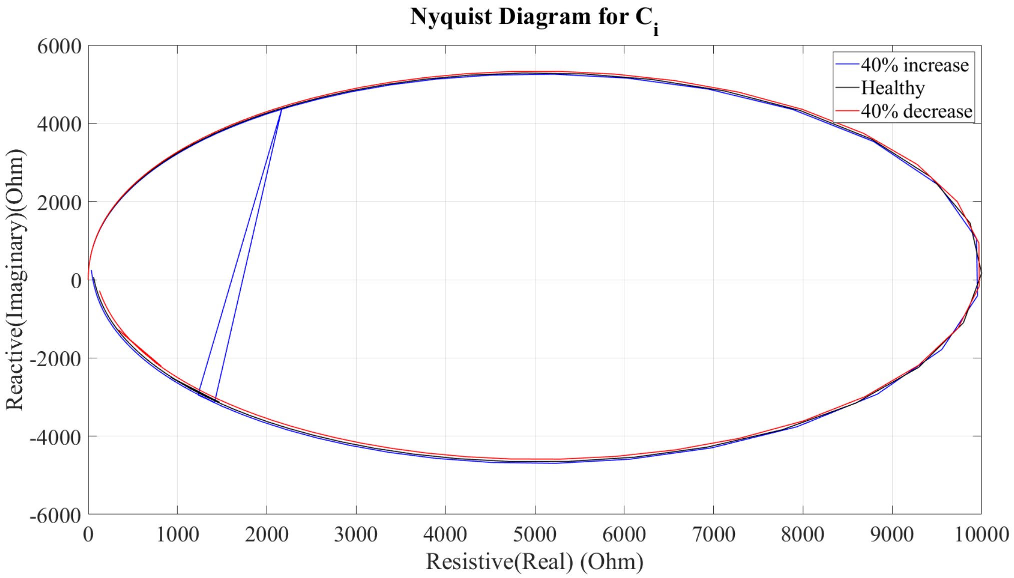

Figure 4.3: Nyquist diagram for different values of C_i

increasing the space d between them and decreasing the turn's overall capacitance.

A graph showing a capacitance value C_i higher than that of a healthy pole could again imply issues with the turn-to-turn insulation. Elevated turn capacitance suggests the presence of areas with thinner insulation. Thin insulation is weaker and increases the risk of turn-to-turn short circuits, posing a potential fault hazard for the coil.

4.2 Change in the value of R_i

Below we can see the impedance and phase spectroscopy graphs of the equivalent circuit model after we have decreased the R_i resistance by different factors, Fig. 4.4 and Fig. 4.5. If we compare the three graphs, it is clear that with the reduction of R_i the impedance graph does not shift while the magnitude of the first antiresonance decreases together with the R_i. Additionally, we can spot the impedance reached during the second antiresonance point increasing as R_i decreases, especially when its value drops to hundreds of Ohm. In the Nyquist diagram, Fig. 4.6, the reduction of the impedance magnitude during the main antiresonance and the increase of the impedance during the second antiresonance are more apparent than in the spectroscopy but there is nothing new to note. It is important to note that apparently the model's sensitivity to the turn-to-turn resistance value is not high as we had to drop the resistance's size class down to kiloohms for noticeable changes in the graphs.

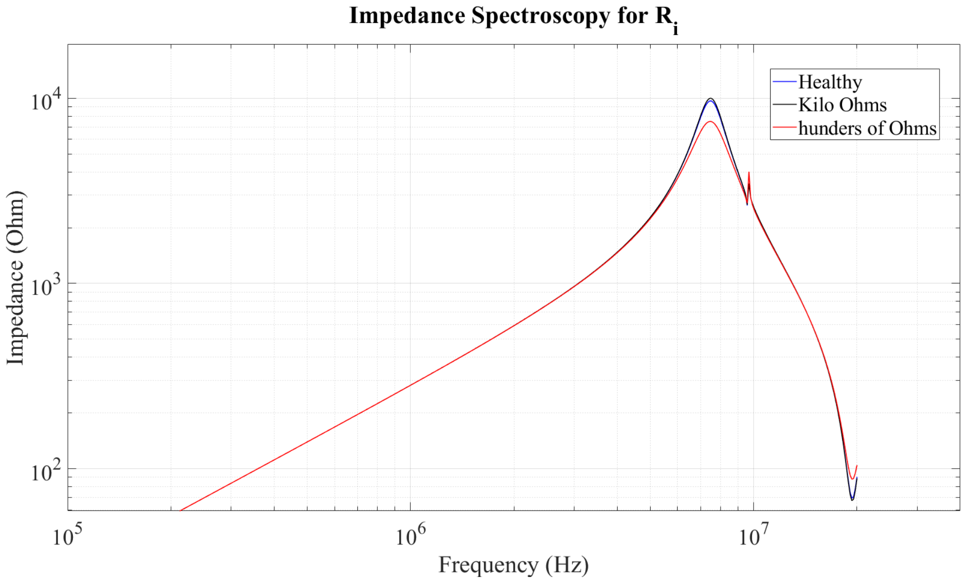

Figure 4.4: Impedance spectroscopy for different values of R_i

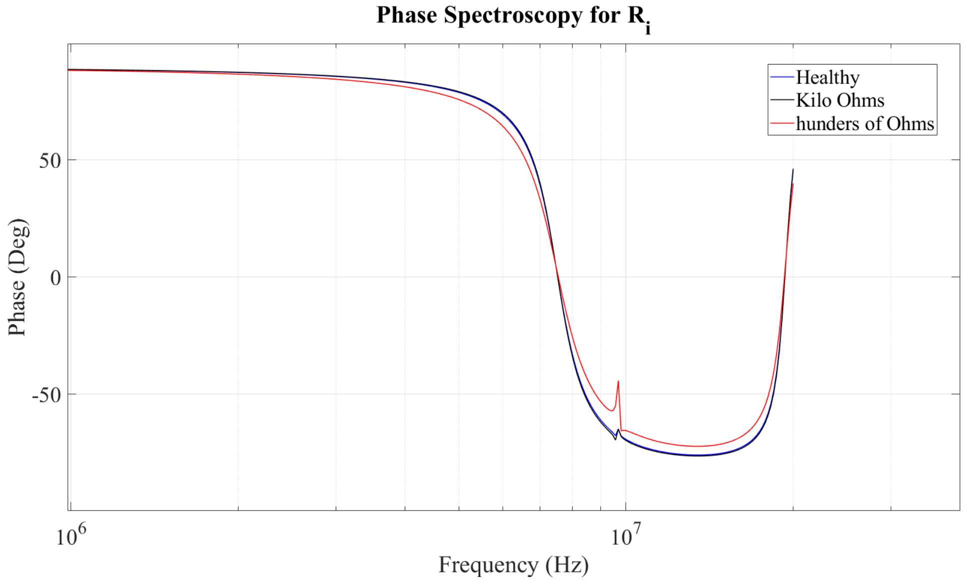

Figure 4.5: Phase spectroscopy for different values of R_i

The value of the turn-to-turn resistance of the coil, $R = \frac{\rho \cdot L}{A}$ where L is the thickness of the insulation, A is the cross-sectional area between the turns and ρ is the resistivity of the insulation material, indicates how healthy the thin film insulation is. A low R_i resistance value is an indication of a weak turn-to-turn insulation. A possible cause for it would be the poor state of the insulation material with a smaller resistivity ρ than required. Additionally, the existence of points in the insulation where its thickness is less than it should be is a

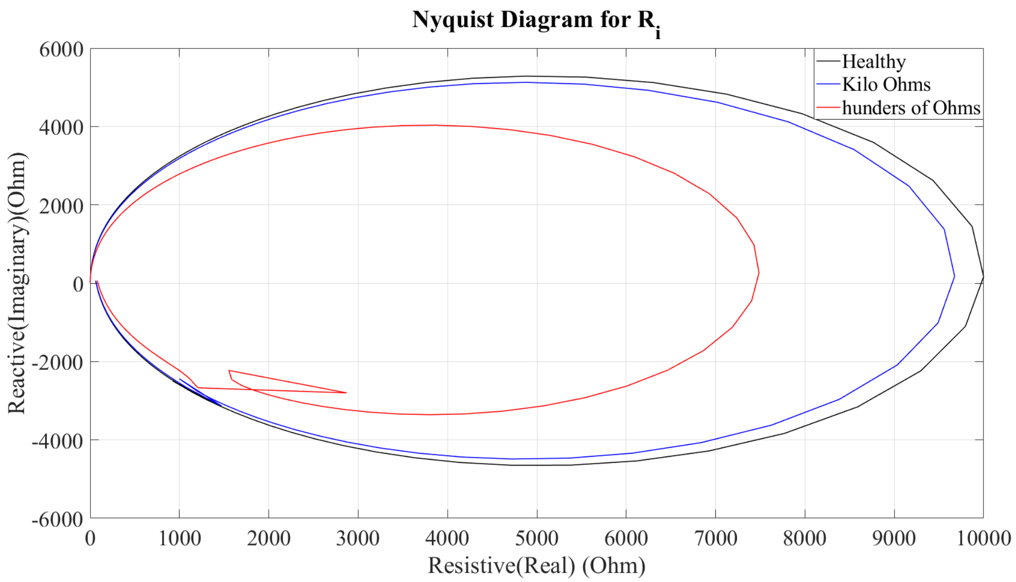

Figure 4.6: Nyquist diagram for different values of R_i

reason for a R_i value. Possible causes for a thin insulation would be stretching during the wounding procedure or a defect during its manufacturing. Finally the resistivity of the material used ρ could be reduced due to contamination of water, something reversible as mentioned previously.

4.3 Change in the value of R_{cc}

The impedance and phase spectroscopy plots of the equivalent circuit model, after reducing the R_i resistance by various factors, are shown in Fig. 4.9 and Fig. 4.10. When comparing the three graphs, it is evident that reducing R_{cc} does not shift the impedance plot; however, the magnitude of the first antiresonance decreases in proportion to R_{cc}. Additionally, the impedance at the second antiresonance point increases more significantly as R_{cc} decreases, showing a greater rise than observed in the R_{cc} impedance graph. In the Nyquist diagram (Fig. 4.11), the decrease in impedance at the main antiresonance and the increase at the second antiresonance are more noticeable than in the spectroscopy graphs, but no new insights are gained. It is worth mentioning that the model seem to show medium sensitivity towards the variation of coil-to-core resistance. However, this a much better case compared to the sensitivity of R_{cc} as reducing the R_{cc} to the hundreds of kiloohms mark showed a noticeable change is the graphs.

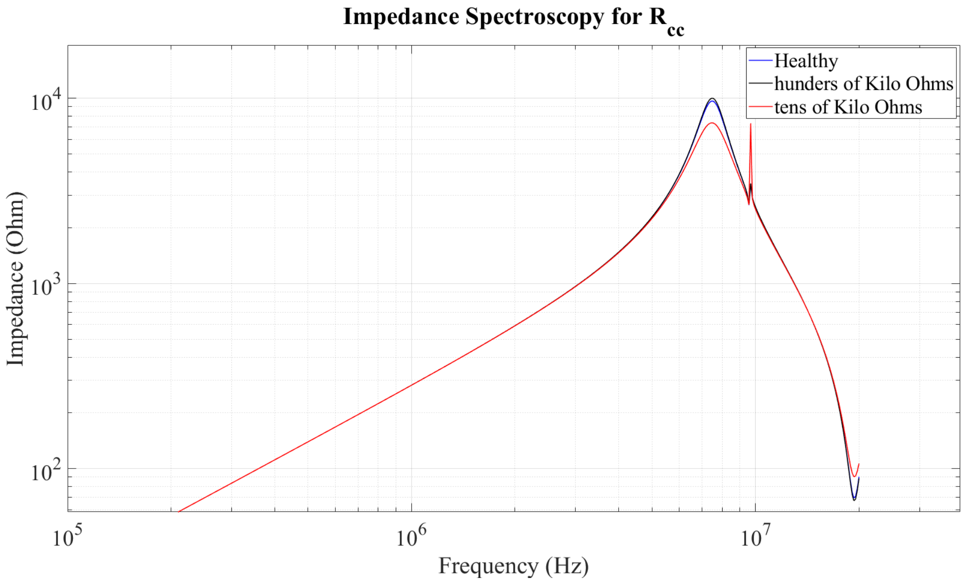

Figure 4.7: Impedance spectroscopy for different values of R_{cc}

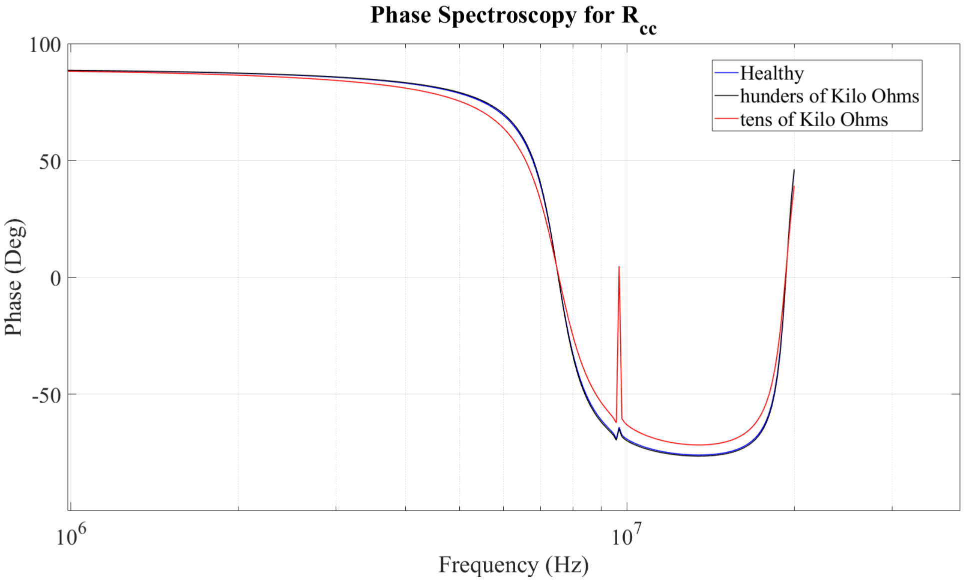

Figure 4.8: Phase spectroscopy for different values of R_{cc}

The value of the coil-to-core resistance is a sign about the health of the coil-to-core insulation that prevents a potential short circuit ground fault. Damage to the coil-to-core insulation as the coil is wound around the core, thus making the coil have direct contact to the core, is the most prevalent cause for a low R_{cc} resistance value. Moreover, improper impregnation of the coil windings with varnish or resin can leave air pockets or voids, creating weak spots where electrical leakage can occur due to the insulation weakness. Finally, again the presence of water contamination reduces the insulation material resistivity and could be

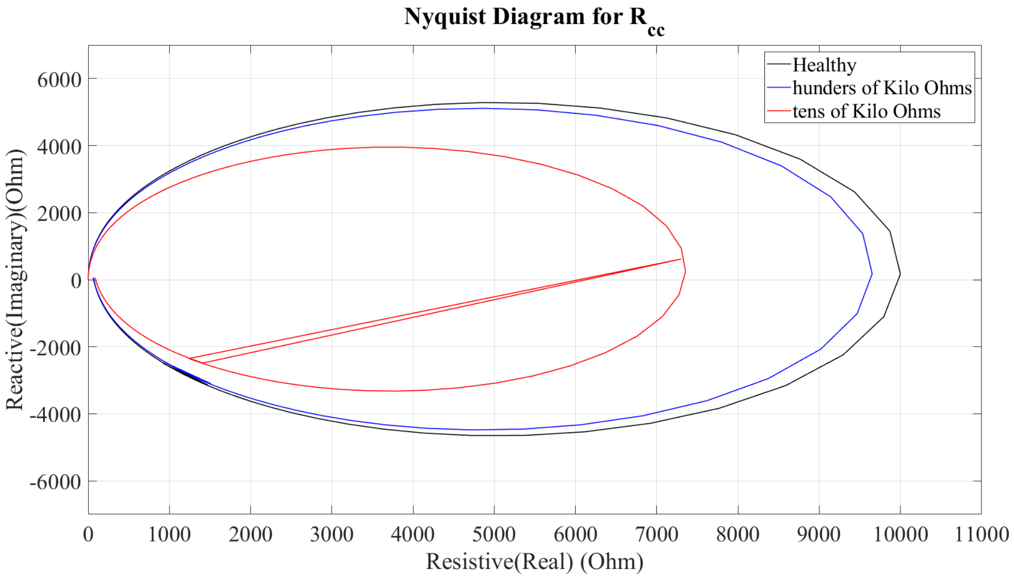

Figure 4.9: Nyquist diagram for different values of R_{cc}

the reason behind a meagre R_{cc} value.

4.4 Change in the value of C_{cc}

The impedance and phase spectroscopy graphs of the equivalent circuit model, shown in Fig. 4.10 and Fig. 4.11, reflect the effects of increasing and decreasing the C_{cc} capacitance. Notably, reducing the C_{cc} capacitance shifts both impedance and phase to the right, similar to what occurs when C_{cc} is reduced. However, the behaviour of the second antiresonance point differs, as its frequency remains constant despite the overall shift in the graph. This consistency makes it a distinguishing feature for detecting changes in C_{cc} versus changes in C_{cc}. In the Nyquist diagram, Fig. 4.12, the second antiresonance point becomes more pronounced when C_{cc} increases, as it occurs earlier in the graph where impedance is higher. Apart from this, no other significant differences between the graphs are observed.

The value of the coil-to-core capacitance of the coil, $C = \frac{\varepsilon \cdot A}{d}$ where A is the area of the plates of the capacitor, d is the spacing between the plates and ϵ is the permittivity of the material separating the plates, generally indicates how healthy the overall insulation between the coil and iron core is.

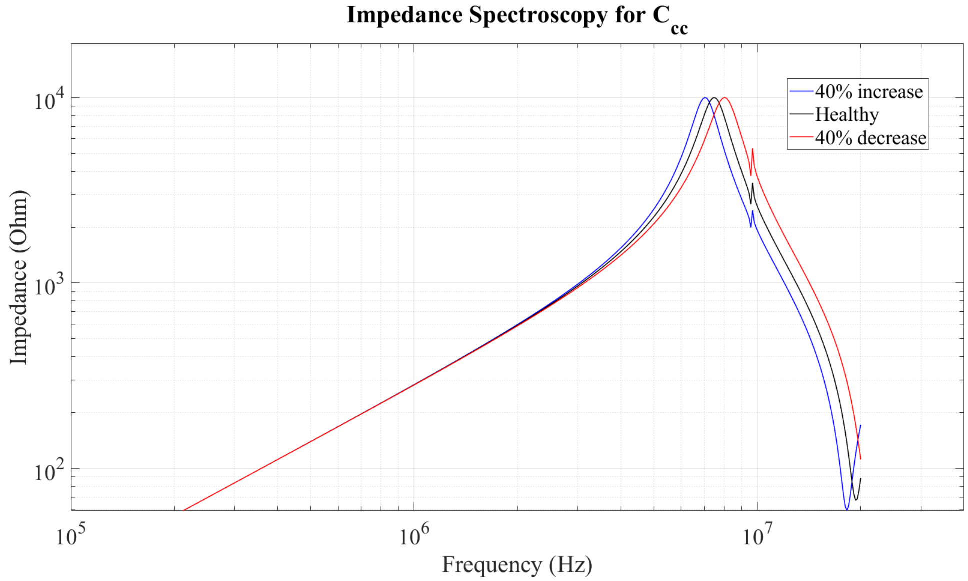

Figure 4.10: Impedance spectroscopy for different values of C_{cc}

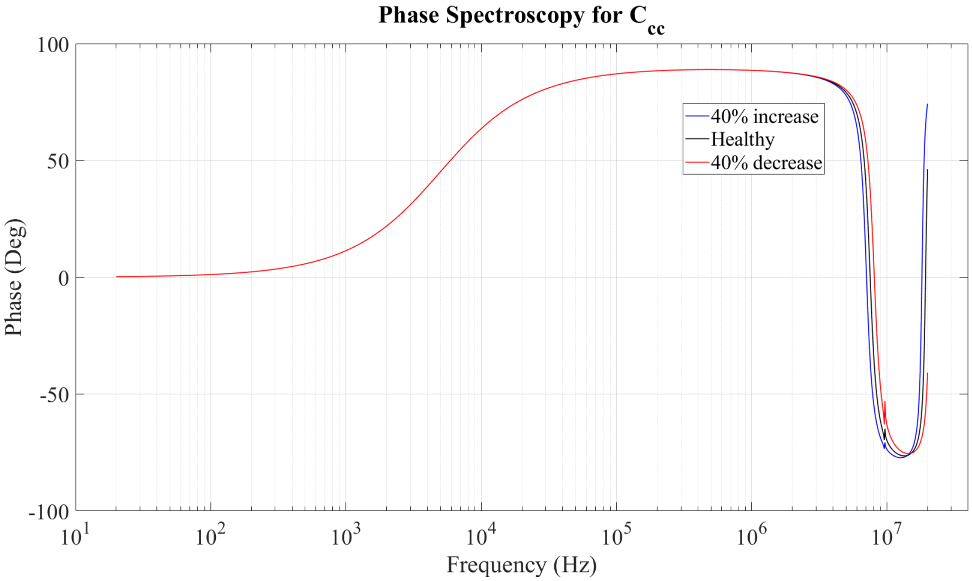

Figure 4.11: Phase spectroscopy for different values of C_{cc}

A lower-than-expected C_{cc} capacitance value can indicate implications with the coil-to-core insulation. A reduced capacitance, caused low permittivity ϵ, may be a sign towards the bad condition of the insulation applied during the coating process. Another factor that can lead to decreased C_{cc} capacitance is the presence of water contamination within the coil-to-core insulation, which also reduces the permittivity ϵ of the material. Additionally, insufficient application of resin between the coil and the core can leave the insulation inadequate to handle the operating voltage, something that will also reduce the C_{cc} capacitance.

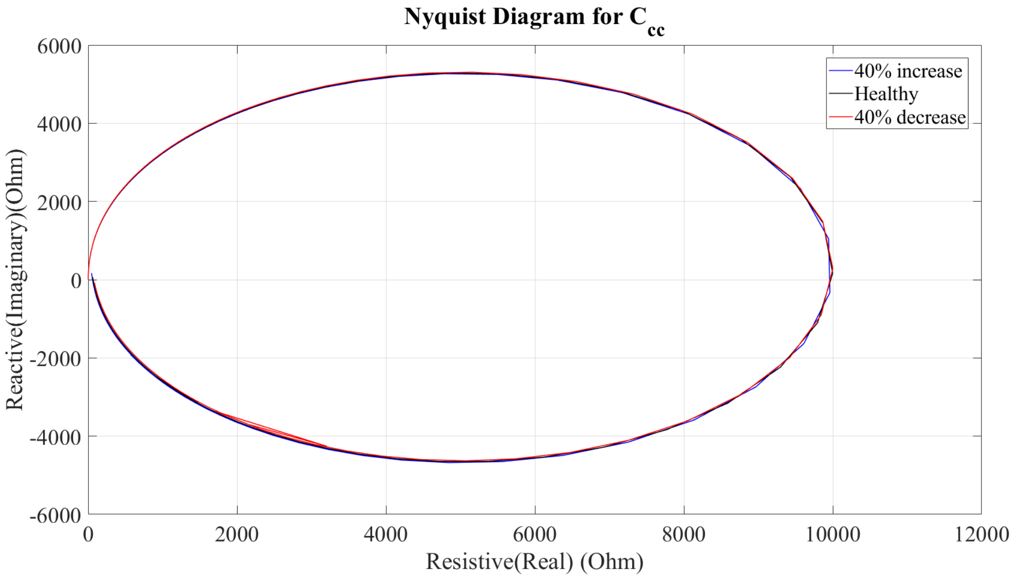

Figure 4.12: Nyquist diagram for different values of C_{cc}

On the other hand, a graph showing a capacitance value C_{cc} higher than that of a healthy pole may indicate problems with the turn-to-turn insulation as well. Damage to the coil-to-core insulation, possibly occurring during coil winding or from misalignment during pressing, could cause the coil to come into direct contact with the core, thus increasing the C_{cc} capacitance. Furthermore, excessive resin application during the impregnation process could fill most of the space between the coil and core with resin. Since resin has a higher permittivity than air, this would result in a higher-than-normal C_{cc} capacitance.

4.5 Change in the value of R_{end}

The impedance and phase spectroscopy plots of the equivalent circuit model, depicted in Fig. 4.13 and Fig. 4.14 respectively, illustrate the effects of varying the R_{end} resistance. Notably, decreasing the R_{end} resistance does not appear to shift the impedance or phase, and the peak impedance magnitude attained during the first antiresonance remains unchanged. However, the peak impedance magnitude at the second antiresonance point is highly sensitive to the reduction of R_{end}. In the Nyquist diagram, Fig. 4.15, these observations are also evident, with nothing new noticed.

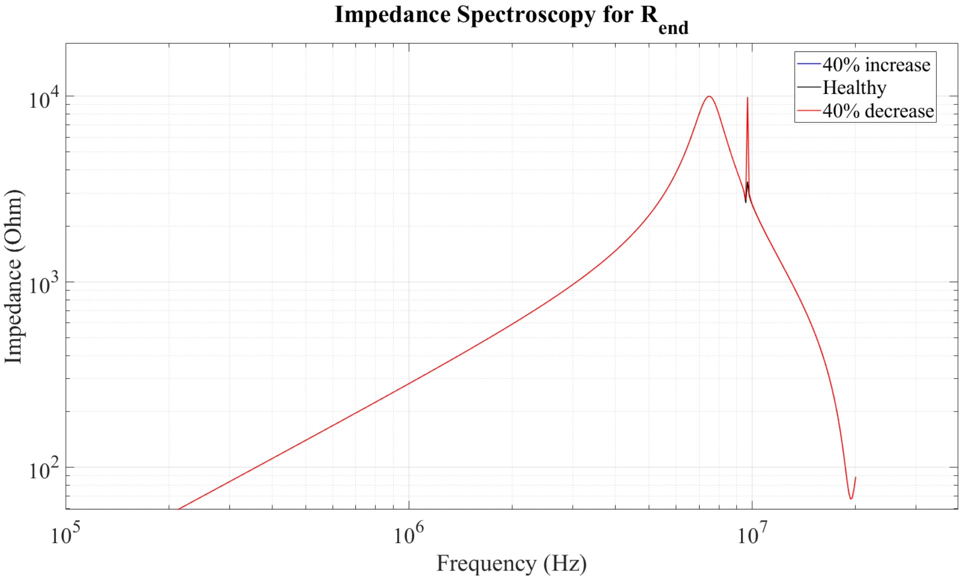

Figure 4.13: Impedance spectroscopy for different values of R_{end}

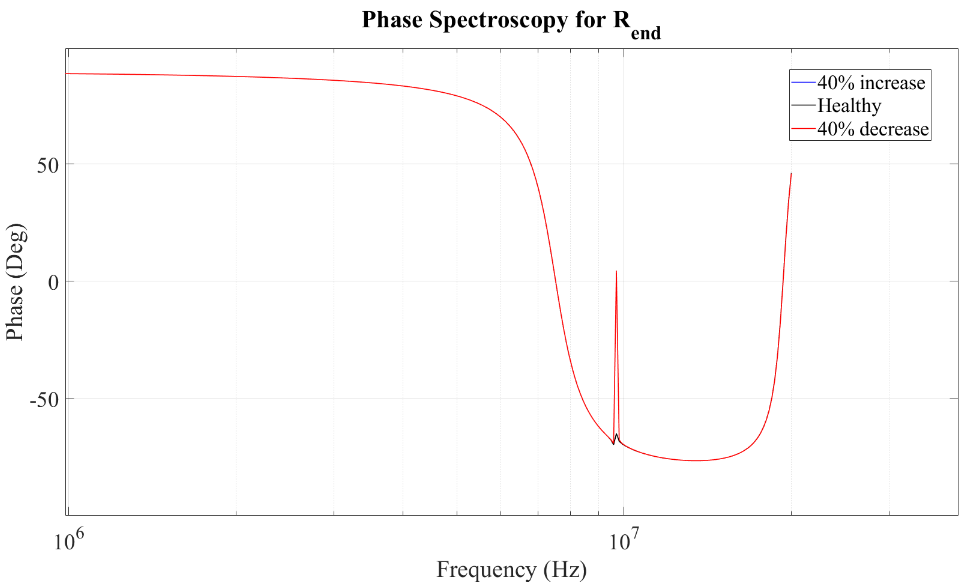

Figure 4.14: Phase spectroscopy for different values of R_{end}

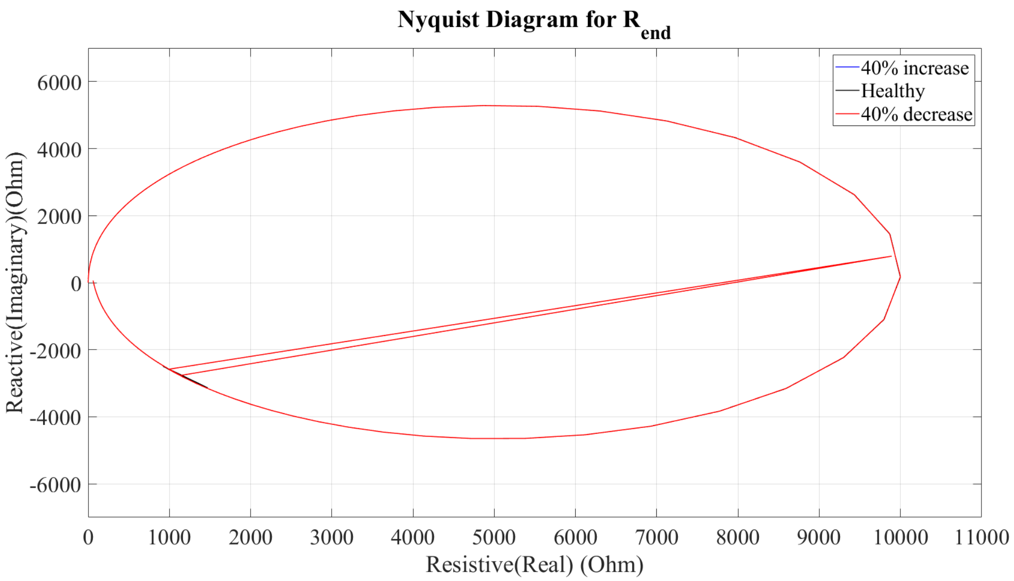

Figure 4.15: Nyquist diagram for different values of R_{end}

4.6 Change is the value of L_{end}

The impedance and phase spectroscopy plots of the equivalent circuit model, depicted in Fig. 4.16 and Fig. 4.17 respectively, illustrate the effects of varying the L_{end} inductance. Notably, decreasing the L_{end} slightly shifts the graphs to the right while the opposite effect is observed when increasing L_{end}, with this change being more clear in the highlighted area of the phase graph. Furthermore, the location where the second antiresonance occurs as well as its intensity are a subject of change. More specifically, the second resonance occurs at a lower frequency if L_{end} increases and happens at a higher frequency if L_{end} decreases, while in both scenarios its intensity being higher than before the change. In the Nyquist diagram, Fig. 4.18, both the change in the intensity and the location of the second resonance is noticeable, with nothing new to add.

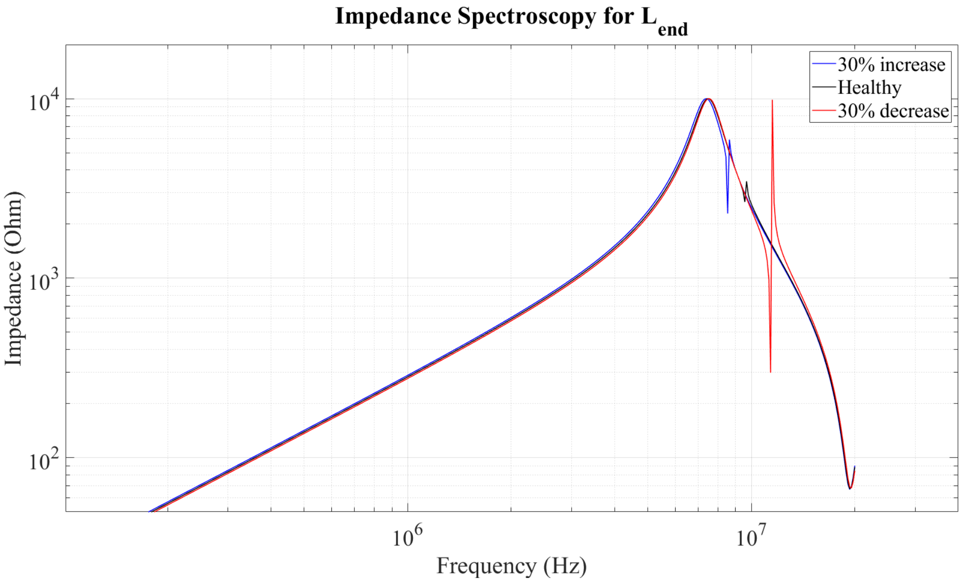

Figure 4.16: Impedance spectroscopy for different values of L_{end}

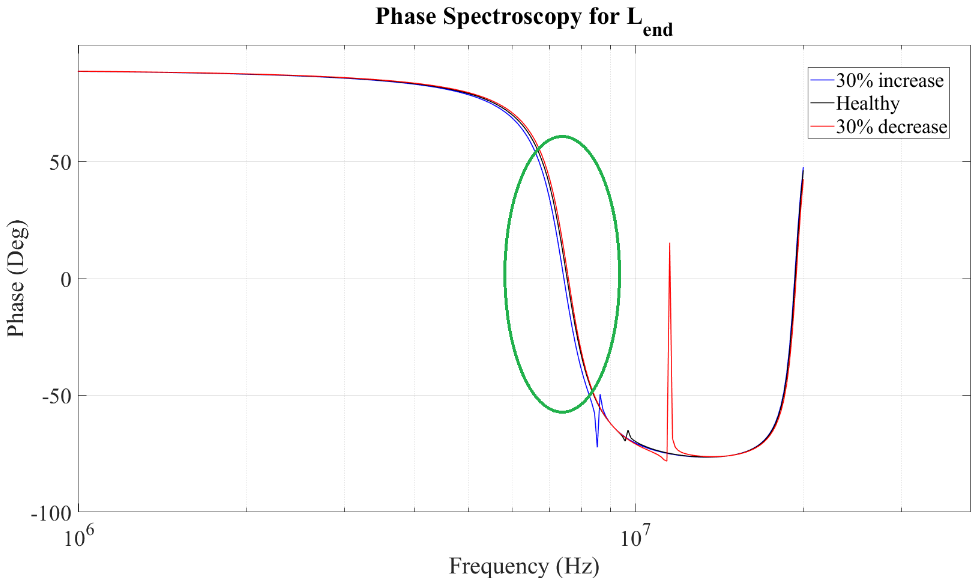

Figure 4.17: Phase spectroscopy for different values of L_{end}, in the highlighted area we can see the shift of the phase graph.

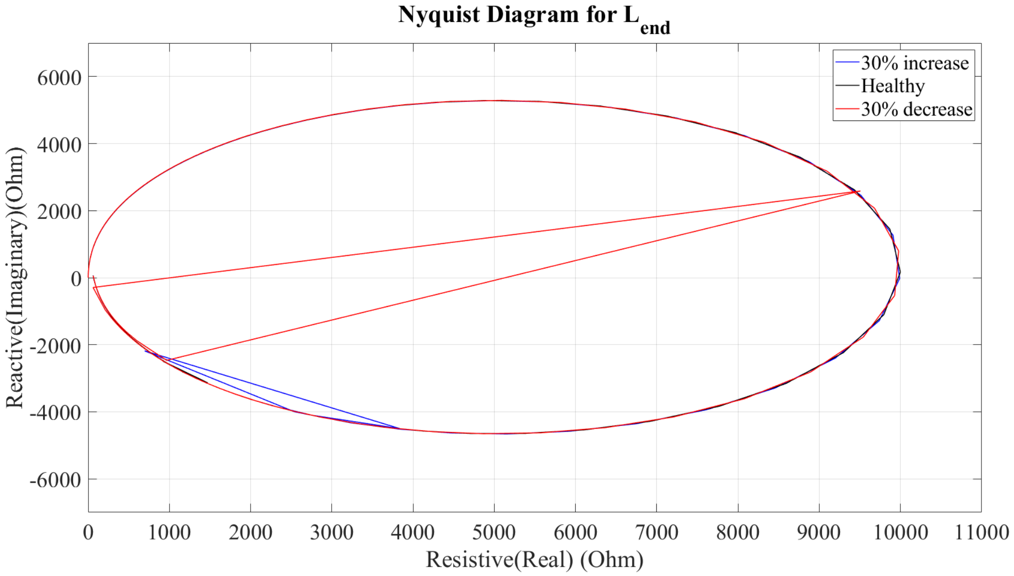

Figure 4.18: Nyquist diagram for different values of L_{end}

4.7 Change is the value of C_{end}

The impedance and phase spectroscopy plots of the equivalent circuit model, depicted in Fig. 4.19 and Fig. 4.20 respectively, illustrate the effects of reducing the C_{end} capacitance by different factors. Notably, decreasing the C_{end} does not influence the graphs other than changing the location and increasing the magnitude of the second antiresonance. On the other hand, if C_{end} is increased the second antiresonance takes place earlier in the graph and its intensity is again increased. In the Nyquist diagram, Fig. 4.21, both the change in the intensity and the location of the second resonance is noticeable, with nothing new to add.

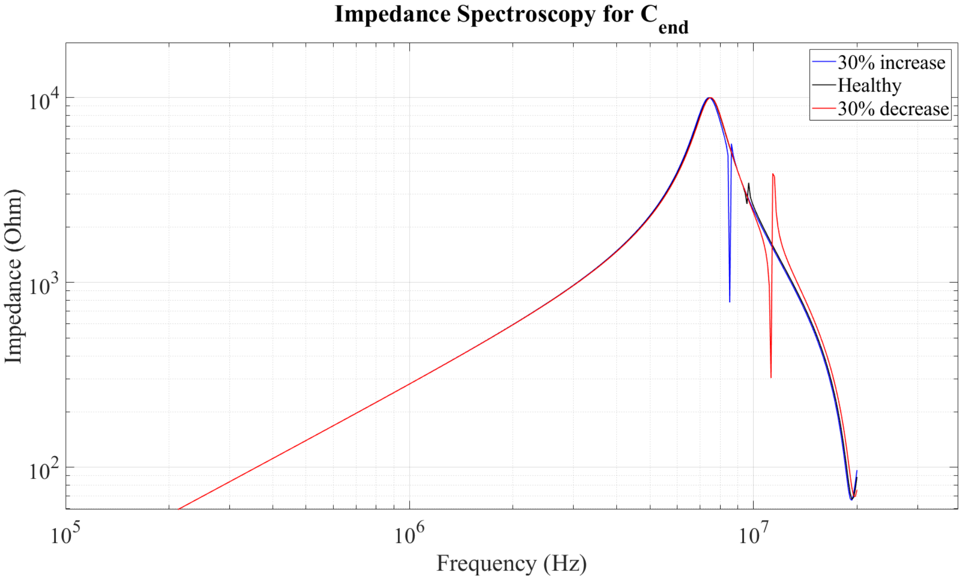

Figure 4.19: Impedance spectroscopy for different values of C_{end}

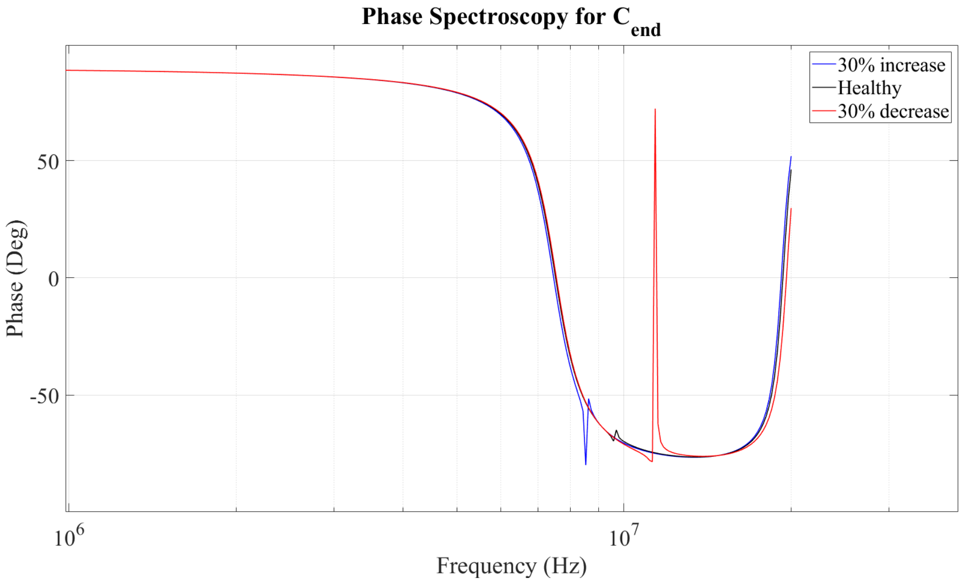

Figure 4.20: Phase spectroscopy for different values of C_{end}

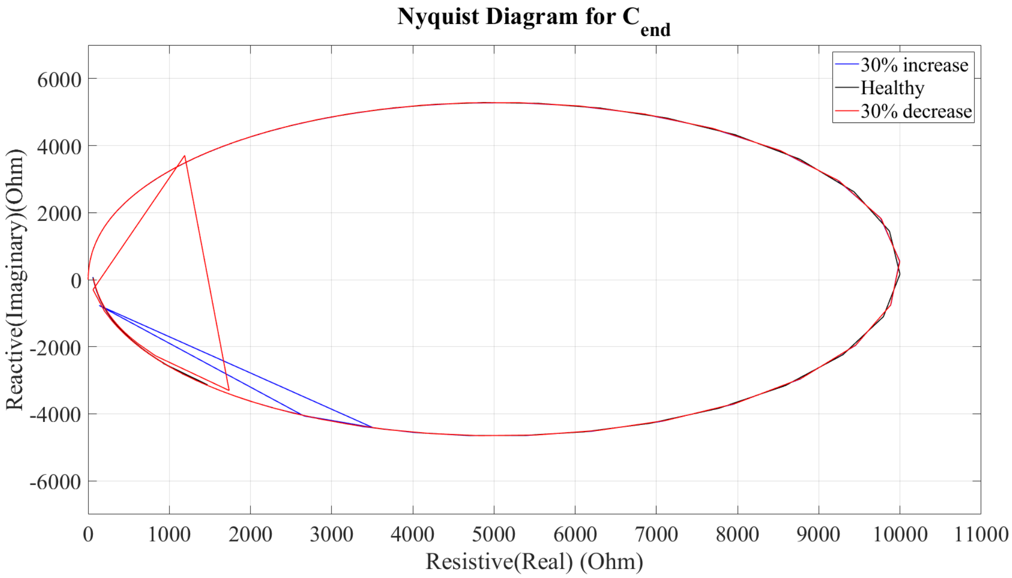

Figure 4.21: Nyquist diagram for different values of C_{end}

4.8 Model parameter analysis tables.

Parameter	**Influence to graph when increased**	**Influence to graph when decreased**
C_i	The whole graph shifts left, and the second antiresonance shift left with respect to the new first antiresonance	The whole graph shifts right, and the second antiresonance shift right with respect to the new first antiresonance
R_i	Graph shows no changes	Low sensitivity, visible reduction to the maximum impedance attained during the main antiresonance when the value drops to hundreds of Ohms
R_{cc}	Graph shows no changes	Medium sensitivity, visible reduction to the maximum impedance attained during the main antiresonance and the second antiresonance when the value drops to tens of kiloohms
C_{cc}	The whole graph shifts left, however the frequency value that the second antiresonance point take place remains unchanged	The whole graph shifts right, however the frequency value that the second antiresonance point take place remains unchanged
R_{end}	Graph shows no changes	Increase in maximum impedance attained during the second antiresonance
L_{end}	Slight shift of the graph to the left which is more apparent in the phase graph, second resonance happens at a lower frequency value and its shape changes	Slight shift of the graph to the right which is more apparent in the phase graph, second resonance happens at a higher frequency value and its shape changes
C_{end}	Slight shift of the graph to the left which is more apparent in the phase graph, second resonance happens at a lower frequency value and its shape changes	Slight shift of the graph to the right which is more apparent in the phase graph, second resonance happens at a higher frequency value and its shape changes

Table 4.1: Parameter mapping concerning the impedance and phase spectroscopy

Parameter name	**Influence to graph when increased**	**Influence to graph when decreased**
C_i	Only the second antiresonance shifting left is visible	Only the second antiresonance shifting right is visible
R_i	Graph shows no changes	Low sensitivity, visible reduction to the maximum impedance attained during the main antiresonance when the value drops to kiloohms
R_{cc}	Graph shows no changes	Medium sensitivity, visible reduction to the maximum impedance attained during the main antiresonance and the second antiresonance when the value drops to hundreds of kiloohms
C_{cc}	Graph shows no changes	Graph shows no changes
R_{end}	Graph shows no changes	The intensity of the second antiresonance is increased
L_{end}	Second resonance happens earlier in the graph and its intensity is increased	Second resonance happens later in the graph and its intensity is increased
C_{end}	Second resonance happens earlier in the graph and its intensity is increased	Second resonance happens later in the graph and its intensity is increased

Table 4.2: Parameter mapping concerning the Nyquist Diagram

5 Chapter 5: Experimental Multifactor Ageing

In this last chapter of this thesis, we will investigate how the conclusions derived from the theoretical analysis and modelling conducted in the previous chapters are connected with experimental ageing results. To accomplish that, we would have to subject healthy poles to accelerated ageing. Afterwards, by utilising the data produced we will evaluate the impact of manufacturing defects on stressed poles and the effectiveness of impedance spectroscopy and Nyquist Diagrams as a quality assessment procedure for permanent magnet synchronous machine poles.

As an essential first step, we had to choose what kind of degradation tests we would have the poles undergo. After careful consideration we decided to subject different groups of poles to different combinations of fixed thermal stress, thermal cycling stress and mechanical stress. The wide array of stresses will provide us with a large range of data and will provide further insight towards our end goal.

It is important to note that before any pole was put through its predetermined ageing process, its healthy state impedance spectroscopy was extracted. Furthermore, again prior to its ageing process every pole available was subjected to a 12-minute-high-voltage (HV) 5kV test for the measurement of their respective coil-to-core resistance, as stated in Section 3.2.1. As this test was done at a very high voltage value it will be considered as electrical stress. Thus, we obtained the impedance spectroscopy of each pole after it had undergone the high voltage test as well.

5.1 Fixed Thermal Stress

This experimental procedure aims to simulate the thermal stress that the pole experiences during long term fixed motor operation, with a group of 6 poles used as test subjects. To acquire data on the gradual degradation of the poles, the procedure was separated into several cycles. At the start of each cycle, all 6 poles were placed inside an oven set to maintain a constant temperature for a selected duration. Following the end of the ageing duration, the poles were extracted from the over and remained in room temperature until they had cooled off. After the poles were cool enough to be handled, their impedance spectroscopy was acquired and then they were placed inside the oven for another ageing cycle. Below, the ageing strategy adopted for the fixed thermal ageing is showcased:

Cycle number	**Temperature(°C)**	**Duration**
C1	200	6 hours
C2	207.5	6 hours
C3	215	6 hours
C4	220	6 hours
C5	225	6 hours
C6	230	6 hours
C7	240	6 hours

Table 5.1: Fixed thermal stress strategy

The collective behaviour of impedance spectroscopy, phase spectroscopy and Nyquist Diagram graphs for poles 34A-39A is depicted below, Fig. 5.1-Fig. 5.3.

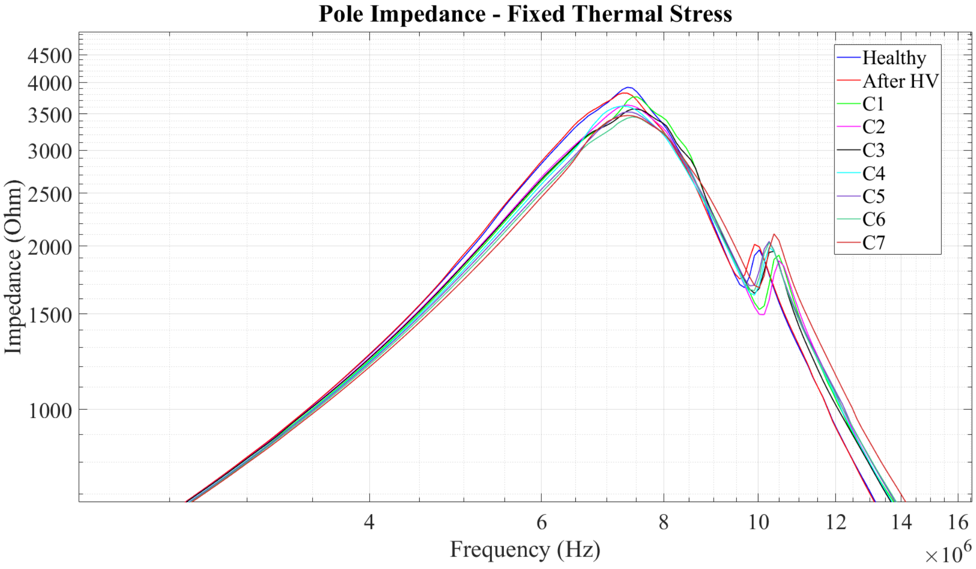

Figure 5.1: Collective impedance spectroscopy of 34A-39A for all thermal cycles

The impact of the high voltage test is visible as the impedance spectroscopy of the poles shifted slightly to the left. This was a strange result compared to the one we envisioned, being the degradation of the coil-to-core insulation signalled by a shift of the graph to the right and the reduction in impedance attained during the main antiresonance. Instead, we see the whole graph slightly shift to the left combined with the reduction in impedance attained during the main antiresonance. According to the parameter analysis carried out in Chapter 4, this is a

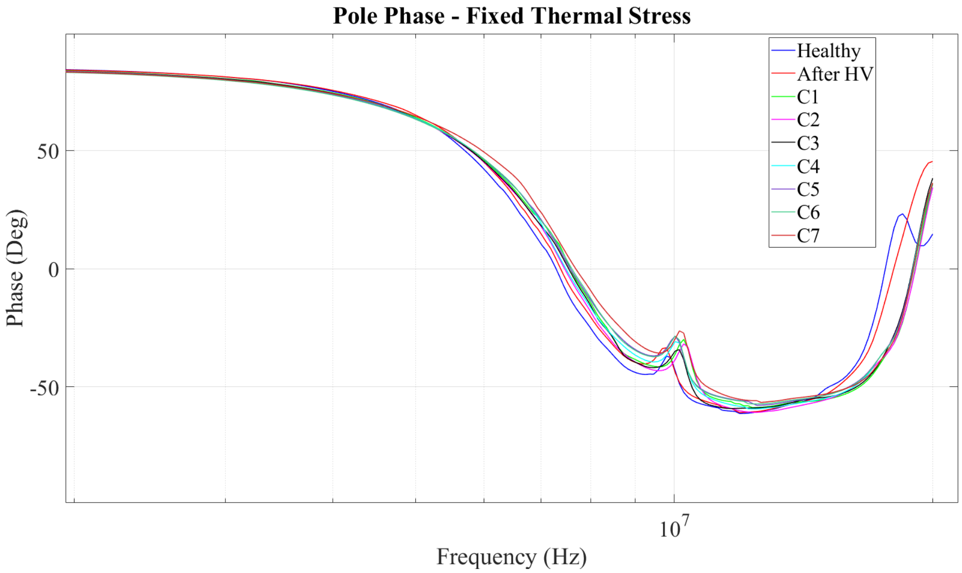

Figure 5.2: Collective phase spectroscopy of 34A-39A for all thermal cycles

sign of increased C_{cc} and C_i and a lowered R_{cc}. The reduction of R_{cc} is an expected result of the electrical stress that the coil-to-core insulation enduring during the HV test.However, the odd increase in the coil-to-core and turn-to-turn capacitances could be a result of the elimination of water contamination of the coil-to-core and turn-to-turn insulations during the HV test process by the means of electrolysis, as 1.23 Volts are sufficient to conduct water electrolysis [76].The elimination of water contamination would bolster the dielectric properties of the insulation, thus increasing the permittivity ϵ and the overall capacitance.

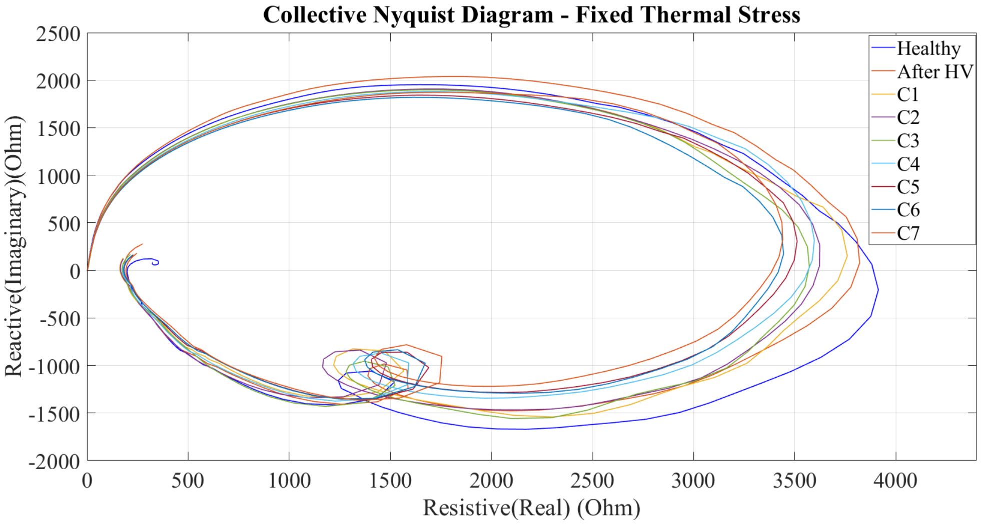

Figure 5.3: Collective Nyquist Diagram of 34A-39A for all thermal cycles

As far as the effect of the fixed thermal stress cycles is concerned, we can see a clear pattern. As the insulation system of the pole get more and more aged the graph is being shifted to the right, the maximum impedance attained during the main antiresonance is reduced and the second antiresonance spot is shifted to the right. According to the model parameter analysis, the graph shifting to the right in combination with the second antiresonance spot being shifted to the right signals the reduction of C_{cc} and Ci. The increase of said values indicates the wear of the insulation however it will not identify its cause as there are a couple of possible scenarios. Firstly, the reduction of the permittivity ϵ, which is connected to the dielectric properties of the material used for the thin film insulation, could be a potential cause. Another cause could be the delamination of the insulation from the copper wire, allowing air to reside between the wire and the insulation increasing the space d between them. Finally a combination of both above scenarios is a possible case. The reduction of the maximum impedance attained during the main antiresonance is, as mentioned earlier, connected to the lowered R_{cc} and R_i values. The main factor for the reduction of R_{cc} and R_i is insulation material resistivity ϱ getting lower due to thermal ageing.

Now for us to explore the effect that manufacturing defect have on the insulation wear process due to fixed thermal stress, we will choose 2 poles of the group and analyse their behaviour. The first one will be the pole from the group whose healthy impedance spectroscopy graph shows a high probability for the presence of manufacturing defects, while the second will be the one whose healthy impedance spectroscopy graph shows a high probability for the presence of manufacturing defects. The selection process will be carried by comparing the said graphs with the one from the healthy pole prototype that the model was based around. In the figure below, Fig. 5.4, the comparison between healthy state impedance spectroscopy graphs for 34A to 39A poles and healthy pole prototype is depicted.

According to the criteria we expressed earlier, the poles chosen were pole 34A and pole 37A, as pole 34A seems to have spots with thin insulation due to its high capacitance and low resistance and pole 37A is the one with the highest resemblance to the healthy pole prototype. Next, the behaviour of each pole's impedance spectroscopy during the fixed thermal stress process is showcased, Fig. 5.5 and Fig. 5.6. There we can see each pole adheres to the

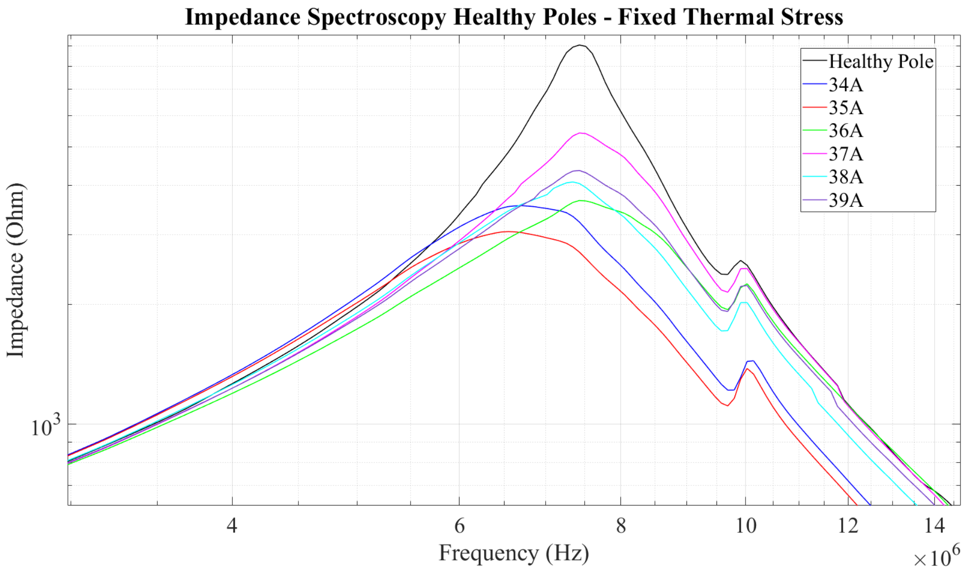

Figure 5.4: Healthy state impedance spectroscopy of 34A-39A poles

collective behaviour of its group to fixed thermal stress.

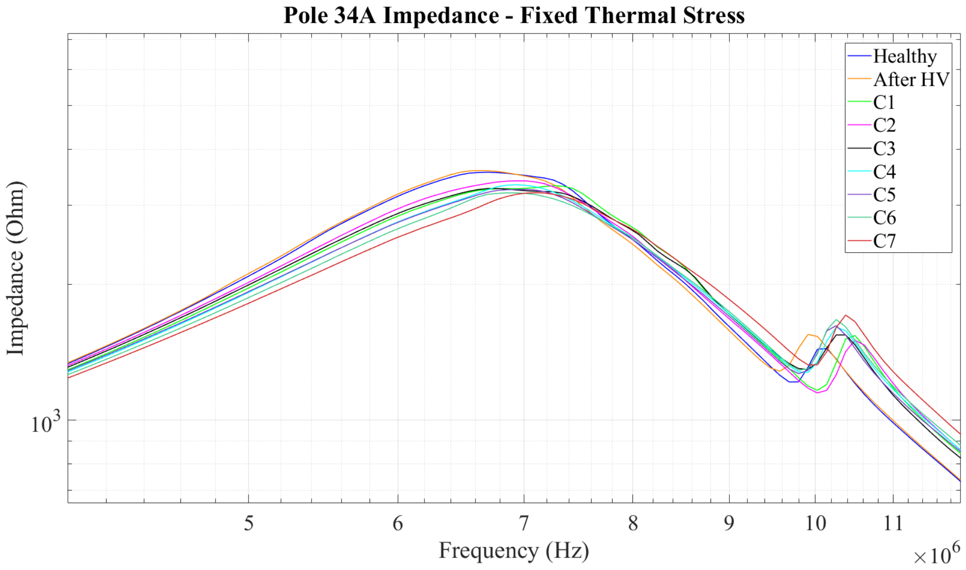

Figure 5.5: Impedance spectroscopy of pole 34A for all thermal cycles

To better exhibit how each pole behaves, a figure depicting the main antiresonance peak impedance location for both poles as the cycles progress, Fig. 5.7, as well as a figure for comparison purposes are provided, Fig 5.8.

Comparing the locations the peak appears during the ageing process of each pole the following remarks can be made. As far as pole 34A is concerned, apparent is the greater

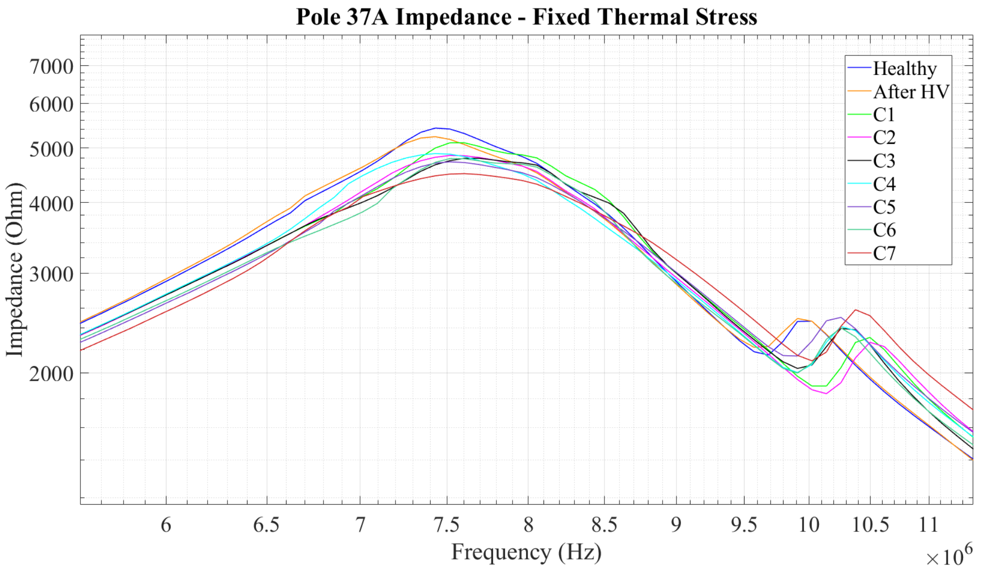

Figure 5.6: Impedance spectroscopy of pole 37A for all thermal cycles

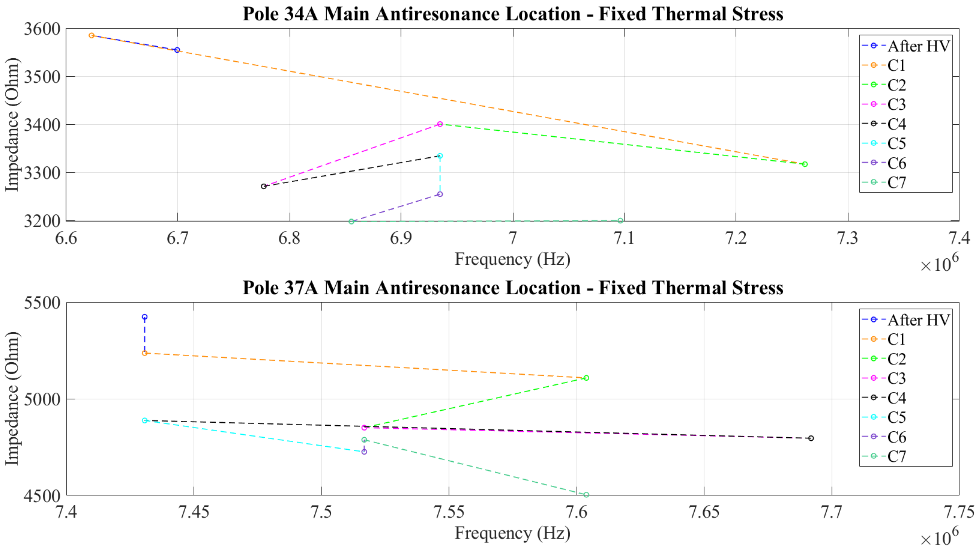

Figure 5.7: Main antiresonance peak impedance location for poles 34A(up) and 37A(down) for all thermal cycles

degree of variation on the frequency that the peak appears. This is an indication that the turn and coil-to-core capacitances are the main parameters that decrease during the ageing process. The capacitance decreasing at a rapid pace is evidence of the impact that the thermal stress has on the thin insulation spots of pole 34A identified from its healthy impedance spectroscopy graph. On the contrary regarding pole 37A, there seem to be a more homogeneous wear of the insulation system as its resistance and capacitance decrease

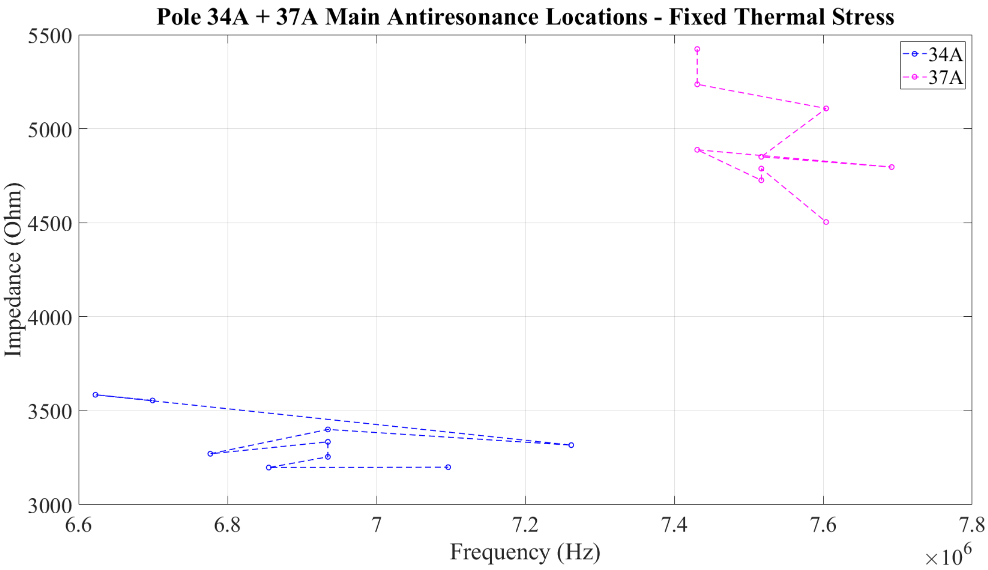

Figure 5.8: Comparison of main antiresonance peak impedance locations for 34A and 37A poles during all thermal cycles

at similar rates.

To conclude, the above observations verify our initial hypothesis concerning the presence of manufacturing defects in pole 34A. The fast reduction of capacitance during thermal stress cycles demonstrates the accelerated ageing of the epoxy resin as well as the faster degradation of the dielectric properties of the insulation material at the weak insulation spots of pole 34A compared to pole 37A.

5.2 Thermal Cycling and Mechanical Stress

This experimental procedure seeks to replicate the thermal response of the pole's insulating materials during motor operation across different load conditions, while ensuring only minor variations in temperature. To monitor the gradual degradation of the 12 poles that will take part in this stress test, the procedure was again divided into multiple cycles. At the beginning of each cycle, all 12 poles of the group were placed in an oven set to operate under varying power to achieve an oscillating temperature value across a set range for a predetermined period. Once the ageing phase concluded, the poles were removed from the oven and left at room temperature to cool. After cooling sufficiently for safe handling, impedance spectroscopy measurements were taken. The poles were then returned to the oven for the next ageing cycle. After 8 thermal cycling stress cycles, all poles were subjected to a HV test and a Breakdown test to assess the condition of their insulation systems. Lastly, the poles were subjected to mechanical stress by a device specifically made for this purpose, Fig, 5.9. The device's main feature is a wagon which can hold inside it a maximum of 6 poles at a time and has the ability to slide horizontal using linear bearings. After the poles were mounted on the wagon was it inserted in the C-shaped track depicted in Fig 5.10. Then it was then driven by an inverter-fed induction motor, which we converted its rotor's rotational motion into rapid horizontal movement. The inverter allowed us to regulate the frequency of the power that was being transmitted to the induction machine, giving us the ability to manipulate its rotational speed.

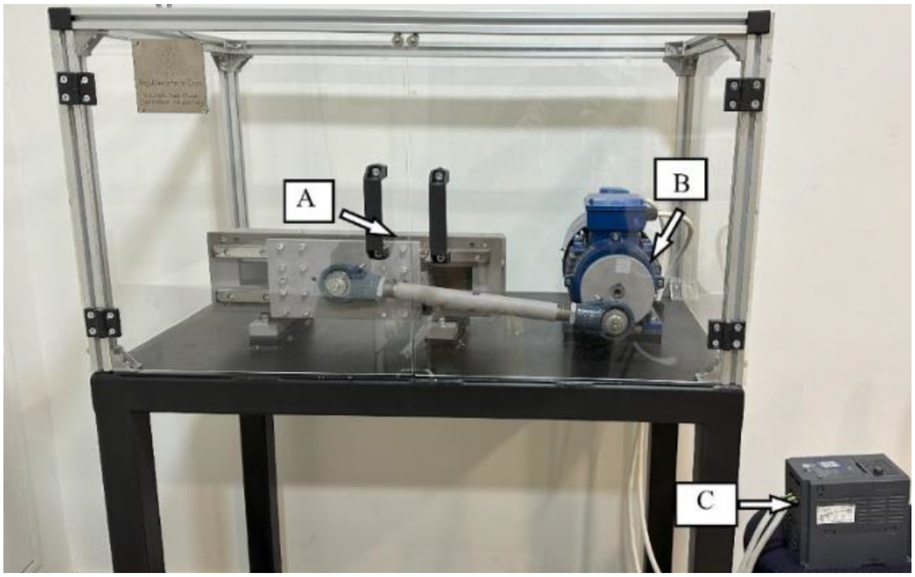

Figure 5.9: Mechanical stress set-up,(A) Mechanical vibration device, (B) Induction motor, (C) Inveter

All mechanical stress tests were carried out with the inverter set to 5 Hz, with the corresponding radial frequency of the rotor being 258 rpm with the device fully loaded. In Fig. 5.11 the mechanism that converts rotational motion into linear movement is illustrated which is driven by the motor, highlighting the disk's radius R and the length L_δ of the rod. The linear oscillation has an amplitude of 40 mm, with its acceleration and velocity, Fig. 5.12, calculated using the following equations.

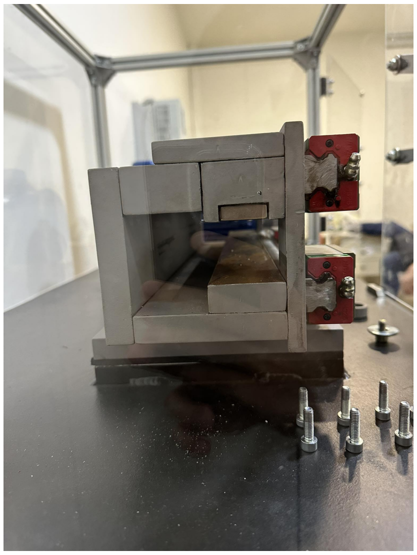

Figure 5.10: C-shapped track

$$u_{lin} = R \cdot \omega \cdot \left(sin(\omega \cdot t) - \frac{R}{2 \cdot L_\delta} \cdot \frac{sin(2 \cdot \omega \cdot t)}{\sqrt{1 - (\frac{R}{L_\delta})^2 \cdot sin^2(\omega \cdot t)}} \right) \tag{4}$$

$$u_{lin} = R \cdot \omega^2 \cdot cos^2(\omega \cdot t) - \frac{R}{2 \cdot L_\delta} \left(\frac{2 \cdot cos(2 \cdot \omega \cdot t))}{\sqrt{1 - (\frac{R}{L_\delta})^2 \cdot sin^2(\omega \cdot t)}} + \frac{\frac{1}{2} \cdot (\frac{R}{L_\delta})^2 \cdot sin^2(\omega \cdot t)}{\left(\sqrt{1 - (\frac{R}{L_\delta})^2 \cdot sin^2(\omega \cdot t)}\right)^3} \right) \tag{5}$$

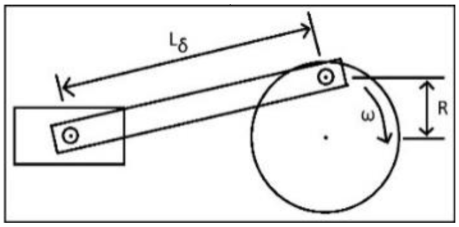

Figure 5.11: Radial to linear conversion mechanism

Worth mentioning is as well the fact that prior to the wagon being inserted in the C-shaped track, the poles mounted on it were connected in series. This in combination with the permanent magnets that we have situated above the location where the mounted poles would be present during the mechanical stress, Fig. 5.13, would create an alternating current in our poles due to induction. This means that the poles would also be subjected to a certain level of electrical stress. The circulating current's peak amplitude was about 4 A with the

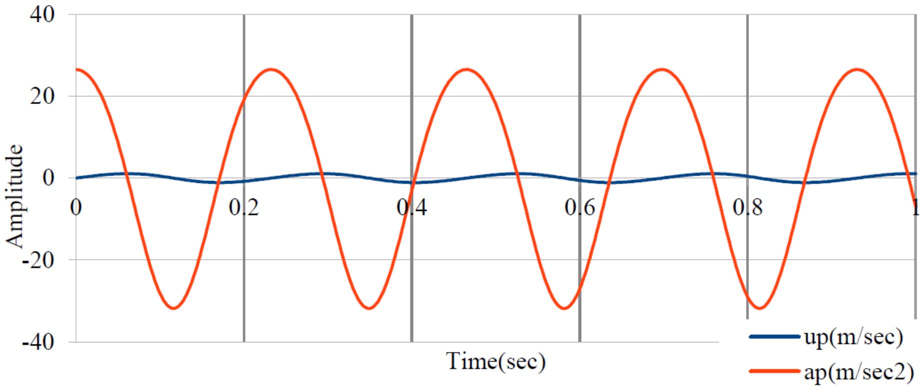

Figure 5.12: Acceleration and velocity during vibration

inverter set at 5 Hz.

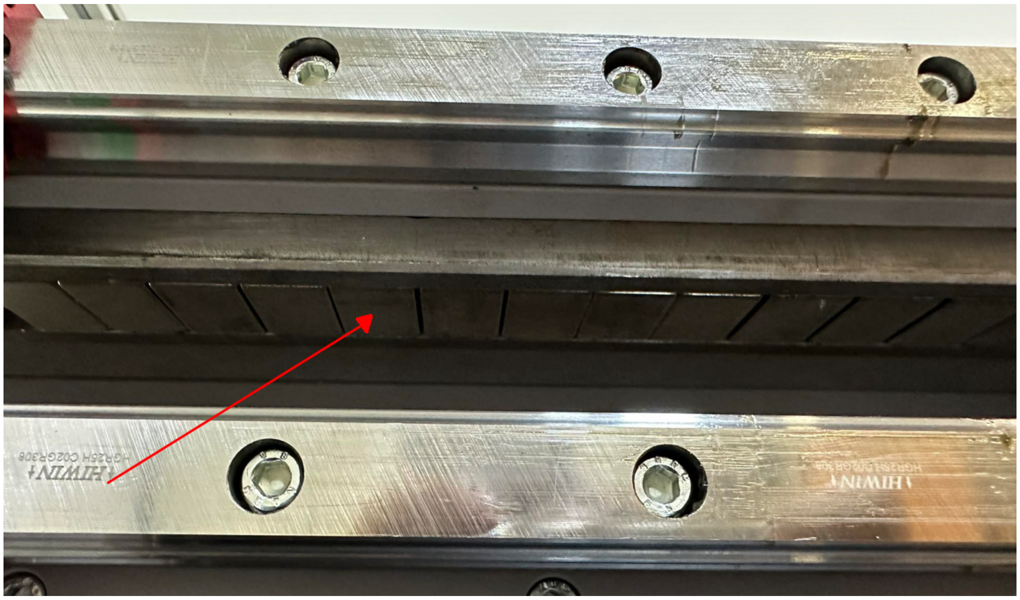

Figure 5.13: Series of magnets placed inside the C-shaped track.

The overall ageing strategy adopted for this mixed stress procedure is outlined below, Table 5.2. Similarly to the previous section, between every ageing the impedance spectroscopy of each was acquired:

Cycle number	**Stress Parameters**	**Duration**
C1	180-220 °C	6 hours
C2	180-220 °C	6 hours
C3	180-220 °C	6 hours
C4	180-220 °C	6 hours
C5	180-220 °C	6 hours
C6	180-220 °C	6 hours
C7	210–250 °C	3 hours
C8	210–250 °C	3 hours
C1	5 Hz	1 hours
C2	5 Hz	1 hours

Table 5.2: Thermal cycling and mechanical stress strategy

Below, the collective behaviour of impedance and phase spectroscopy graphs for poles 20A-31A are illustrated, Fig. 5.14-Fig. 5.16.

The effect of the high voltage test is apparent in the collective impedance spectroscopy of the poles. Compared to the healthy state, the graph is shifted to the left and the maximum impedance attained is lower as well. According to the parameter analysis carried out in Chapter 4, this is a sign for an increased C_{cc} and C_i and a lowered R_{cc}. The causes behind the parameter changes were touched upon in Section 5.1 and will not be reiterated.

Regarding the thermal cycling stress, the results are different compared with the fixed thermal stress. The ellipsis size reaches its maximum, the impedance rises, and the second antiresonance point shifts to the right of the healthy one, with a higher amplitude. These changes are primarily due to chemical alterations in the insulating system as a whole due to the thermal stress and accelerated delamination caused by the alternating size of the copper wire due to thermal enlargement. However, the shift in the secondary spike suggests that the main factor is the reduction of thin film capacitance, which leads to increased impedance.

Again contrary to the fixed thermal stress results, the behaviour of the impedance spectra and Nyquist plots does not follow a simple monotonic pattern during the accelerated ageing process. After each cycle, the amplitude either increases or decreases, with the Nyquist

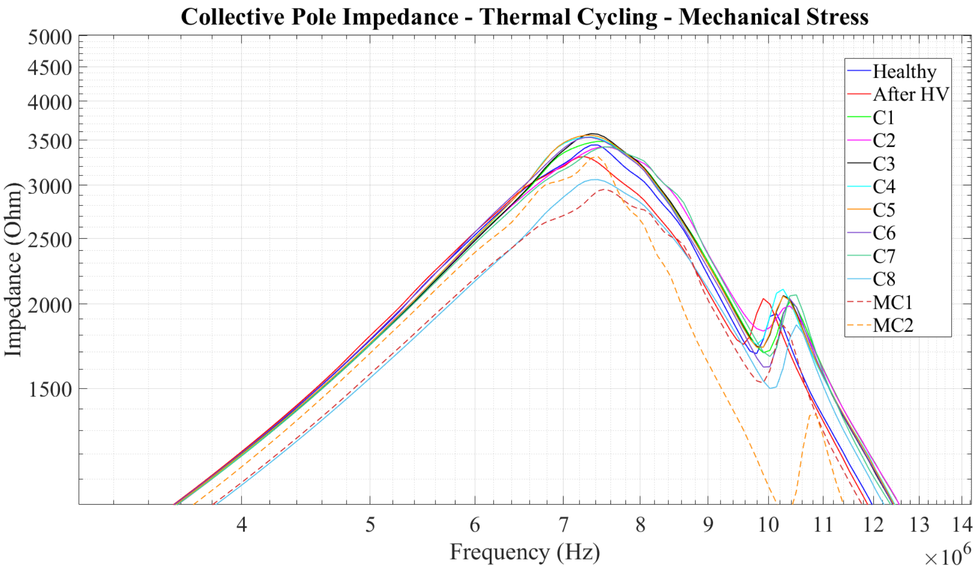

Figure 5.14: Collective impedance spectroscopy of 20A-31A poles for all thermal cycling and mechanical stress cycles.

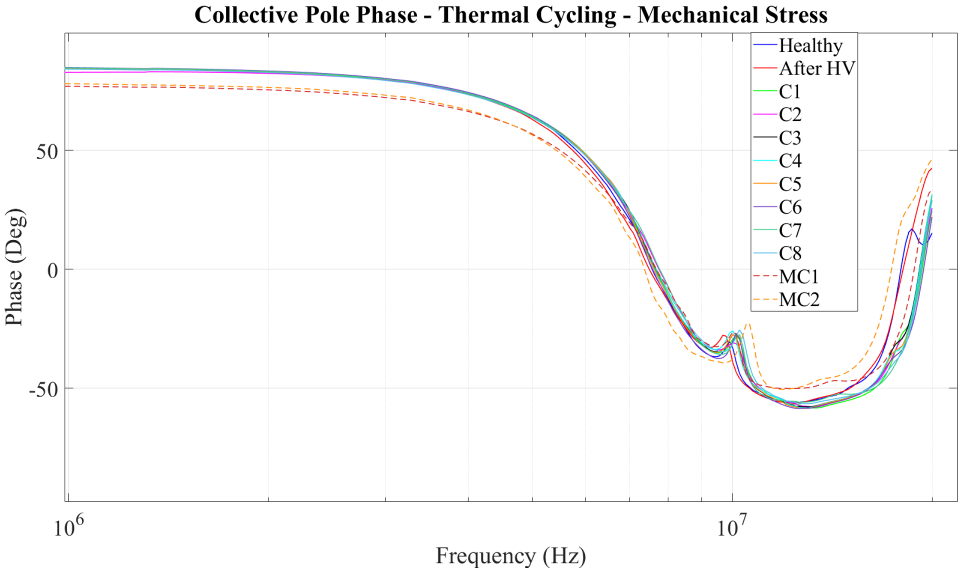

Figure 5.15: Collective phase spectroscopy of 20A-31A poles for all thermal cycling and mechanical stress cycles.

ellipsis gradually shrinking back to its original size. The most notable change is the shift of the secondary antiresonance point to the right, accompanied by a higher amplitude than that of the healthy poles. This complex behaviour is linked to changes in the chemical composition of the co-existing insulating materials (epoxy and thin film). As the insulation ages its resistance decreases, leading to a reduction of the maximum impedance attained during

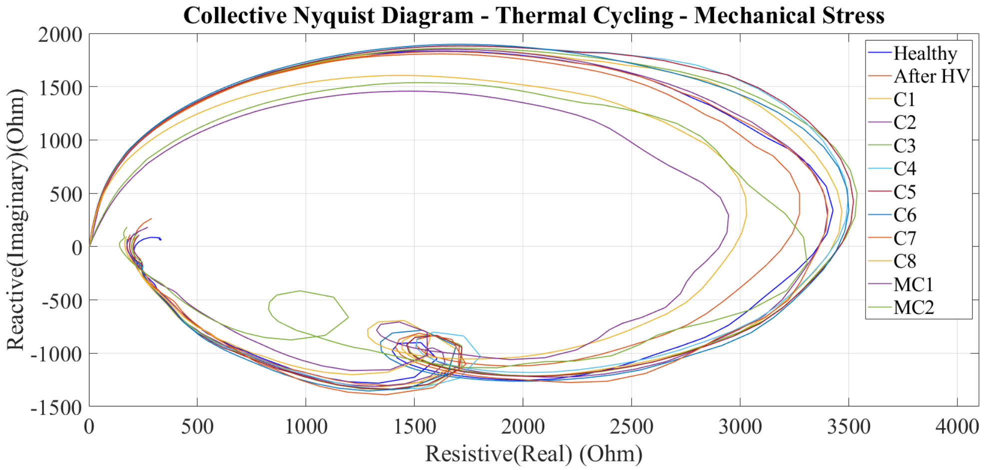

Figure 5.16: Collective Nyquist Diagram of 20A-31A poles for all thermal cycling and mechanical stress cycles.

the antiresonance. Simultaneously, as the ageing of the epoxy takes place the insulation capacitance reduces, which in turn increases capacitive reactance and overall impedance.

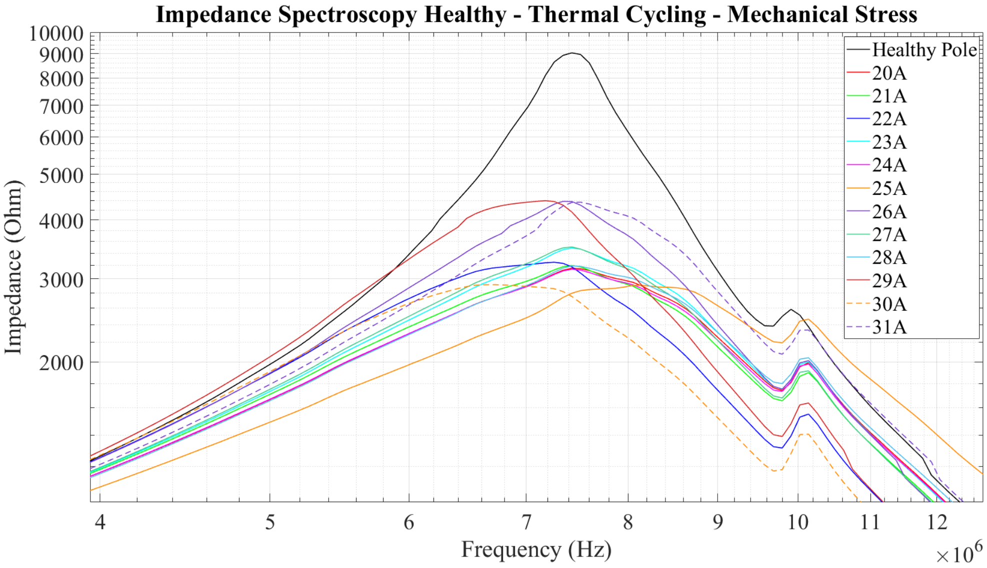

Figure 5.17: Healthy state impedance spectroscopy of 20A-31A poles.

During the mechanical stress cycles, we see a much more dramatic result. After the first cycle, the maximum impedance attained during the main antiresonance is lower and the location of the secondary antiresonance point is shifted to the left, when compared to the last thermal cycling stress cycle. This is an indication of an increase in C_i and a reduction of R_{cc}, which is connected to the turn insulation getting thinner and the coil-to-core insulation getting weaker. After the second cycle we can spot a change in the behaviour of the graph, the maximum impedance attained during the main antiresonance compared to the first mechanical stress cycle is higher, the location of the main antiresonance point is shifted to the left and the location of the secondary antiresonance point is shifted to the right. This combination of signs imply the increase of C_{cc} and R_i and the reduction of $R_c c$ and C_i. The concurrent increase of R_i and reduction of C_i indicate the delamination of the turn insulation from the copper wire, as the presence of air between the insulation and wire increases the distance between them. The increase of C_{cc} together with reduction of R_{cc} shows the coil-to-core insulation getting thinner, as the coil which is getting more and more loose from the epoxy starts to slam into the core due to the vibrations, eroding the coil to core insulation.

Now for us to explore the effect that manufacturing defects have on the insulation wear process due to thermal cycling and mechanical stress, we will now choose 3 poles of the group and analyse their behaviour, with the selection criteria being the same as for fixed thermal stress. After analysing the graphs in Fig. 5.17, the poles chosen were 22A due to low R_{cc} and high capacitance, 28A due to only low R_{cc} and pole 26A for high resemblance to the healthy pole prototype. Next, the behaviour of each pole's impedance spectroscopy during the fixed thermal stress process is showcased, Fig. 5.18-Fig. 5.20.

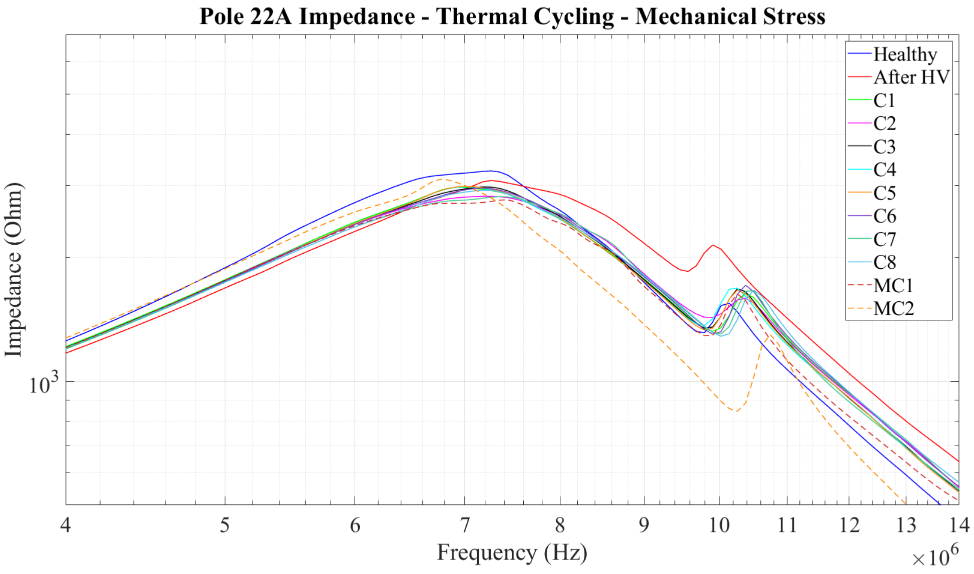

Figure 5.18: Impedance spectroscopy of poles 22A for all thermal cycling and mechanical cycles.

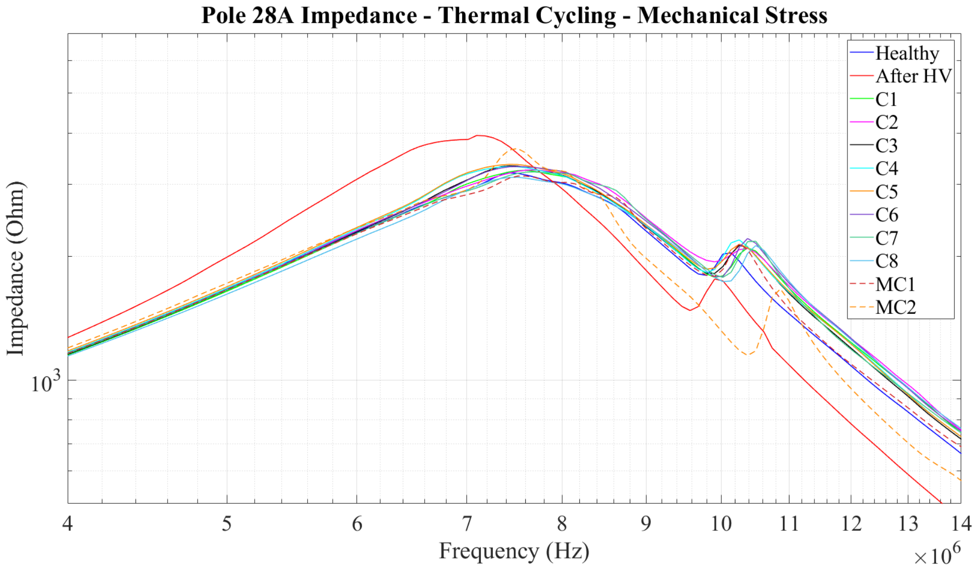

Figure 5.19: Impedance spectroscopy of poles 28A for all thermal cycling and mechanical cycles.

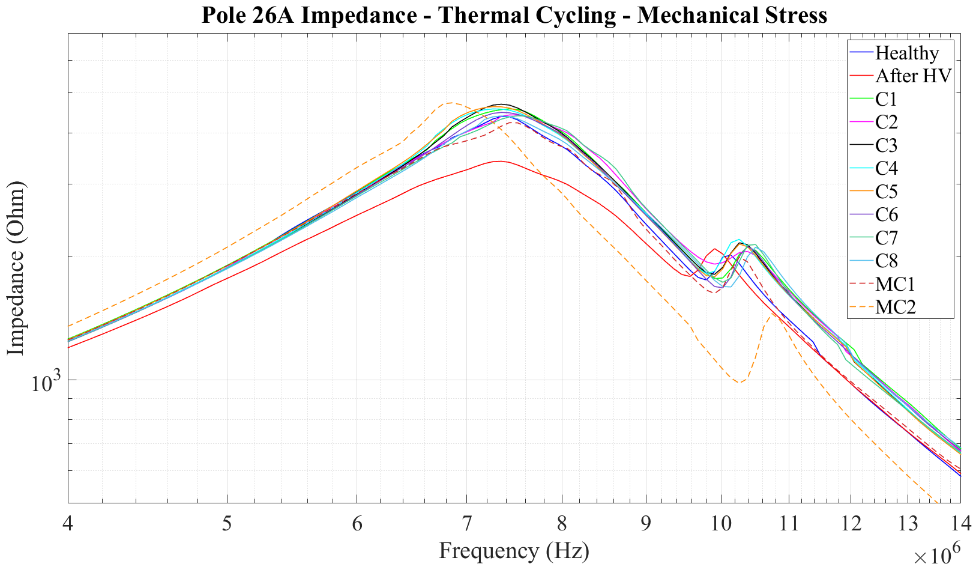

Figure 5.20: Impedance spectroscopy of poles 26A for all thermal cycling and mechanical cycles.

To better illustrate how each pole behaves, figures depicting the main antiresonance peak impedance location for all three poles, Fig 5.20-Fig. 5.23, as well as a figure for comparison reasons are provided, Fig. 5.24.

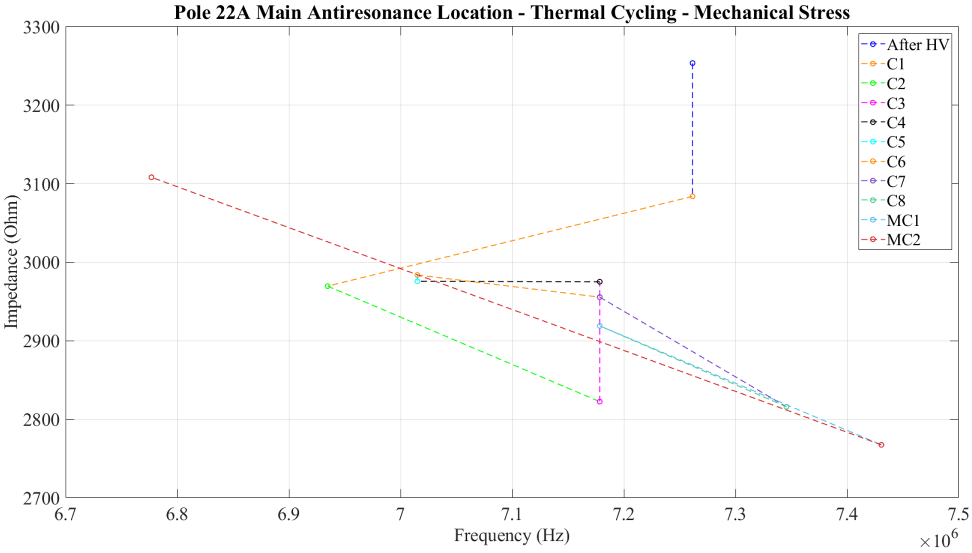

Figure 5.21: Impedance spectroscopy of poles 26A for all thermal cycling and mechanical cycles.

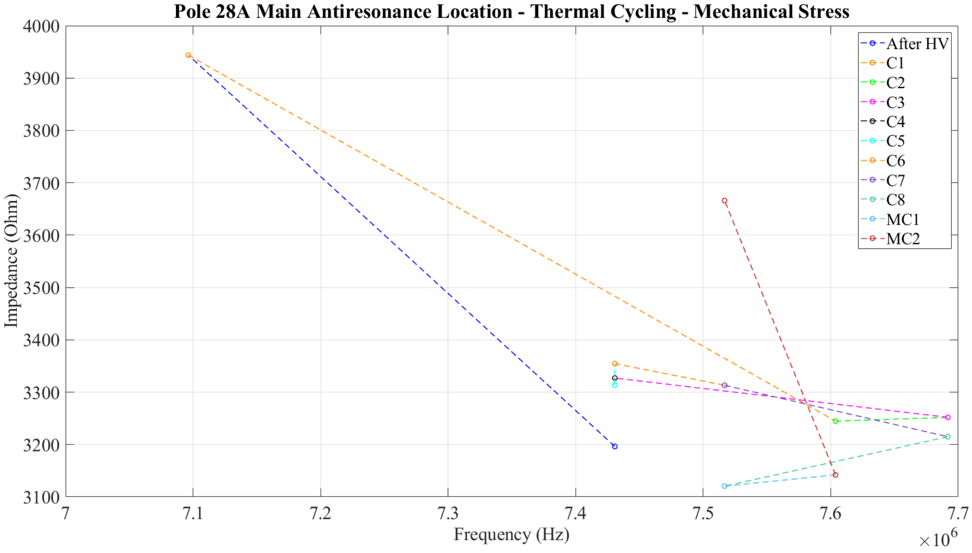

Figure 5.22: Impedance spectroscopy of poles 26A for all thermal cycling and mechanical cycles.

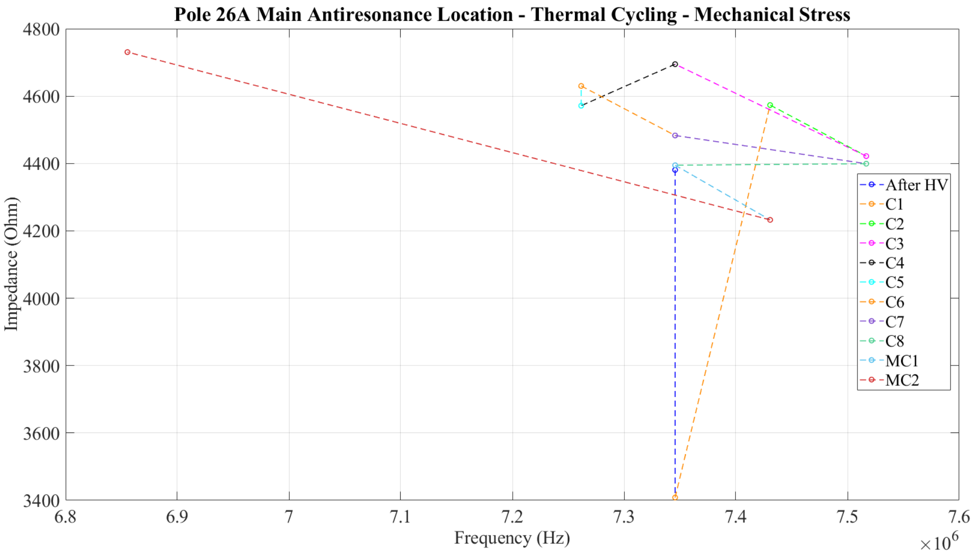

Figure 5.23: Impedance spectroscopy of poles 26A for all thermal cycling and mechanical cycles.

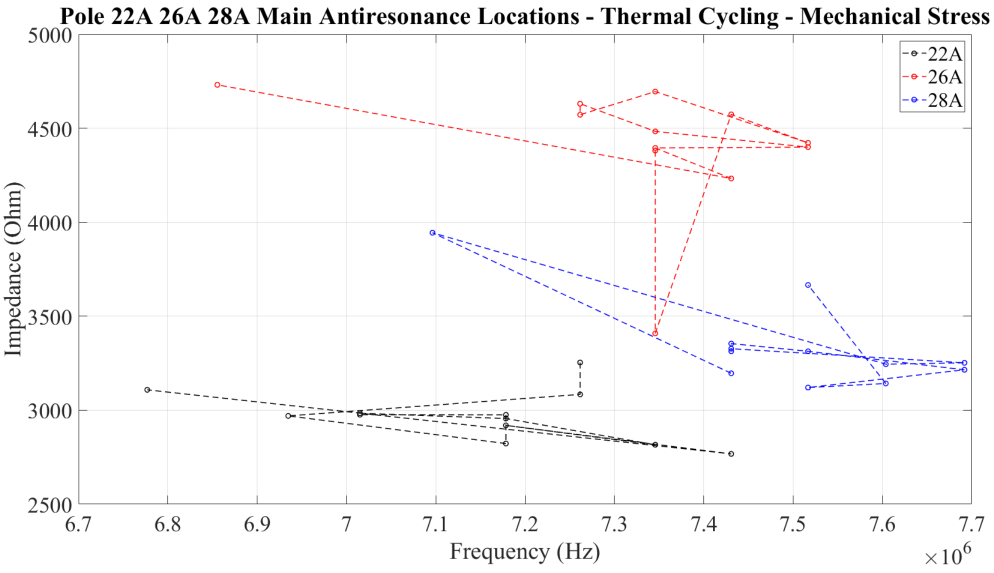

Figure 5.24: Comparison of main antiresonance peak impedance locations for 22A, 26A and 28A poles during all thermal and mechanical cycles.

Comparing the 3 graphs we can see that after the dramatic impact of the HV test, during the thermal cycling stress cycles, the main antiresonance peak impedance location remains close to the healthy state with some minor differences. In pole 26A, the impedance and frequency of the antiresonance point are slightly elevated after the first thermal cycle and stay there for the whole test stress. As mentioned previously, this signals changes in the chemical composition of the different insulation materials, resulting in an increase in its resistance value. In pole 22A, we can see the insulation capacitance value being the main parameter that fluctuates across the thermal cycles, with resistance immediately dropping, contrary to pole 26A, and being mostly monotonic in its reduction. This highlights the weakness of the insulation system as chemical change in the materials is no longer enough to support a high impedance value. Regarding pole 28A, which is the more moderate case between the two previous poles, its maximum impedance attained is stable across all thermal cycles except for the last cycle where it drops accompanied by an increase in capacitance.

As far as the mechanical stress cycles are concerned, the much more intense and predictable reaction of the graph is evident. After the first cycle, the antiresonance location is moved down and to the right across all poles, indicating a reduction in R_{cc} and C_{cc}. However, this is a transitional situation, as during the second cycle we see clear results. For poles 22A and 26A, we can see the antiresonance location shifts aggressively to the left and the impedance is increased. This again signals the delamination of the turn insulation from the copper wire and the vibration-caused erosion of the coil-to-core insulation, as we witness an increase of R_i and C_{cc} and the reduction of C_i. However, pole 28A behaves rather differently, as its graph's fluctuations are not as aggressive as in poles 22A and 26A. This could be an indication of the coil not placed perfectly in poles 22A and 26A, resulting in the uneven degradation of the coil-to-core insulation.

To conclude, the above remarks do not provide clear guidelines to verify the presence of manufacturing defects in the poles examined. The different behaviour of the pole impedance spectroscopy graphs during thermal cycle stress between are not enlightening enough to provide us with concrete evidence about the presence of manufacturing defects. Despite that not being the case about the mechanical stress, there are no signs in the healthy state graphs about potential manufacturing defects during the stress test.

6 Chapter 6: Conclusions and Outlook

During this project, it is shown that despite a physic-based model of a coil requiring thorough investigation for its development, it can be utilised to great effect for diagnostic and prognostic purposes.

More specifically:

- The step-by-step development of the equivalent circuit model was showcased. First, an initial basic design was proposed, the reasoning behind its parameter components was explained. Subsequently, a more advanced version of the model was introduced which was able to take into account the possibility of a coil-to-core short circuit fault with the addition of the coil-to-core insulation parameters. Ultimately, the final version of the model was presented, which contained circuit parameters tied to the equipment used during our tests. For each model version, a comparison between its impedance spectroscopy graph and the one produced for the healthy pole prototype was carried out.
- The effect that potential manufacturing defects have on the spectroscopy and Nyquist graphs was also investigated. To that end, we first compared the spectroscopy graphs and Nyquist diagram produced from the healthy state equivalent circuit model with the corresponding graphs where the value of a single parameter was either increased or decreased. Afterwards, we connected the changes in the diagrams with potential pole manufacturing defects for all model parameters. Finally, using information observed from the behaviour of the diagrams, a brief parameter analysis was constructed as well.
- An in-depth analysis on how to spot potential manufacturing defects through the impedance spectroscopy graph and the effect that those defects have on the ageing process of the insulation system under various stresses was carried out. After thoroughly examining the results, we can confirm the validity of using impedance spectroscopy for the quality assessment of segmented motor poles in tandem with other tests, like the surge test, that would complement its weak points.

For future work, regarding prognosis and quality assessment for motor poles, it would be worth focusing on the following points:

- An independent equivalent circuit model of the segmented motor pole without the need for calibration parameters due to the testing equipment. Moreover, developing a model in which the coil-to-core insulation is configured for each turn of the pole's coil will bring us closer to reality and may be the path to uncover other phenomena on the impedance spectroscopy graph.

- As far as the stresses that we had the poles undergo, we did not conduct degradation procedures with electrical stress as the main ageing mechanism, due to time constrains of the project. This is a factor that limits the range of the data we used for the insulation ageing analysis. So work based on electrical stress and an analysis on partial discharges would provide great insight regarding prognosis for motor poles. Moreover, the development of an experimental procedure during which two or more different types of stresses are applied simultaneously on a group of poles would enhance the quality of the data produced, as this brings us closer to the actual deterioration process of the pole insulation system.

References

[1] J. Pedersen, *Model Based and Robust Control Techniques for Internal Combustion Engine Throttle Valves.* PhD thesis, 12 2013.

[2] . H. D. Zhu, Z. Q., "Electrical machines and drives for electric, hybrid, and fuel cell vehicles.," *Proceedings of the IEEE*, vol. 95(4), 2007.

[3] `https://evkx.net/technology/motors/wrsm/`.

[4] `https://www.mathworks.com/help/mcb/ref/srmcommutation.html`.

[5] N. Bianchi, S. Bolognani, D. Bon, and M. Pre, "Rotor flux-barrier design for torque ripple reduction in synchronous reluctance motors," vol. 3, pp. 1193 – 1200, 11 2006.

[6] E. M. Illiano, *Design of a highly efficient brushless current excited synchronous motor for automotive purposes.* PhD thesis, ETH Zurich, 2014.

[7] `https://howtomechatronics.com/how-it-works/how-brushless-motor-and-esc-work/`.

[8] X. Wang, S. Xu, C. Li, and X. Li, "Field-weakening performance improvement of the yokeless and segmented armature axial flux motor for electric vehicles," *Energies*, vol. 10, no. 10, p. 1492, 2017.

[9] "http://hyperphysics.phy-astr.gsu.edu/hbase/Solids/hyst.html".

[10] Y. Ma, J. Cao, S. Jiang, and L. Li, "Failure analysis on nd-fe-b under the multi-physical field coupling of permanent-magnet synchronous machines," *Energy Reports*, vol. 9, pp. 2911–2920, 2023.

[11] M. Kumar, "Social, economic, and environmental impacts of renewable energy resources," Renewable Energy Hybrid Systems.(2020) Jan 21;1.

[12] N. J. Sheikh, D. F. Kocaoglu, and L. Lutzenhiser, "Social and political impacts of renewable energy: Literature review," *Technological Forecasting and Social Change*, vol. 108, pp. 102–110, 2016.

[13] F. Mwasilu, J. J. Justo, E.-K. Kim, T. D. Do, and J.-W. Jung, “Electric vehicles and smart grid interaction: A review on vehicle to grid and renewable energy sources integration,” *Renewable and Sustainable Energy Reviews*, vol. 34, pp. 501–516, 2014.

[14] J. Van Mierlo, M. Berecibar, M. El Baghdadi, C. De Cauwer, M. Messagie, T. Coosemans, V. A. Jacobs, and O. Hegazy, “Beyond the state of the art of electric vehicles: A fact-based paper of the current and prospective electric vehicle technologies,” *World Electric Vehicle Journal*, vol. 12, no. 1, 2021.

[15] Z. Tahir, G. Ahmadu, and M. Aminu, “Review of motors for electrical vehicles,” *J. Sci. Res. Rep*, vol. 24, pp. 1–6, 2019.

[16] S. Thangavel, D. Mohanraj, T. Girijaprasanna, S. Raju, C. Dhanamjayulu, and S. M. Muyeen, “A comprehensive review on electric vehicle: Battery management system, charging station, traction motors,” *IEEE Access*, vol. 11, no. 1, pp. 20994–21019, 2023.

[17] S. R. Jape and A. Thosar, “Comparison of electric motors for electric vehicle application,” *international Journal of Research in Engineering and Technology*, vol. 6, no. 09, pp. 12–17, 2017.

[18] P. Bhatt, H. Mehar, and M. Sahajwani, “Electrical motors for electric vehicle–a comparative study,” *Proceedings of recent advances in interdisciplinary trends in engineering & applications (RAITEA)*, 2019.

[19] L. Kumar and S. Jain, “Electric propulsion system for electric vehicular technology: A review,” *Renewable and Sustainable Energy Reviews*, vol. 29, pp. 924–940, 2014.

[20] V. Dmitrievskii, V. Prakht, E. Valeev, A. Paramonov, V. Kazakbaev, and A. Anuchin, “Comparative study of induction and wound rotor synchronous motors for the traction drive of a mining dump truck operating in wide constant power speed range,” *IEEE Access*, vol. 11, pp. 68395–68409, 2023.

[21] C. Rossi, D. Casadei, A. Pilati, and M. Marano, “Wound rotor salient pole synchronous machine drive for electric traction,” in *Conference Record of the 2006 IEEE Industry Applications Conference Forty-First IAS Annual Meeting*, vol. 3, pp. 1235–1241, 2006.

[22] "A closer look at brushed ac motors in evs." `https://chargedevs.com/features/a-closer-look-at-brushed-ac-motors-in-evs/`, 2022.

[23] N. Bianchi, S. Bolognani, E. Carraro, M. Castiello, and E. Fornasiero, "Electric vehicle traction based on synchronous reluctance motors," *IEEE Transactions on Industry Applications*, vol. 52, pp. 1–1, 11 2016.

[24] T. A. Huynh and M.-F. Hsieh, "Performance analysis of permanent magnet motors for electric vehicles (ev) traction considering driving cycles," *Energies*, vol. 11, no. 6, 2018.

[25] S. Niapour, G. Garjan, M. Shafiei, M. R. Feyzi, S. Danyali, and M. Bahrami Kouhshahi, "Review of permanent-magnet brushless dc motor basic drives based on analysis and simulation study," *International Review of Electrical Engineering*, vol. 9, no. 5, pp. 930–957, 2014.

[26] C. Chan, J. Jiang, W. Xia, and K. Chan, "Novel wide range speed control of permanent magnet brushless motor drives," *IEEE transactions on power electronics*, vol. 10, no. 5, pp. 539–546, 1995.

[27] Y.-H. Lim, Y.-S. Kook, and Y. Ko, "A new technique of reducing torque ripples for bdcm drives," *IEEE Transactions on Industrial Electronics*, vol. 44, no. 5, pp. 735–739, 1997.

[28] L. Shao, R. Navaratne, M. Popescu, and G. Liu, "Design and construction of axial-flux permanent magnet motors for electric propulsion applications—a review," *Ieee Access*, vol. 9, pp. 158998–159017, 2021.

[29] K. Akatsu and S. Wakui, "A comparison between axial and radial flux pm motor by optimum design method from the required output nt characteristics," *Compel-the International Journal for Computation and Mathematics in Electrical and Electronic Engineering - COMPEL-INT J COMPUT MATH ELEA*, vol. 25, pp. 496–509, 04 2006.

[30] J. F. Gieras, R.-J. Wang, and M. J. Kamper, *Axial flux permanent magnet brushless machines.* Springer Science & Business Media, 2008.

[31] T. J. Woolmer and M. McCulloch, "Analysis of the yokeless and segmented armature machine," in *2007 IEEE International Electric Machines & Drives Conference*, vol. 1, pp. 704–708, IEEE, 2007.

[32] B. Zhang, T. Seidler, R. Dierken, and M. Doppelbauer, "Development of a yokeless and segmented armature axial flux machine," *IEEE Transactions on Industrial Electronics*, vol. 63, no. 4, pp. 2062–2071, 2015.

[33] W. Liu, L. Liu, I.-Y. Chung, D. Cartes, and W. Zhang, "Modeling and detecting the stator winding fault of permanent magnet synchronous motors," *Simulation Modelling Practice and Theory*, vol. 27, pp. 1–16, 09 2012.

[34] G. Stone, "Condition monitoring and diagnostics of motor and stator windings–a review," *IEEE Transactions on Dielectrics and Electrical Insulation*, vol. 20, no. 6, pp. 2073–2080, 2013.

[35] B. Ebrahimi and J. Faiz, "Magnetic field and vibration monitoring in permanent magnet synchronous motors under eccentricity fault," *Electric Power Applications, IET*, vol. 6, pp. 35–45, 01 2012.

[36] A. Singh, B. Grant, R. DeFour, C. Sharma, and S. Bahadoorsingh, "A review of induction motor fault modeling," *Electric Power Systems Research*, vol. 133, pp. 191–197, 2016.

[37] Y. Chen, S. Liang, W. Li, H. Liang, and C. Wang, "Faults and diagnosis methods of permanent magnet synchronous motors: A review," *Applied Sciences*, vol. 9, no. 10, p. 2116, 2019.

[38] M. Zhu, W. Hu, and N. C. Kar, "Torque-ripple-based interior permanent-magnet synchronous machine rotor demagnetization fault detection and current regulation," *IEEE Transactions on Industry Applications*, vol. 53, no. 3, pp. 2795–2804, 2016.

[39] J. Faiz and H. Nejadi-Koti, "Demagnetization fault indexes in permanent magnet synchronous motors—an overview," *IEEE Transactions on Magnetics*, vol. 52, no. 4, pp. 1–11, 2015.

[40] J. D. McFarland and T. M. Jahns, "Investigation of the rotor demagnetization characteristics of interior pm synchronous machines during fault conditions," *IEEE Transactions on Industry Applications*, vol. 50, no. 4, pp. 2768–2775, 2013.

[41] K. N. Gyftakis, S. A. Rasid, G. A. Skarmoutsos, and M. Mueller, "The demagnetization harmonics generation mechanism in permanent magnet machines with concentrated

windings," *IEEE Transactions on Energy Conversion*, vol. 36, no. 4, pp. 2934–2944, 2021.

[42] S. Sharouni, P. Naderi, M. Hedayati, and P. Hajihosseini, "Demagnetization fault detection by a novel and flexible modeling method for outer rotor permanent magnet synchronous machine," *International Journal of Electrical Power & Energy Systems*, vol. 116, p. 105539, 2020.

[43] P. Liang, F. Chai, Y. Yu, and L. Chen, "Analytical model of a spoke-type permanent magnet synchronous in-wheel motor with trapezoid magnet accounting for tooth saturation," *IEEE Transactions on Industrial Electronics*, vol. 66, no. 2, pp. 1162–1171, 2019.

[44] M. Galea, L. Papini, H. Zhang, C. Gerada, and T. Hamiti, "Demagnetization analysis for halbach array configurations in electrical machines," *IEEE Transactions on Magnetics*, vol. 51, no. 9, pp. 1–9, 2015.

[45] J. Farooq, S. Srairi, A. Djerdir, and A. Miraoui, "Use of permeance network method in the demagnetization phenomenon modeling in a permanent magnet motor," *IEEE transactions on magnetics*, vol. 42, no. 4, pp. 1295–1298, 2006.

[46] M. Zafarani, T. Goktas, and B. Akin, "A simplified mathematical approach to model and analyze magnet defects fault signatures in permanent magnet synchronous motors," pp. 1–6, 2015.

[47] Z. Li, X. Huang, Y. Yu, D. Jiang, L. Wu, and T. Shi, "Nonlinear analytical modelling for surface-mounted permanent magnet motors with magnet defect fault," *IEEE Transactions on Energy Conversion*, vol. 37, no. 3, pp. 1955–1964, 2022.

[48] Z. Ullah, B. A. Lodhi, and J. Hur, "Detection and identification of demagnetization and bearing faults in pmsm using transfer learning-based vgg," *Energies*, vol. 13, no. 15, 2020.

[49] P. McFadden and J. Smith, "Model for the vibration produced by a single point defect in a rolling element bearing," *Journal of sound and vibration*, vol. 96, no. 1, pp. 69–82, 1984.

[50] P. McFadden and J. Smith, “The vibration produced by multiple point defects in a rolling element bearing,” *Journal of sound and vibration*, vol. 98, no. 2, pp. 263–273, 1985.

[51] Y.-T. Su and S.-J. Lin, “On initial fault detection of a tapered roller bearing: frequency domain analysis,” *Journal of Sound and Vibration*, vol. 155, no. 1, pp. 75–84, 1992.

[52] V. Patel, N. Tandon, and R. Pandey, “Vibrations generated by rolling element bearings having multiple local defects on races,” *Procedia Technology*, vol. 14, pp. 312–319, 2014.

[53] S. Mufazzal, S. Muzakkir, and S. Khanam, “Theoretical and experimental analyses of vibration impulses and their influence on accurate diagnosis of ball bearing with localized outer race defect,” *Journal of Sound and Vibration*, vol. 513, p. 116407, 2021.

[54] J. Lee, Y. Lee, and N. Kim, “Detection and analysis of shaft misalignment in application of production and logistics systems using motor current signature analysis,” *Expert Systems with Applications*, vol. 217, p. 119463, 2023.

[55] H. M. Kelk, A. Eghbali, and H. A. Toliyat, “Modeling and analysis of cage induction motors under rotor misalignment and air gap eccentricity,” vol. 2, pp. 1324–1328, 2005.

[56] J. G. Cintron-Rivera, S. N. Foster, and E. G. Strangas, “Mitigation of turn-to-turn faults in fault tolerant permanent magnet synchronous motors,” *IEEE Transactions on Energy Conversion*, vol. 30, no. 2, pp. 465–475, 2014.

[57] K. N. Gyftakis and A. J. Marques-Cardoso, “Reliable detection of very low severity level stator inter-turn faults in induction motors,” in *IECON 2019-45th Annual Conference of the IEEE Industrial Electronics Society*, vol. 1, pp. 1290–1295, IEEE, 2019.

[58] C. A. Platero, K. N. Gyftakis, P. A. Panagiotou, and A. Fernandez, “Scheme for synchronous machine stator turn-to-turn protection,” *IET Electric Power Applications*, vol. 14, no. 4, pp. 716–722, 2020.

[59] F. Wu, P. Zheng, and T. M. Jahns, “Analytical modeling of interturn short circuit for multiphase fault-tolerant pm machines with fractional slot concentrated windings,” *IEEE Transactions on Industry Applications*, vol. 53, no. 3, pp. 1994–2006, 2017.

[60] B.-G. Gu, J.-H. Choi, and I.-S. Jung, “Development and analysis of interturn short fault model of pmsms with series and parallel winding connections,” *IEEE Transactions on Power Electronics*, vol. 29, no. 4, pp. 2016–2026, 2013.

[61] D. S. B. Fonseca, C. M. C. Santos, and A. J. M. Cardoso, “Stator faults modeling and diagnostics of line-start permanent magnet synchronous motors,” *IEEE Transactions on Industry Applications*, vol. 56, no. 3, pp. 2590–2599, 2020.

[62] A. C. Babu and J. Seshadrinath, “Stator inter-turn fault modelling and analysis on induction motor based on mccm,” pp. 1–6, 2021.

[63] I. Jeong, B. J. Hyon, and K. Nam, “Dynamic modeling and control for spmsms with internal turn short fault,” *IEEE Transactions on Power Electronics*, vol. 28, no. 7, pp. 3495–3508, 2012.

[64] Z. Zhao, Y. Chen, Y. Yu, M. Han, C. Tang, and C. Yao, “Equivalent broadband electrical circuit of synchronous machine winding for frequency response analysis based on gray box model,” *IEEE Transactions on Energy Conversion*, vol. 36, no. 4, pp. 3512–3521, 2021.

[65] H. Elmadah, D. Roger, and N. Takorabet, “Hf model of high temperature machine coils,” pp. 1–2, 2019.

[66] X. Cao, H. Yang, and X. Bai, “Equivalent capacitance model of segmented induction coil in electromagnetic exploration system for deep resources,” *IEEE Sensors Journal*, vol. 21, no. 6, pp. 7756–7767, 2021.

[67] H. Zhang, S. Wang, D. Yuan, and X. Tao, “Double-ladder circuit model of transformer winding for frequency response analysis considering frequency-dependent losses,” *IEEE Transactions on Magnetics*, vol. 51, no. 11, pp. 1–4, 2015.

[68] K. Nakahara and F. Kuroki, “Equivalent circuit model of multi-layered coils for integrated sensor applications in medium-wave frequencies,” pp. 1–3, 2016.

[69] W. Xue, Z. Huang, X. Xu, B. Shen, and Z. Jin, “Ramping loss analysis of no-insulation hts coil under external field using an improved equivalent circuit model,” *IEEE Transactions on Applied Superconductivity*, vol. 31, no. 8, pp. 1–5, 2021.

[70] A. Massarini and M. K. Kazimierczuk, “Self-capacitance of inductors,” *IEEE transactions on power electronics*, vol. 12, no. 4, pp. 671–676, 1997.

[71] G. Lv, D. Zeng, and T. Zhou, “Analysis of secondary losses and efficiency in linear induction motors with composite secondary based on space harmonic method,” *IEEE Transactions on Energy Conversion*, vol. 32, no. 4, pp. 1583–1591, 2017.

[72] “Ieee recommended practice for testing insulation resistance of electric machinery,” *IEEE Std 43-2013 (Revision of IEEE Std 43-2000)*, pp. 1–37, 2014.

[73] X. Chen, Z. Zhang, S. Yu, and T.-G. Zsurzsan, “Fringing effect analysis of parallel plate capacitors for capacitive power transfer application,” *2019 IEEE 4th International Future Energy Electronics Conference (IFEEC)*, pp. 1–5, 2019.

[74] P. Chen, J. Liu, H. Zhang, and B. Chu, “Increase of capacitance of thick dielectrics by fringe effect,” *IEEE Transactions on Dielectrics and Electrical Insulation*, vol. 26, no. 5, pp. 1716–1719, 2019.

[75] Y. Feng, B. Shao, X. Tang, Y. Han, T. Wu, and Y. Suzuki, “Improved capacitance model involving fringing effects for electret-based rotational energy harvesting devices,” *IEEE Transactions on Electron Devices*, vol. 65, no. 4, pp. 1597–1603, 2018.

[76] P. W. Atkins, J. De Paula, and J. Keeler, “Atkins’ physical chemistry,” 2023.

A Appendix A

A.1 Equipment used during tests

Figure A.1: Megger FRAX 99 Sweep Frequency Response Analyzer.

Figure A.2: Megger MIT1525 15kV Insulation Tester.

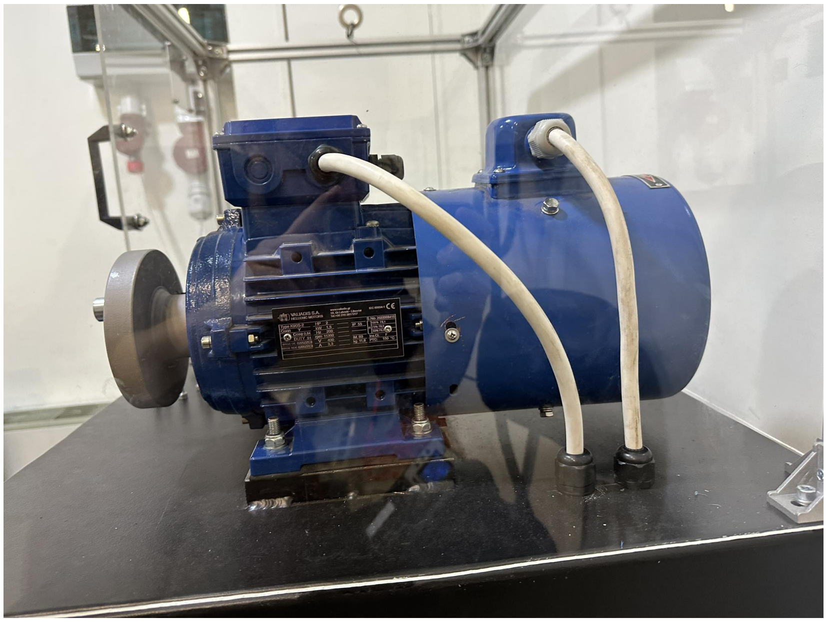

Figure A.3: Picture of the induction motor used in the mechanical stress test.

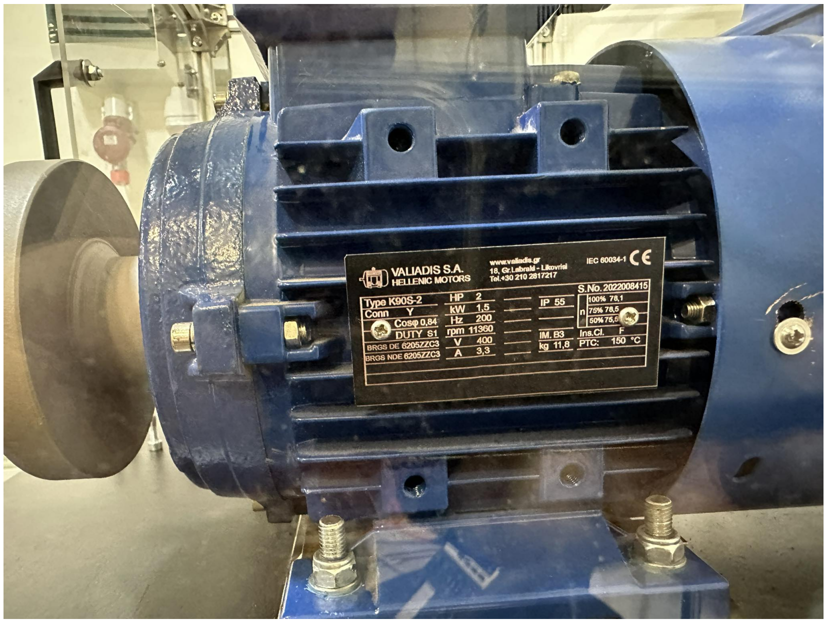

Figure A.4: Rated values of the induction motor.

Figure A.5: Picture of the inverter used to power the induction motor.

Figure A.6: Rated values of the inverter.

B Appendix B

B.1 General figures

Figure B.1: Insulation resistanc emeasurement for copper bar pair 1-2.

Figure B.2: Insulation resistanc emeasurement for copper bar pair 3-4.

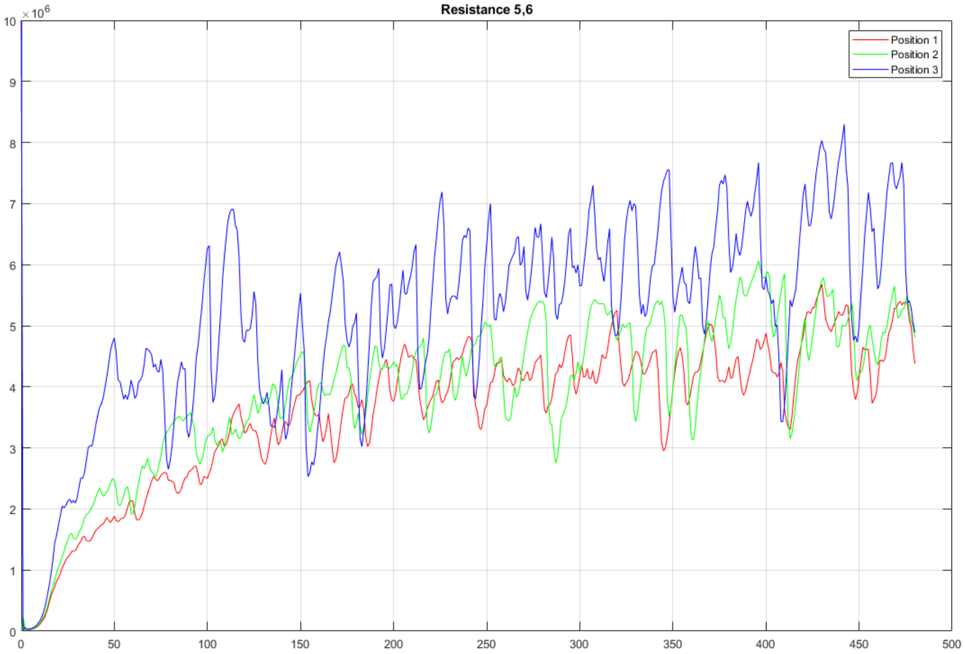

Figure B.3: Insulation resistanc emeasurement for copper bar pair 5-6.

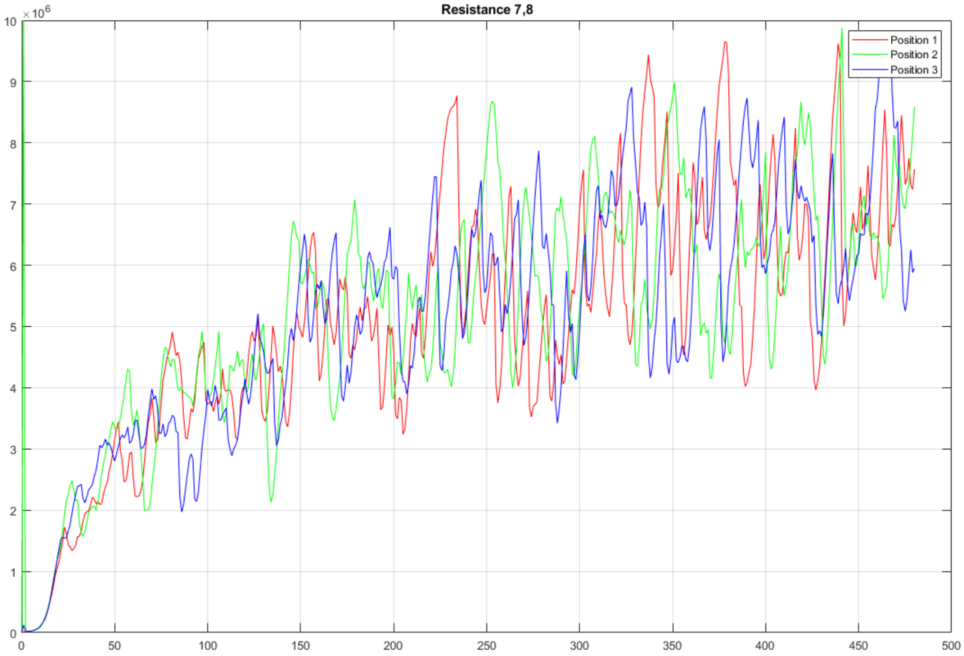

Figure B.4: Insulation resistanc emeasurement for copper bar pair 7-8.

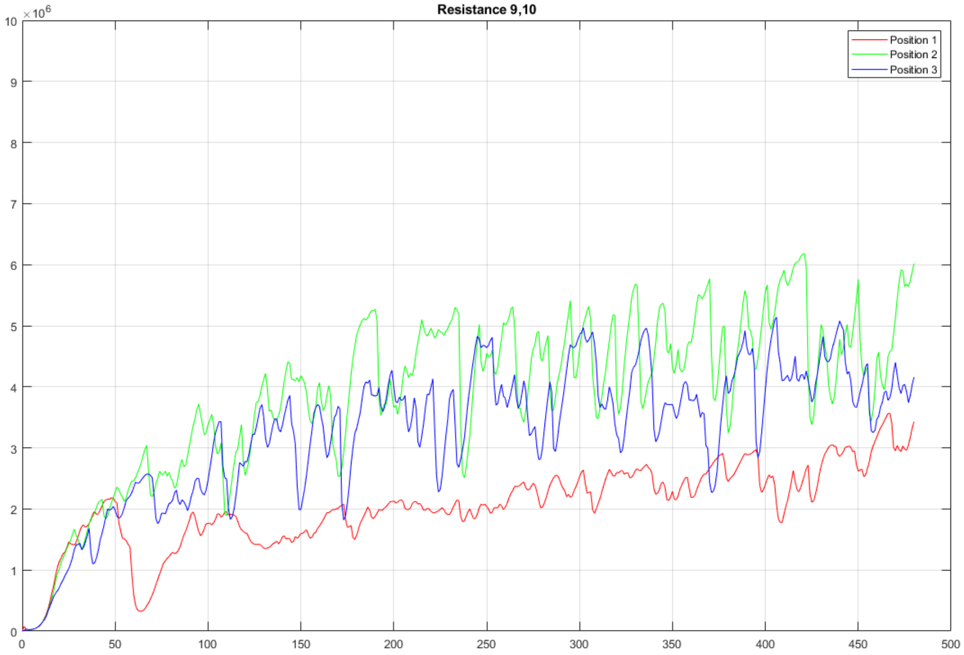

Figure B.5: Insulation resistanc emeasurement for copper bar pair 9-10.